3-2022

Magnetic Anomaly Absolute Positioning for Hypersonic Aircraft

Alexander J. McNeil

MAGNETIC ANOMALY ABSOLUTE POSITIONING FOR HYPERSONIC AIRCRAFT

THESIS

Alexander J. McNeil

AFIT-ENG-MS-22-M-046

DEPARTMENT OF THE AIR FORCE
AIR UNIVERSITY

AIR FORCE INSTITUTE OF TECHNOLOGY

Wright-Patterson Air Force Base, Ohio

AFIT-ENG-MS-22-M-046

MAGNETIC ANOMALY ABSOLUTE POSITIONING FOR HYPERSONIC AIRCRAFT

THESIS

Presented to the Faculty

Department of Electrical and Computer Engineering

Graduate School of Engineering and Management

Air Force Institute of Technology

Air University

Air Education and Training Command

in Partial Fulfillment of the Requirements for the

Degree of Master of Science in Electrical Engineering

Alexander J. McNeil, B.S.E.E.

March 17, 2022

AFIT-ENG-MS-22-M-046

MAGNETIC ANOMALY ABSOLUTE POSITIONING FOR HYPERSONIC AIRCRAFT

THESIS

Alexander J. McNeil, B.S.E.E.

Committee Membership:

Joseph A. Curro, Ph.D
Chair

Robert C. Leishman, Ph.D
Member

Aaron J. Canciani, Ph.D
Member

David A. Woodburn, Ph.D
Member

Abstract

The Global Positioning System (GPS) has proven to be an extremely valuable asset for navigation, and timing. GPS has become the standard navigation system for all applications, but GPS has limitations. GPS is susceptible to jamming, spoofing, and in the case of hypersonic aircraft, is likely unavailable. When an aircraft is traveling at hypersonic speeds, there is a plasma sheath that surrounds the aircraft. This plasma sheath blocks electromagnetic waves [1], and is therefore responsible for a GPS blackout. GPS unavailability for hypersonic aircraft has prompted the research into the viability of alternate navigation systems for these aircraft. This paper seeks to explore the viability of Magnetic Navigation (MagNav) [2] for hypersonic aircraft. Hypersonic aircraft present new challenges for MagNav including: high altitudes, high speeds, large scale map availability, and new noise sources. This paper explores these challenges to determine if any poses an insurmountable problem. Simulations are conducted to explore the potential performance of MagNav on a hypersonic vehicle. These simulations conclude that MagNav is viable on a hypersonic aircraft.

Table of Contents

Page

List of Figures

Figure Page

List of Tables

MAGNETIC ANOMALY ABSOLUTE POSITIONING FOR HYPERSONIC AIRCRAFT

I. Introduction

1.1 Problem Motivation

The Global Positioning System (GPS) has proven to be the navigation, and timing standard for all applications since its introduction. With world-wide availability and near meter level accuracy, it has proven to be extremely useful. In modern times, the flaws in the GPS system have started to show. GPS is prone to jamming and spoofing. These vulnerabilities are a byproduct of the GPS system design, and have prompted research in the field of alternative navigation systems.

One such alternative navigation method is Magnetic Navigation (MagNav). MagNav uses magnetic anomalies in the earth's crust to provide absolution position [2], using a scalar map matching approach. In 2016, Canciani created the MagNav navigation system. This system uses a combination of altimeters, inertial measurement unit (IMU)s, magnetometers, and magnetic anomaly maps to provide absolute positioning. Since then, there have been several advancements such as online calibration [3] and vector-based MagNav [12]. Magnetic anomalies are present over the entire globe and provide a virtually unjammable and unspoofable navigation source. However, MagNav requires maps of these magnetic anomalies. These maps are somewhat common, albeit spotty and there are some world-wide maps that are collected via satellite surveys. New magnetic anomaly maps are constantly being created, making this alternative navigation source increasingly viable with the passage of time.

MagNav provides a compelling alternative navigation option for hypersonic vehicles. Hypersonic navigation will be entirely dependent on an alternate navigation approaches. Due to the communication blackout problem. Communications blackout is caused by a plasma sheath around the hypersonic aircraft, blocking the electromagnetic waves used for communication [1]. This plasma is created from friction between the aircraft and the air as a result of traveling at the speeds necessary to be considered hypersonic. This thesis will have to provide base level analysis of these potential plasma effects. However, additional research showing the potential effects of this plasma for MagNav will be required of future research.

Hypersonic trajectory planning is not trivial as highlighted by Lysak [8]. Lysak provided a machine learning-based system that was capable of planning a hypersonic trajectory in a six degree of freedom simulation. Since these trajectories are readily available, they can be easily repurposed as truth data for navigation simulations. Lysak's work provides an excellent source of data as it is both on the forefront of hypersonic trajectory planning and is readily available, at AFIT.

This thesis seeks to use the navigation system created by Canciani [2], with the trajectories created by Lysak [8]. This adaptation of MagNav will challenge core assumptions of speed and altitude that MagNav has assumed. In addition, new problems, especially those related to map size, are expected. Maps are typically confined to smaller areas, however due to the vast distances covered by a hypersonic aircraft in a short time, the map size requirement for MagNav will be significantly increased. This will mean that systems designed for map handling will have to be adjusted to allow for simulation to be feasible for hypersonic aircraft.

1.2 Research Objectives

The objectives for this thesis is to simulate MagNav on a hypersonic aircraft. The following objectives and questions are in place to accomplish this, and to provide thorough simulation:

- Does the plasma sheath create a significant barrier to prohibit the function of MagNav on a hypersonic vehicle?
- Provide an analysis on maps to create more computationally friendly map handling algorithms. Current map handling algorithms are too complex to be viable with the map sizes for hypersonic MagNav.
- Create and analyze MagNav simulations using a high quality magnetic anomaly map on hypersonic trajectories.
- Provide an analysis on the current worldwide viability of MagNav on a hypersonic trajectory, by analyzing the performance of MagNav on a satellite based magnetic anomaly map.
- Conduct analysis and simulation of vector based MagNav for hypersonic trajectories. Since vector MagNav shows a potential increase in performance, and the Enhanced Magnetic Model (EMM) has a world-wide vector map.
- Investigate which, if any, core assumptions of MagNav are invalidated as a result of hypersonic speeds or altitudes.

1.3 Document Overview

This thesis consists of four additional chapters. Chapter II provides an overview of relevant literature to both provided a foundation for the research, and to provide

the reader with an understanding of both the fields of MagNav and hypersonics. Chapter III covers the tools, analysis algorithms, simulation designs, setups, and initial conditions used. Chapter IV provides the results from simulations and their analysis. Finally, Chapter V summarizes the results, provides insights to the analysis, and suggests areas of potential future research.

II. Background and Literature Review

This chapter starts by covering the basics of Magnetic Navigation (MagNav). After this, a detailed analysis of magnetic anomaly maps, and the potential issues that arise with current maps as result of hypersonic speeds is performed. Following this analysis, scrutiny of magnetic noise sources, and calibration methods used to remove these noise sources is presented. After establishing the foundation for MagNav, the relevant aspects of hypersonic flight characteristics are highlighted. These flight characteristics have the side effect of creating plasma around the hypersonic aircraft. This plasma might create magnetic noise. However, since this is a mostly unexplored field, a basic analysis of the potential plasma effects is presented in the final section of this chapter.

2.1 Magnetic Navigation

MagNav is a navigation technique that uses a combination of inertial measurement units, altimeters, and magnetometers to obtain absolute positioning using magnetic anomalies referenced via magnetic anomaly maps. Aerial MagNav was successfully demonstrated in 2016 by Canciani [2]. This section will cover the crucial elements of the earth's magnetic anomaly field, the basics of navigation filtering, and the navigation filter proposed by Canciani [2].

2.1.1 Magnetic Anomaly Fields

Magnetic Anomaly Fields are natural phenomenons that occur from magnetization in the rocks in the earth's crust [13]. The magnetic anomaly field is different from the earths magnetic core field. The earths magnetic core field is the result of the movement of the magma currents in the earth's core [13]. The core field is modeled using the

World Magnetic Model (WMM) [4]. For the purposes of this paper, all deviating magnetic fields from the WMM that are not from the noise sources in Section 2.3 are magnetic anomaly fields. These magnetic fields are constant phenomenons that change on geological timescales; meaning that for hundreds of years there is little drift in the anomaly field. This stability results in the ability to map magnetic anomaly fields. These maps remain valid for thousands of years, assuming no major geological disturbances. The mapping process and its limitations are outlined in Section 2.2. An example of a magnetic anomaly map can be seen in Figure 1. MagNav is a favorable alternate navigation source as these anomaly maps are widely available, with some caveats. Some of these maps are capable of modeling the whole globe. On a flight across the United States, Canciani achieved 3.2 km Distance Root Mean Squared (DRMS) performance using a magnetic anomaly based navigation system [2]. The basis of this navigation filter is covered in the next sections.

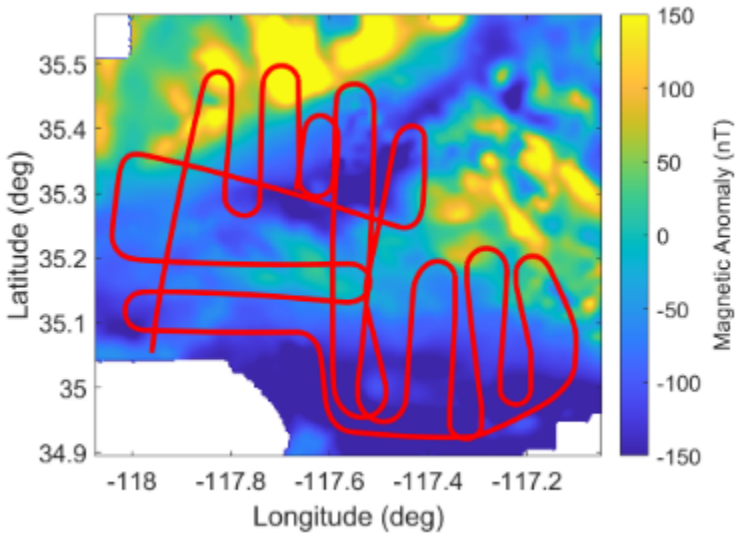

Figure 1: Magnetic anomaly map with flight path in red [3]

2.1.2 The Extended Kalman Filter

The Extended Kalman Filter (EKF) is non-linear Kalman Filter. This filtering system is used to estimate both a state vector ($\underline{\hat{x}}_k$) and covariance matrix ($\boldsymbol{P}_k$). In the case of MagNav, the states are aircraft position. The prediction equations can be seen below[14].

$$\underline{\hat{x}}_{k|k-1} = f(\underline{\hat{x}}_{k-1|k-1}) + \underline{u}_k \tag{1}$$

$$\boldsymbol{P}_{k|k-1} = \boldsymbol{F}_k \boldsymbol{P}_{k-1|k-1} \boldsymbol{F}_k^T + \boldsymbol{Q}_k \tag{2}$$

$$\tag{3}$$

During the prediction steps shown in (1) and (2). f is a non-linear function which describes the motion of the states as a function of the previous time step's states ($\underline{\hat{x}}_{k-1|k-1}$) and additive white noise u_k. The partial derivative of (1) with respect to the individual states is the $\boldsymbol{F}_k$ matrix in (2), which predicts the covariance $\boldsymbol{P}_{k|k-1}$ with some noise $\boldsymbol{Q}_k$. After the predictions, the updates are performed. The first step of the update process is seen below [14].

$$\underline{\bar{y}}_k = \underline{z}_k - h(\underline{\hat{x}}_{k|k-1}) \tag{4}$$

$$\boldsymbol{S}_k = \boldsymbol{H}_k \boldsymbol{P}_{k|k-1} \boldsymbol{H}_k^T + \boldsymbol{R}_k \tag{5}$$

$$\boldsymbol{K}_k = \boldsymbol{P}_{k|k-1} \boldsymbol{H}_k^T \boldsymbol{S}_k^{-1} \tag{6}$$

$$\tag{7}$$

The updating step follows a similar methodology to the prediction step. First a predicted measurement is calculated with the non-linear function h, and its Jacobian with respect to the state $\underline{x}_k$, $\boldsymbol{H}$ is calculated. Since the Jacobians of f and h are not

always analytical, the matrices $\boldsymbol{F}$ and $\boldsymbol{H}$ can be calculated through finite differencing, as is the case in MagNav. The Jacobian $\boldsymbol{H}$ is used with noise $\boldsymbol{R}$ and the estimated covariance to create the innovation covariance $\boldsymbol{S}$. The innovation covariance is used to create the Kalman gain $\boldsymbol{K}$. The final step of the process is to update the state estimate to get $\underline{\hat{x}}_{k|k}$ and state covariance $\boldsymbol{P}_{k|k}$.

$$\underline{\hat{x}}_{k|k} = \underline{\hat{x}}_{k|k-1} + \boldsymbol{K}_k \underline{\bar{y}_k} \tag{8}$$

$$\boldsymbol{P}_{k|k} = (\boldsymbol{I} - \boldsymbol{K}_k \boldsymbol{H}_k)\boldsymbol{P}_{k|k-1} \tag{9}$$

The Kalman Gain is used to weigh measurements before the state vector and covariance matrix is updated. Once the Kalman Gain has been calculated, the state vector and covariance matrix are updated with the weighted measurements.

The original design for the MagNav filter is based on the Rao-Blackwellized particle filter. This filter is a combination of a particle filter and an EKF [15]. The main advantage of this filter is to allow for large initial position uncertainties and non-Gaussian noise cases. In addition, a Roa-Blackwellized particle filter will excel at processing non-linear states. However, since the EKF handles these non-linear states sufficiently with less computational burden, the EKF was selected for this thesis.

2.1.3 Magnetic Navigation Filter

There are three unique components that make up the states of the EKF that is used for MagNav. The first key component is the magnetometer measurement processor. A measurement processor is a way to update states of a filter (in this case the Kalman filter) to provide additional error correction. The second component is used to handle the inertial measurement unit (IMU) data. For the IMU data, a Pinson 15 error model as outlined in Titterton and Weston [16] is used. The third key component for the MagNav filter is an altimeter processor. In total the MagNav

filter has 17 states.

The magnetic measurement processor has several components: earth models, magnetic maps, compensation systems, and raw magnetometer measurements. These work together to estimate a measurement in the process described in (10).

$$h(\hat{\underline{x}}_{mag}) = \hat{x}_{fogm} + B_{map} + B_{WMM} + B_{cal} \tag{10}$$

Removal of the noise with the terms $\hat{x}_{fogm}$ and B_{cal} is crucial to navigation quality and is discussed in detail in Section 2.3. However, the filter is capable of modeling space weather and ionospheric noises and uses these models to produce $\hat{x}_{fogm}$. The calibration steps that are required to model aircraft noise sources, B_{cal}, before navigation can be performed are discussed in detail in Section 2.3.4. The calibration results are then used to estimate the contribution of the aircraft field to the total measurement. This contribution can then be applied to calibrate the sensor and remove noise sources. In addition to the required sensor calibration, MagNav requires a magnetic anomaly map. Maps are discussed in detail in Section 2.2. These maps are distributed in two forms, total magnetic field and magnetic anomaly field maps. If a magnetic anomaly map is used instead of the total field map, the core field B_{WMM}, must be calculated using the WMM [4], and added to the expected measurement. In general, adequate navigation results are achieved with sufficient calibration, and finely sampled magnetic anomaly maps which are not available worldwide. A block level diagram of the EKF MagNav system can be seen in Figure 2. It is important to note that this filter has not been tested at supersonic or hypersonic speeds, the latter of which is the primary goal of this paper.

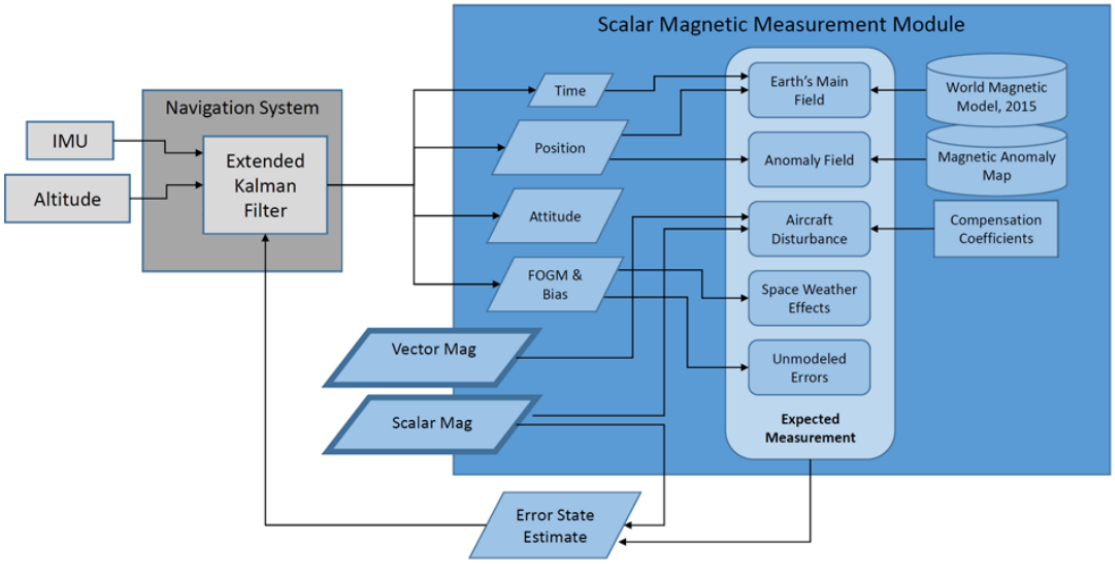

Figure 2: MagNav filter layout [3]

The next component of the filter is the Pinson 15 error model. This error model is used to estimate errors in the accelerometers and gyroscopes that are present on an IMU. These errors are then used to aid in correcting the mechanization process. The fifteen states present in the model are:

North Position Error (m)	Accel x-axis Bias Error (m/s^2)
East Position Error (m)	Accel y-axis Bias Error (m/s^2)
Down Position Error (m)	Accel z-axis Bias Error (m/s^2)
North Velocity Error (m/s)	Gyro x-axis Bias Error (rad/s)
East Velocity Error (m/s)	Gyro y-axis Bias Error (rad/s)
Down Velocity Error (m/s)	Gyro z-axis Bias Error (rad/s)
North Tilt Error (rad)	
East Tilt Error (rad)	
Down Tilt Error (rad)	

These states correct IMU mechanization errors that are defined by the parameters outlined in Table 1 [16]. IMU noise parameters vary by IMU grade and model. For

this paper, only navigation grade and tactical grade IMUs were used in simulation. Of these two grades, a navigation grade IMU will have superior performance. Mechanization is the process of taking IMU measurements and creating a position solution [17]. The Pinson mechanization errors are used as states within the MagNav filter to help correct the mechanization solution and make up 15 of the 17 total states.

Table 1: Table of IMU Noise Parameters

Noise Parameter	**Description**
Accel Bias	Biases which are proportional to the magnitude of the applied acceleration.
Gyro Bias	Bias which are proportional to the magnitude of the applied angular acceleration.
VRW	Zero-Mean Gaussian noise covariance of velocity random walk [2].
ARW	Zero-Mean Gaussian noise covariance of acceleration random walk [2].
Accel/Gyro Scale Factor	Errors in the ratio relating the change in the output signal to a change in the measured input rate.

The final key component is altimeter aiding. This assists the stability of the IMU mechanization by providing absolute altitude measurements, as a mechanized IMU is always unstable in the vertical channel. This system provides an altitude error state estimate to further reduce and bound IMU drift in the vertical channel. The final 17 filter states are outlined below [2]:

North Position Error (m)	Accel x-axis Bias Error (m/s^2)
East Position Error (m)	Accel y-axis Bias Error (m/s^2)
Down Position Error (m)	Accel z-axis Bias Error (m/s^2)
North Velocity Error (m/s)	Gyro x-axis Bias Error (rad/s)
East Velocity Error (m/s)	Gyro y-axis Bias Error (rad/s)
Down Velocity Error (m/s)	Gyro z-axis Bias Error (rad/s)
North Tilt Error (rad)	DC Bias (nT)
East Tilt Error (rad)	FOGM Bias (nT)
Down Tilt Error (rad)	

These states are propagated and updated using equations seen on Pages 115-122 of [2]. This concludes the review of the scalar MagNav algorithm.

2.1.4 Vector Magnetic Navigation

Vector based MagNav is an innovation on MagNav that replaces the scalar sensors with a vector sensor. This system shows promise for a sizeable increase in navigation accuracy [12]. This system faces three major issues. First is sensor availability. Currently, there are no off-the-shelf vector sensors that have performance comparable to scalar sensors. Vector sensors are prone to decreased measurement accuracy, increased noise, and thermal drift. These noise sources reduce the realistic viability of vector MagNav until improved sensors are available. Sensor availability has also created the second roadblock for vector MagNav, vector map availability. Currently, there are no high quality vector magnetic anomaly maps created with areomagnetic surveys. There are however a handful of satellite-based vector anomaly maps. The third major issue is extremely precise attitude requirements that are beyond what current systems are capable of. With improved vector sensors, attitude measurements, and expanded mapping efforts, vector MagNav will become an increasingly

viable navigation system.

Vector MagNav does not show a linear increase with respect to magnetometer readings. The underlying physics reasoning is seen in (11) [12].

$$\mathbf{B} = \nabla(\mathbf{\Delta U}) \tag{11}$$

This equation states that the magnetic field component (i.e. the vector magnetometer reading) $\mathbf{B}$ is the gradient of a magnetic potential field labeled ΔU. This yields the following equations for each vector component [12]:

$$B_x = \frac{\delta}{\delta x}(\Delta U) \tag{12}$$

$$B_y = \frac{\delta}{\delta y}(\Delta U) \tag{13}$$

$$B_z = \frac{\delta}{\delta z}(\Delta U) \tag{14}$$

Vector MagNav will not increase performance by three times over scalar MagNav, as all the new information is related. This relation forms as each axis of the vector field represent a gradient of the potential magnetic field. Instead, initial simulations demonstrate around a 50% increase in navigation accuracy of vector MagNav over scalar MagNav [12].

2.2 Maps

Current MagNav filters depend on looking up measurements within magnetic anomaly maps. Typically, these maps are surveyed in two ways. The first method, which produces the best results, is by flying a geo-survey aircraft at low altitudes. The second method is completed using satellite based collection systems, such the ESA Swarm satellite constellation [18]. The resulting survey data is then analyzed

to create a map. During the map creation process, there are two crucial survey elements: line spacing, and map altitude as magnetic fields are spatially related. It is also important to note that, maps created post GPS have increased accuracy as a result of more accurate surveys. This section will provide an in depth analysis of the effect of line spacing and map elevation, and an analysis of the survey processing procedure.

2.2.1 Map Elevation

MagNav is sensitive to both map survey altitude and navigation altitude [2]. If a flight is flown at different altitude than a non-upwards continued map, navigation accuracy will decrease due to sensor and map mismatch. For all cases, as altitude increases, navigation accuracy decreases. This decrease in navigation accuracy is the result of signal attenuation which occurs as the distance between the aircraft and the magnetic anomalies in the earth's crust increases. Map data collection from a geo-survey aircraft creates a low altitude map. These maps are typically no more than a few kilometers above ground level. Since the flight is done at a single altitude, an upwards continuation algorithm must be utilized to allow map querying at higher altitudes. This algorithm is a strategy to shift the maps altitude upwards. Upwards continuation acts as a low pass filter [2]. This filtering element of upwards continuation removes high frequency elements. Removal of these high frequency components will reduce the information available to the navigation filter, which will in turn reduce navigation accuracy.

$$U(x, y, z_0 + \delta z) = \frac{\delta z}{2\pi} \int_{-\infty}^{\infty} \int_{-\infty}^{\infty} \frac{U(x', y', z_o)}{[(x - x')^2 + (y - y')^2 + \delta z^2]^{\frac{3}{2}}} \delta x' \delta y', \tag{15}$$

$$\mathcal{F}[U_{z+\delta z}] = \mathcal{F}[U_z] e^{-\Delta z \sqrt{k_x^2 + k_y^2}}. \tag{16}$$

The upwards continuation operation for magnetic fields x and y, and their derivatives x' and y' between altitudes z_0 and $z_0 + \delta z$ can be seen in (15). The Fourier domain equivalent can be seen in (16) [19]. In this equation, $\mathcal{F}[U_z]$ is the Fourier equivalent of the map at the current altitude, k_x and k_y are the x and y magnetic fields in the frequency domains, and Δz is the change in altitude. Since the Fourier expression is more computationally efficient, it is the preferred expression.

Upwards continuation has two factors that can limit the navigation performance. First, as previously discussed, it slowly attenuates high-frequency magnetic signals. Second, upwards continuation introduces edge effects. Edge effects occur when a map is upwards continued significantly. After a certain altitude, sources from the area outside the map begin to influence readings. However, the map is unaware of these sources and thus upwards continuation will differ from the truth, resulting in corruption around the map's edges. The rule of thumb for avoiding these edge effects is for each kilometer upwards continued, the map should have 50 kilometers in each horizontal direction. Even with this rule of thumb, the outer 10% of the map becomes invalidated. Thus, for a flight that occurs at high altitudes, a much larger map will be needed [2]. The altitude compounded with the large distances covered by hypersonic vehicles results in the need to examine the viability of satellite-based maps.

Satellite-based maps are the result of downwards-continuing magnetic data collected from a survey satellite. These maps are at much higher altitudes, and can cover large sections of the globe with adequate accuracy. However, downwards continuation tends to be unstable, and it performs like a high-pass filter [2]. High pass filters can attenuate the frequencies used by MagNav, resulting in poor navigation results. The limitations of the native form of downwards continuation (mathematically expressed as upwards continuation with integration bounds reversed) restricts the maximum distance a field can be downwards continued. The primary factor that

limits downwards continuation is that there are infinite layouts for the individual magnetic sources that produce the same measurements at a higher altitude, making the end result ambiguous. However, other statistical and Taylor Series expressions for downwards continuation have shown promise as a more stable form of downwards continuation [20, 21]. In addition to this, the best satellite maps utilize aircraft-based surveys to further enhance their models. Regardless of enhancements, it is important to note that there is a high degree of uncertainty from downwards continuation, and no downwards continuation system is perfect. This thesis will seek to answer if downwards continued satellite-based maps are sufficient for MagNav at high altitudes on a hypersonic aircraft.

Satellite-based maps and data collections are readily available. An example of such a collection would be the ESA Swarm data collection [22]. This dataset was collected at altitudes ranging from 400-500 km. The maps generated from the three satellite constellation are vector maps sampled at 50 Hz resulting in sample spacing of around 160 m. The fluxgate magnetometers have around 1 nT accuracy. In addition, the swarm carries a scalar magnetometer capable of 1 Hz with 0.3 nT of accuracy and 0.1 nT of resolution [4]. This data is readily and publicly available and even has a Python API for ease of use. A picture of an ESA Swarm satellite can be seen below in Figure 3.

The use of satellite-based magnetic anomaly maps could be ideal for a case such as hypersonic aircraft. Since the altitude difference is only a few orders of magnitude, downwards continuation could be used. Maps such as Enhanced Magnetic Model (EMM) seek to perform downward continuation with minimal errors by creating harmonic models that detail the earth's magnetic anomalies. These maps combine tools and datasets like ESA Swarm and the WMM (a model of the earth's core magnetic field) to create a map of the earth's magnetic anomaly fields. Maps such as these

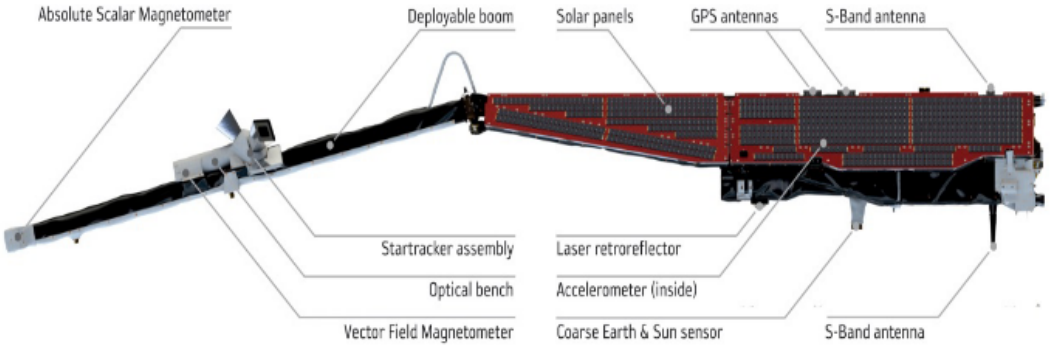

Figure 3: ESA Swarm satellite [4]

are relatively low resolution, with a maximum resolution of 2 arc-minutes (3.7 km at the earth's equator, with better resolution closer to the poles), and a height above the geoid of 4 km [23]. Due to the effects of downwards continuation, some areas of this map will not be highly accurate, however simulations at hypersonic speeds and altitudes will need to be conducted, to analyze the performance of the EMM compared to a traditional map created by a geo-survey aircraft. A picture of the magnetic anomalies mapped with EMM can be seen in Figure 4. One distinct advantage of the EMM is that it is also a vector map. This means that it can be utilized to simulate vector MagNav worldwide, albeit with reduced performance over a more finely surveyed vector map (however no such map exists).

2.2.2 Survey Quality and Processing

The distance between survey lines is called line spacing, and is a crucial part of magnetic anomaly map creation. In the ideal case, maps are surveyed with line spacing less than or equal to the survey height. These surveys are called fully sampled, and result in no loss in information when interpolating between sample points. This is because all relevant spacial frequencies are captured per the Nyquest Sampling

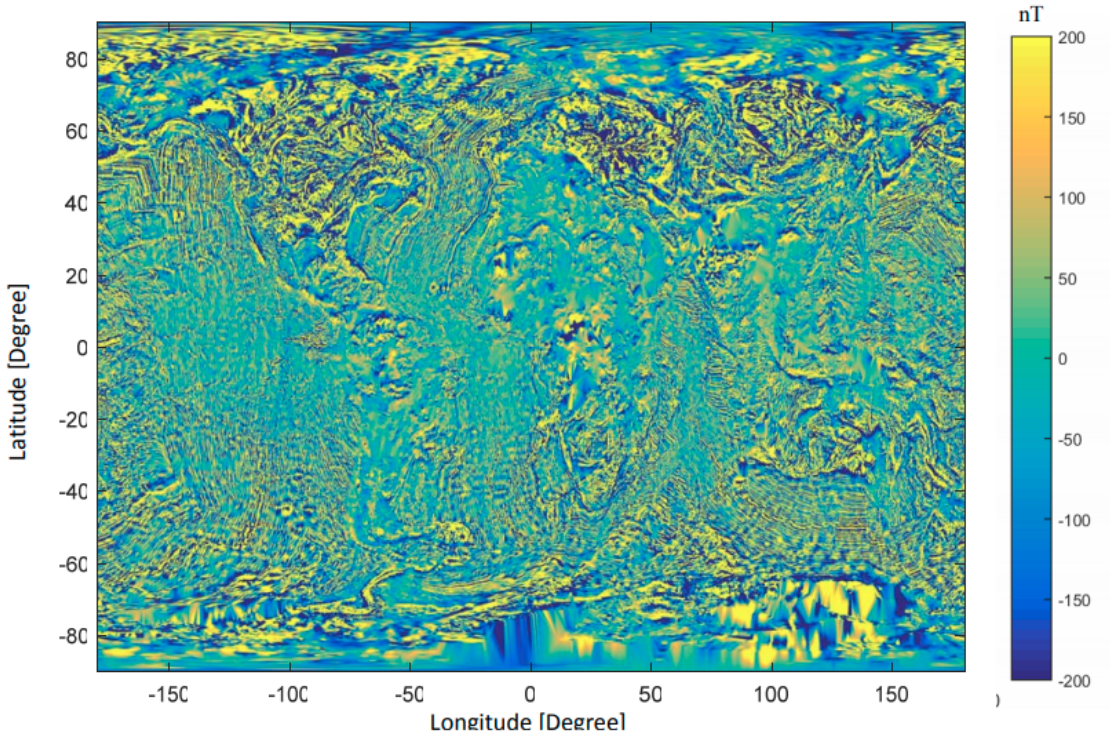

Figure 4: World Magnetic Anomaly Map [4]

Theorem [2]. However, due to budget and time constraints, surveys can end up under-sampled. This under-sampling can be alleviated by flying above the surveyed altitude. To showcase the availability of magnetic anomaly surveys, a map of surveys in the contiguous United States can be seen in Figure 5. The surveys shown in Figure 5 are compiled into a map of the magnetic anomalies of North America. This map is interpolated to a height of 1 km, and has line spacing from 1-8 km and is known as North American Magnetic Anomaly Database (NAMAD) [5]. This line spacing results in the map being significantly under-sampled in some locations.

The final step of map surveying is tie line surveying. This is done for map consistency and to create a smooth map at a constant altitude [7]. If this is not performed, maps become impractical to use. For the case of this paper, all maps have had these corrections performed. Since tie lines are not key for magnetic anomaly sampling, they have no effect on final map accuracy, and play no role in any upwards con-

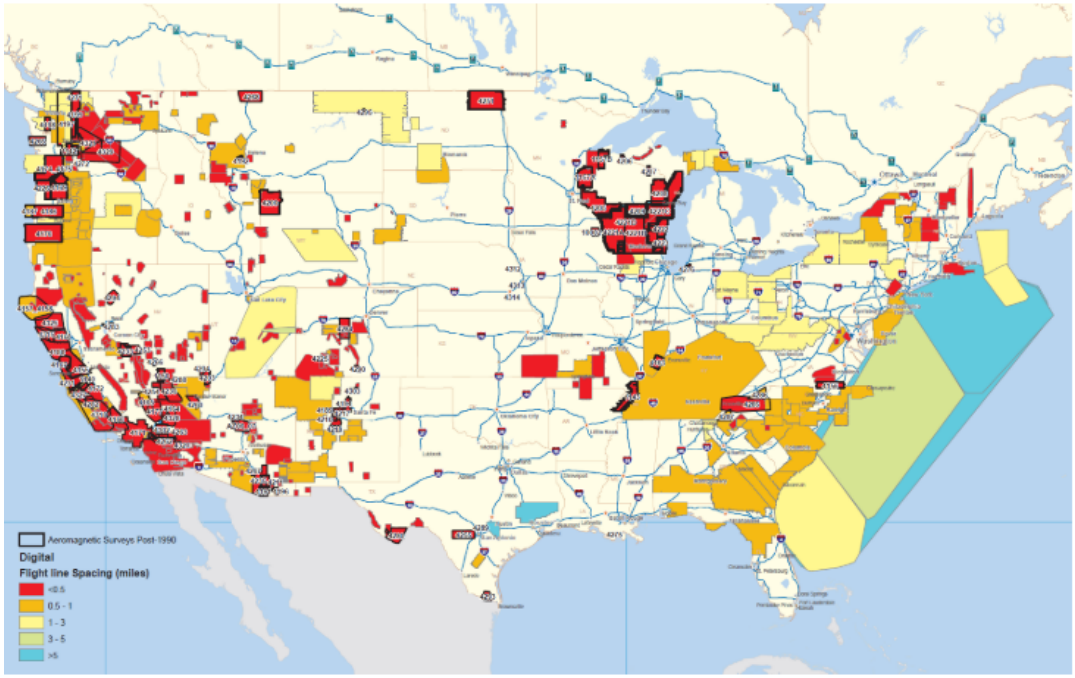

Figure 5: NAMAD survey map. Post GPS surveys outlined in black [2][5].

tinuation algorithm. A diagram detailing all survey elements can be seen below in Figure 6.

2.2.3 Australia Magnetic Anomaly Map

Even though magnetic anomaly maps are common; finely sampled, low altitude, post GPS maps are not common. Of these high quality maps, there are even fewer that span large areas. One example of a map that spans an area large enough to perform hypersonic flights is the Australia Magnetic Anomaly Map. This map covers the entire country of Australia. For this publicly available map, the surveyed altitude is 300 m, with close to 90 m grid spacing. This map is both finely sampled and low in altitude. While both of these qualities are ideal, the scope of this map makes it an ideal testing map for hypersonic trajectories. This map can be seen in Figure 7.

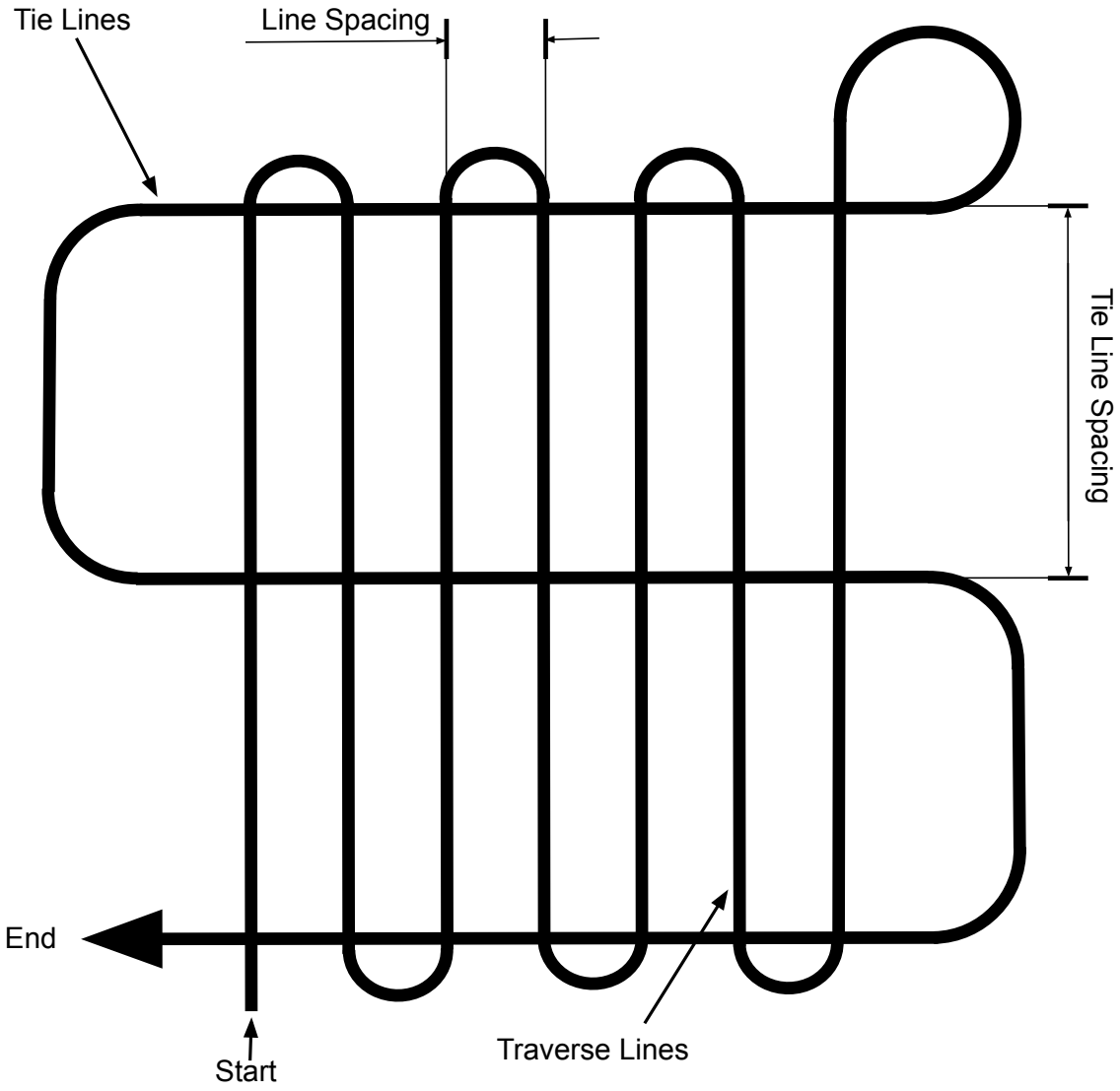

Figure 6: Diagram of map survey elements.

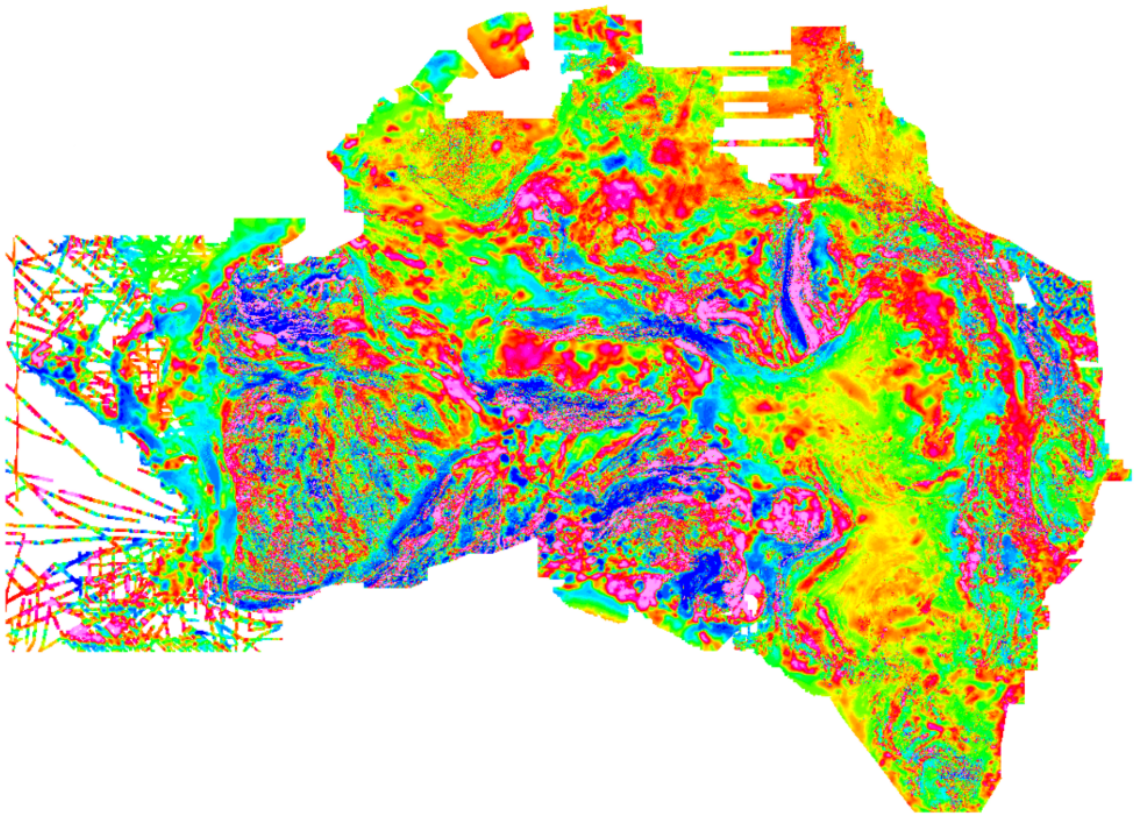

Figure 7: Australia Magnetic Anomaly Map. Note country wide availability with few un-surveyed sections [11].

2.3 Magnetic Noise Sources

There are a multitude of errors and distortions that can negatively effect the performance of a MagNav system. These errors mostly stem from four separate sources: the earth's main magnetic field, atmospheric noise, measurement noise, and aircraft sources. This section details these noise sources and the current calibration methods used to remove them.

2.3.1 Earth's Magnetic Field

The earth's magnetic field consists of two primary components, the core field and the anomaly field. When a measurement is collected it is the vector norm of the addition of the core field and the anomaly field vectors. Thus, once a scalar sensor has collected a measurement the core field has to be removed to obtain the magnetic anomaly field. The core field is induced by the movement of magnetic particles in the earth's core. The resulting movement of these particles generates a magnetic field in the order of 50 000 nT, which is significantly larger than the anomaly fields which are in the order of 100 nT [13]. Fortunately, the core field is a heavily studied topic and is characterized for elevations ranging from 1 km below to 850 km above the earth's ellipsoidal shape in the WMM [4]. The WMM is a publicly available model of the earth's core field, and for a given location will give an accurate representation of the earth's core field as a vector. For the case of MagNav, the earth's core field can be removed from the solution by taking the vector norm and subtracting it from the scalar magnetometer measurement. This results in the calibration and removal of the core field from the magnetometer measurement.

This calibration process does induce some error in the navigation solution. The WMM requires the location to be known to accurately provide a value for the core field [4]. This means that there is no solution unless an initial location is known. In

addition, as error in the final navigation solution increases, there is additional error in the core field calculation. However, core field values change in the order of 10 nT per km [4] and for any useful navigation solution this error will be negligible.

2.3.2 Ionosphere and Space Weather Induced Noise

Space weather and other atmospheric noise sources can induce significant measurement noise in addition to the earth's magnetic field. These noises can originate from many sources, however they all primarily originate from the sun. The primary noise sources in this vein are: ionospheric noise, magnetospheric noise, and coupling current noise. Combined these elements can induce up to 1870 nT of magnetic noise [2]. However, these noises change slowly and can be estimated and removed with filter estimation or by a base station.

Ionospheric noise originates in the ionosphere as a result of solar plasma. Solar plasma causes the formation of ions in the ionosphere. The movement of these ions in the earth's magnetic field create electric currents which in turn induce a magnetic field. These noises vary by location, season and time of day. As a result, ionospheric noise is best removed by information from a well surveyed base station where magnetic readings are known. The electric currents in the ionosphere are further increased by Equatorial Electro Jet (EEJ), which is the result of solar warming of the atmosphere [2]. In middle latitudes this noise is in the range of 40-50 nT, however closer to the magnetic equator these currents can contribute up to 200 nT of magnetic noise and are periodic every day[24]. The last source of noise in the ionosphere is the auroral currents. These originate from the sun's plasma stream and are dependent on the number of sun spots and season [24]. These are also periodic with respect to the 27-day rotation of the sun. In all, these errors can be removed with high accuracy via a surveyed ground station.

The next major noise source is the earth's magnetosphere. The magnetosphere is the area of the earth's atmosphere which is heavily effected by particles in the solar wind from the sun. The solar wind consists of protons and electrons which begin to interact and form currents and thus magnetic fields when they get close to earth. These currents are typically constant in altitudes in hypersonic flight ranges [25]. The solar wind can induce 20-30 nT of noise on a normal day, but during events such as geomagnetic storms that can occur with solar flares, there can be noise in the range of 100s of nano-Teslas [25].

The final major space weather related noise source are coupling currents. Coupling currents stem from the previous two different noise sources: ionospheric and magnetospheric. Since magnetospheric currents are solenoidal [25], they can occasionally cross into the ionosphere and couple with the sources there [25]. The coupling currents can result in 30-100 nT of errors at high latitudes. In addition to ionospheric coupling, there can be extra coupling noise induced near the EEJ. The coupling noise is in the range of 15-40 nT of error [2]. The coupling currents are unpredictable, however it is best to note that they are most noticeable near the earth's poles, and thus will add to difficulty when navigating in polar regions.

Removing ionosphere and space weather noise is done in two ways. By the use of a base station, all space weather and atmospheric errors are removable. However, base stations are not always available. As a result, the MagNav filter attempts to estimate these errors. Since these errors are highly periodic and characterized, the filter can estimate these errors with little effect on navigation results

2.3.3 Measurement Error

It is important to remember, that the current form of MagNav depends on magnetic scalar measurements. MagNav depends on scalar measurements for several

reasons. Three primary reasons for only using scalar measurements are: the most accurate magnetometers are scalar magnetometers, most anomaly maps are scalar maps, and lastly there is not a satisfactory way to estimate the needed aircraft attitude as needed for a vector magnetometer. In the case of vector MagNav, if there is an attitude error of 1°, the estimated calibration error from removing the 50 000 nT core field can be 873 nT. This means that without extremely precise attitude, vector MagNav is not feasible [12]. In MagNav, $|B_{anomaly}|$ is the desired measurement value, and what is found on maps. This value is found by subtracting earth's core field ($|B_{core}|$) from the magnetometer (17).

$$|B_{anomaly}| = |B_{total}| - |B_{core}|. \tag{17}$$

Since magnetic fields are vectors, this induces a slight error in the measurements as a result of the projection of the vector measurement to a scalar. Consider the following example:

$$B_{total} = B_{core} + B_{anomaly} = \begin{bmatrix} 50000 \\ 0 \\ 0 \end{bmatrix} + \begin{bmatrix} 1000 \\ 1000 \\ 1000 \end{bmatrix} = \begin{bmatrix} 51000 \\ 1000 \\ 1000 \end{bmatrix}$$

From these example values we get:

$$|B_{core}| = 50\,000 \text{ nT}$$
$$|B_{anomaly}| = 1\,732 \text{ nT}$$
$$|B_{total}| = 51\,019 \text{ nT}$$

In this example $|B_{total}|$'s true value is 51 019 nT. However, scalar addition results in a calculated B_{total} of 51 732 nT. This results in an error of 713 nT. However, the anomaly fields were exaggerated for the case of example, and in a realistic case the total distortion becomes fractions of nano-Teslas [2]. Consider the following example:

$$B_{total} = B_{core} + B_{anomaly} = \begin{bmatrix} 50000 \\ 0 \\ 0 \end{bmatrix} + \begin{bmatrix} 50 \\ 50 \\ 50 \end{bmatrix} = \begin{bmatrix} 50050 \\ 50 \\ 50 \end{bmatrix}$$

From these example values we get:

$$|B_{core}| = 50\,000 \text{ nT}$$
$$|B_{anomaly}| = 86.7 \text{ nT}$$
$$|B_{total}| = 51\,050 \text{ nT}$$

This results in: $|B_{total}|$ measured of 50 086.7 nT, and a $|B_{total}|$ of 51050 nT, which is a minimal error of 36.7 nT. Since most maps are created with scalar magnetometers, this measurement error will be present in map data as well. Since errors between magnetometer measurements and the magnetic anomaly map are consistent, magnetometer measurement errors have no negative effect on navigation results.

2.3.4 Aircraft Effects

A typical aircraft will have several magnetic sources that will induce a magnetic field. For survey aircraft like those seen in Figure 9 this is typically avoided by placing the magnetometer in a stinger far from the magnetic components of the aircraft. Moving the magnetometer away from the aircraft reduces aircraft noise as magnetic

fields decrease proportionally to the distance cubed as demonstrated in (18) [26].

$$B(r) = \frac{\mu_0}{4\pi}\left[\frac{3\mathbf{r}(\mathbf{m}\cdot\mathbf{r})}{|\mathbf{r}|^5} - \frac{\mathbf{m}}{|\mathbf{r}|^3}\right]. \tag{18}$$

This equation depends on three variables: permeability μ_0, magnetic moment vector $\mathbf{m}$, and the distance vector $\mathbf{r}$. Since the magnitude of magnetic sources on board the aircraft are relatively small, increasing the radius between the sources and the magnetometer nearly negates their effect.

The X-43A is a proposed hypersonic aircraft. This aircraft is made with composite materials. The design diagram provided by NASA, seen in Figure 8, showcases these material selections [6]. Due to the required high performance nature of a hypersonic aircraft, it is reasonable to assume that non-ferromagnetic materials will play a significant if not sole role in aircraft design and construction. Since these materials are non-ferromagnetic, they will introduce no magnetic noise into a MagNav solution. This means that it is likely that aircraft noise can be significantly reduced by placing the magnetometer far from away any ferromagnetic materials.

Regardless of magnetometer placement, some calibration will likely still be needed. Several modern calibration methods exist, but the base case is considered to be the Tolles-Lawson [27] calibration method. This calibration method assumes three magnetic sources: permanent magnetization, induced magnetization and eddy currents. To achieve Tolles-Lawson compensation, 18 total parameters are fitted with a least-squares method. This section will explain how Tolles-Lawson seeks to remove noise with calibration, in addition to more modern calibration approaches that show promise for better calibration results.

Permanent magnetization is the easiest to understand aircraft disturbance source. Any aircraft might have some small magnetic parts. These parts have permanent magnetic fields that will always produce some noise in the form of a static bias in a

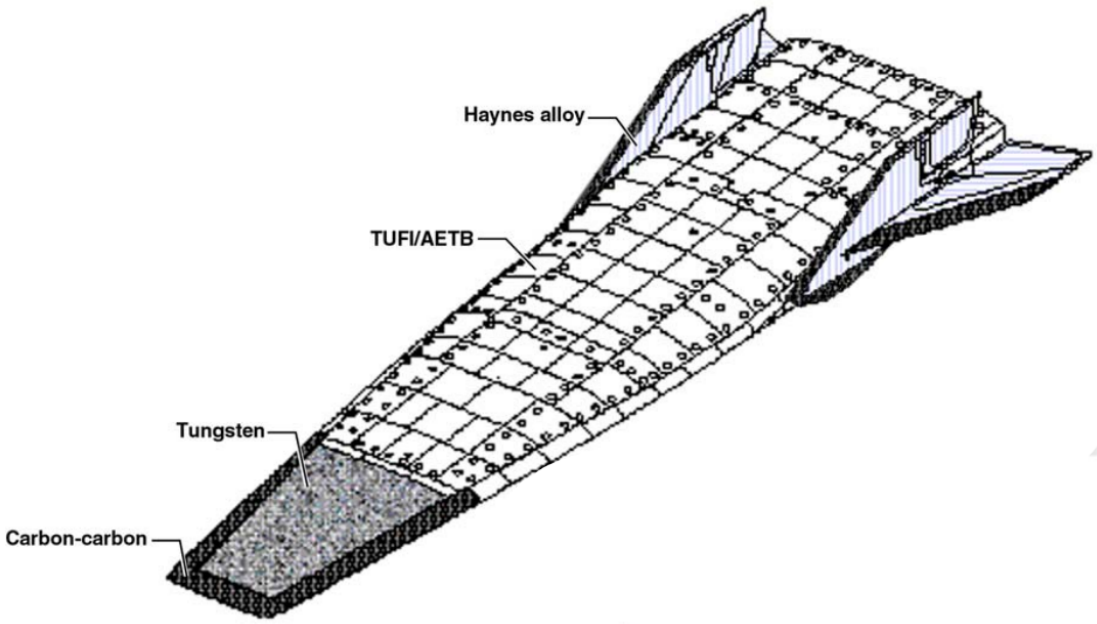

Figure 8: X-43A material choices [6].

magnetic measurement. This permanent field can be mitigated by de-gaussing. This is a process that can be performed on an aircraft to remove static magnetic fields [7], resulting in the mitigation of noise from the craft producing cleaner magnetic measurements. The first three terms in the Tolles-Lawson calibration calibrate the vector of the permanent sources [29].

The second major disturbance source is induced magnetization. Induced magnetization is the result of the aircraft moving in an external field. This field in turn induces magnetic fields in ferromagnetic materials inside the aircraft. Typically, this can have a minute affect as most aircraft components are constructed of aluminum and other non-ferromagnetic materials. However, any ferrous components will still induce magnetic fields that will produce noise [7]. Since the earth's magnetic field in the body frame (which is the same coordinate frame as the magnetometer) varies with heading, directionally dependent calibration is necessary. Directionally dependent calibration is typically completed through a calibration flight. This flight should

Figure 9: Sander Geophysics Limited survey plane. Note the magnetometer stinger [28]

be done in an area with few magnetic anomalies, as they will contribute to calibration errors [7]. The flight is typically done in the "clover leaf" pattern [7] seen in Figure 10. This pattern exposes the aircraft to most different directionally dependent induced magnetic fields. This flight pattern also requires slight rolls and pitches ($10-15°$), not seen in the figure. In order to compensate for the induced sources, the Tolles-Lawson calibration includes six calibration parameters for induced fields [29].

The final disturbance source that Tolles-Lawson seeks to calibrate out are eddy currents. These are magnetic fields that get induced in wires according to Lenz's Law, as a result of the aircraft moving through the earth's magnetic field [2]. Like the induced magnetization, eddy currents are dependent on aircraft orientation. Eddy currents have nine Tolles-Lawson parameters, for the magnetic field vector's changes with respect to each of the three attitude elements: roll, pitch, and yaw.

In addition to the sources calibrated by Tolles-Lawson there are a myriad of other potential noise sources. For example flight control surfaces, electronic components, aircraft engines, and other moving aircraft panels will all induce magnetic noise. For these noise sources there is little that can be done to remove them. Consequentially,

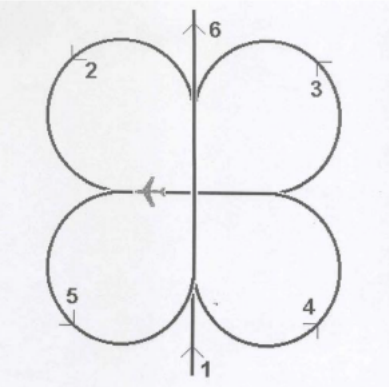

Figure 10: Tolles-Lawson Calibration Flight [7]

it is critical to place magnetometers as far away as possible from these noise sources. This will help calibrate the noise automatically. In addition, since MagNav depends on low-frequency signals, a low-pass filter might also help remove these noise sources.

Tolles-Lawson calibration is the current standard for areomagnetic platform compensation, however it is somewhat limited in its performance. There are several attempts to improve the effectiveness of calibration systems. An analysis of Tolles-Lawson shows that many of the tuning variables are correlated, resulting in less than ideal tuning, especially if data from all orientations is not collected [29]. This means a new approach with MagNav in mind is needed. This new approach has been a hot topic for research [3] [29]. For a typical survey aircraft the Figure of Mirit (FOM), which is the remaining un-calibrated noise, can be less than 1 nT [2], however this increases significantly when aircraft conditions are less than ideal and in the 10's of nano-Teslas [3].

A new calibration approach is to dynamically update a Tolles-Lawson model while navigating. The EKF is appended with the 19 states from a Tolles-Lawson calibration matrix. This results in the ability for the filter to continuously estimate the Tolles-Lawson coefficients, and also allows for compensation of the coefficients with respect to nearby magnetic anomalies. This system, notationally called "online calibration,"

results in close to a 50% improvement in navigation accuracy [3], however is not directly a calibration system.

2.4 Hypersonic Aircraft

Hypersonic vehicles travel at speeds that exceed mach 5 and altitudes up to 60 km [30]. As a result of their significant speed, extra considerations for navigation systems on hypersonic vehicles must be made. Within these speed and altitude bounds, flight characteristics can vary significantly and still be considered within the realm of hypersonic flight. Detailed studies of these characteristics can be seen in [30]. This section will give a brief overview of the characteristics of hypersonic flight, and how these unique characteristics can affect MagNav. Additionally, there are new noise sources that can conflict with magnetometer readings that need to be specifically analyzed.

2.4.1 Hypersonic Flight Characteristics

Hypersonic aircraft do not follow standard ballistic trajectories. Standard ballistic trajectories are parabolic in nature, whereas trajectories typically seen in hypersonic vehicles such as a Hypersonic Glide Vehicle (HGV) are lower and less predictable. This unpredictability results in the need for a navigation system, as the flight path is not left up to physics alone, and is instead controlled. The complex flight patterns of HGVs result in the need for a navigation system that provides a higher degree of accuracy than IMUs are capable of. A control system for a HGV, suggested by Lysak [8] is capable of guiding HGVs within 25 km of a random target. An example of a HGV trajectory can be seen in Figure 11. In addition to being on a dynamic path, HGVs can also switch destination during the course of the flight. This potential can be seen in Figure 12, where the HGV has the potential to strike a target anywhere

in the area outlined in blue. This area is known as the cross range [9]. The paths shown in Figure 12 are the result of Li's algorithm. Li's algorithm is an analytical method of determining a HGV flight-path [9]. The method suggested by Lysak [8] uses artificial intelligence to create HGV trajectories. This system shows significant improvements over Li's analytical system. Not only does Lysak's system produce better guidance results, it also allows for navigation around no-fly zones, a feature that Li's algorithm does not have. Lysak's algorithm is a significant improvement and provides a compelling base system to provide HGV trajectory data.

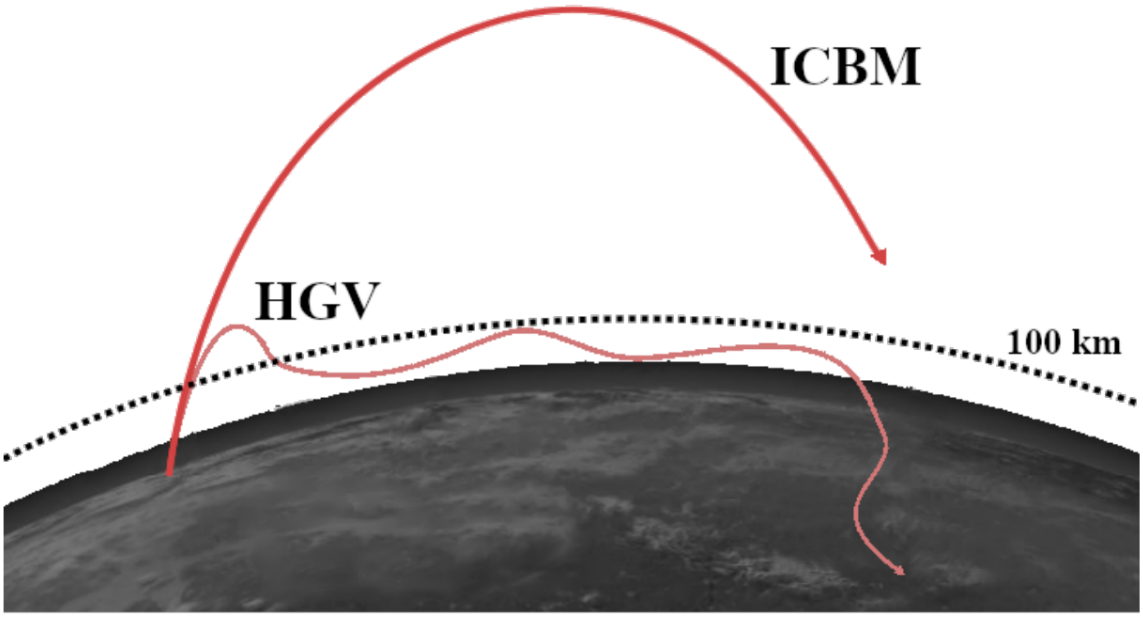

Figure 11: HGV vs ICBM Flight Path [8].

As a result of the altitudes reached in a hypersonic flight, a MagNav system's performance can be negatively impacted by magnetic signal attenuation [2]. However, performance degradation is partially offset by two factors: flight duration and speed. From the MagNav discussion in Section 2.1 it is noted that MagNav is responsible for bounding IMU drift. Hypersonic flights have shorter duration relative to normal flights. As a result, IMU drift (which is directly related to time) is significantly less.

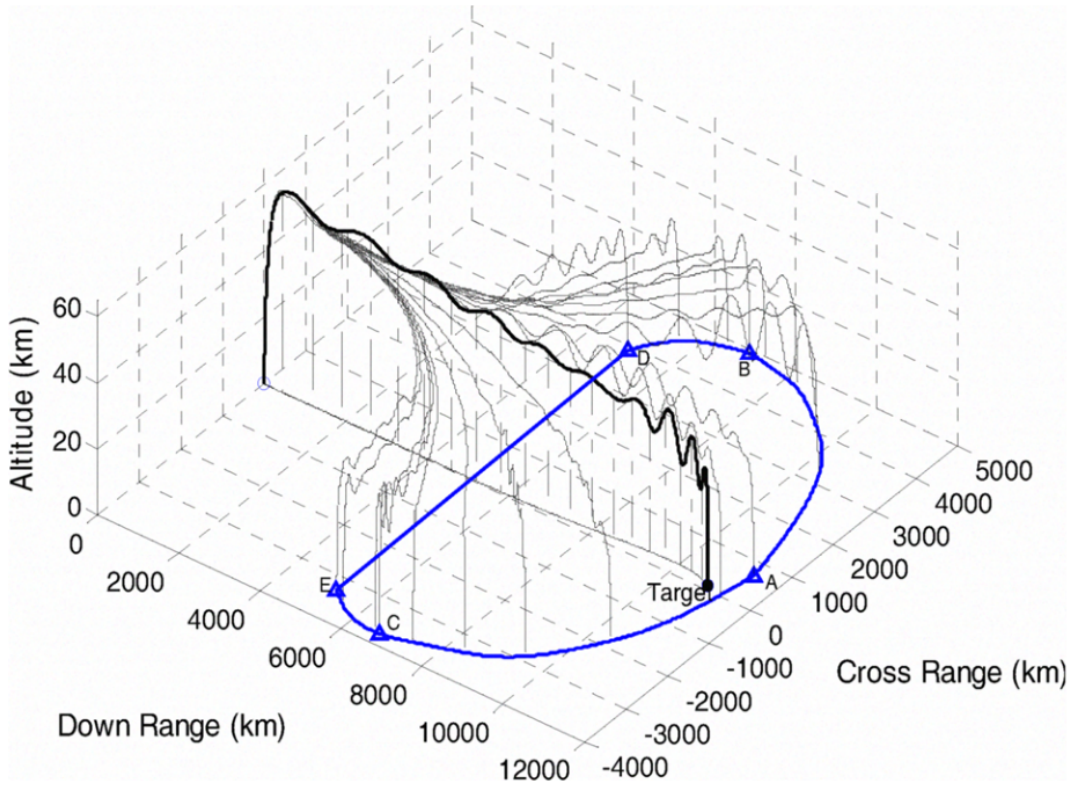

Figure 12: HGV Cross Range and Flight Paths [9].

Speed can also significantly increase the performance of MagNav. Since the flight is going orders of magnitude faster than a standard aircraft, a HGV will receive more magnetic information. This is because magnetic information is spatially dependent, and a faster moving aircraft will cover more space. Both shorter flight duration and increased aircraft speed should compound to help offset the negative effect of increasing flight altitude.

2.4.2 Hypersonic Aircraft Aerodynamic Effects

Hypersonic aircraft experience many aerodynamic effects from their high speed that normal aircraft do not experience. These effects can be broken down to three major types: inviscid flows, viscous flows, and high-temperature flows. Inviscid flows originate from shock-waves and other expansion and retractions happening in the

atmosphere and around the craft. Viscous flows are the result of the air passing around the aircraft. Lastly, high-temperature flows originate from the friction between the hypersonic aircraft and the atmosphere [30]. This friction heats the air and is responsible for creating a plasma sheath around the vehicle. The plasma sheath results in the loss of traditional communication systems [1] and is responsible for the re-entry blackout problem. To ensure that MagNav will not succumb to this blackout issue, an analysis of the magnetic permeability of the plasma sheath is presented in Section 2.4.3. These plasma effects can generate additional magnetic noise, in addition to blackout potential. A simple way to reduce plasma related magnetic noise would to place the magnetometer further away from the hotter areas where plasma will first generate. An example of how plasma formation can be spatially dependent can be seen in Figure 13. This figure shows areas of higher plasma density and are locations that magnetometers should be kept away from. A detailed study of the magnetic effects and noises generated by this plasma is beyond the scope of this paper. This paper explores a first order analysis of the plasma effects to ensure validity of the assumptions contained in the next chapter.

2.4.3 Plasma Effects

Plasma effects could distort magnetic fields at frequencies relevant to MagNav. We must explore these effects to understand how to properly calibrate a magnetic sensor in a hypersonic environment. Since MagNav depends entirely on the magnitude of the $\boldsymbol{B}$ field [2], we must understand how plasma can distort and otherwise change this element of a magnetic field. In addition to this, there is no need to consider any high frequency effects since MagNav only uses low frequencies to navigate.

A magnetic field $\boldsymbol{H}$ traveling through a medium with magnetic permeability μ

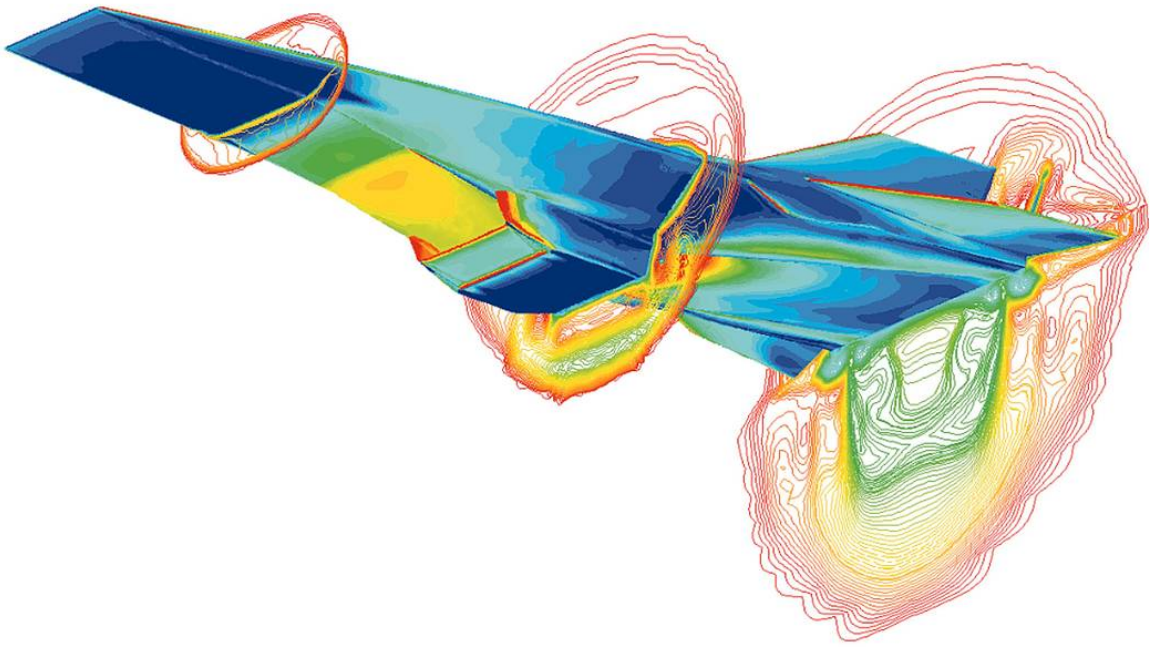

Figure 13: CFD image of X-43A [10]. Blue corresponds to lower plasma density, red corresponds to higher plasma density. Note how density is higher around forward facing surfaces.

results in $\boldsymbol{B}$ (19) [31].

$$\boldsymbol{B} = \mu \boldsymbol{H}. \tag{19}$$

We can see that it is crucial to define μ to better understand how penetration through a plasma sheath of a hypersonic aircraft will distort the magnetic field that will be used for navigation. For the case of navigation, the magnetic fields are low frequency, thus the needs of more complex permeability topics are irrelevant. Complex permeability is only relevant to enable the passing of electromagnetic fields through plasma sheaths [1]. Thus, for this study low frequency real permeability will be sufficient. However, further analysis of the magnetic noise from the plasma sheath generated at hypersonic

speeds should be performed.

For all types of matter, there are two different types of permeabilities: total (μ), and relative (μ_r). Relative permeability is defined as follows:

$$\mu_r = \frac{\mu}{\mu_0} \tag{20}$$

When the plasma is at low frequency, application of the Boh-Van Leeuwen theorem [32] can be used to obtain the relative magnetic permeability:

$$\mu_r = 1 + \frac{\mu_1^2 n_o}{3k_B T}. \tag{21}$$

Where n_0 is the total number of charged particles (in this case atoms, in the order of 1×10^{25} to 1×10^{30}), μ_1 is the magnetic moment of each charged particle (in the order of 1×10^{-24}), T is temp in kelvin and k_B is the Boltzmann constant. This results in $\mu_1^2 n_o \lll 3k_B T$. Analysis of (21) shows that as temperature (T) increases, relative permeability decreases to one, which is the permeability of free space (μ_0). This means that for extremely hot plasma (as is the case in a Hypersonic aircraft where the plasma is around 9000 K [30]), magnetic fields will travel similarly to a vacuum. [32, 33, 34, 1].

As a result of this analysis we will assume that the distortion created by the plasma will be minimal and removable by calibration algorithms. In the worst case scenario, where the plasma is cooler and with a larger magnetic moment, it can be expected to have a permeability similar to a non-ferromagnetic metal. Therefore, current calibration algorithms should be capable to handle the removal of the noise generated by plasma as long as the plasma produces constant noise. Should this not be the case, aircraft design techniques as described in [35] discuss the possibility of using complex permeability materials in order to negate the distortion of plasma.

Using these complex permeability materials, it should be possible to create a craft capable of allowing navigation regardless of plasma interference.

2.5 Summary

This chapter outlined the core literature available for the topic of hypersonic MagNav. The literature in this chapter points towards both the need for a navigation system for vehicles traveling at speeds greater than mach 5, partially due to the re-entry blackout problem. In addition, this section covered the potential issues that might arise when flying at hypersonic speeds for a magnetic navigation system. Lastly this chapter viewed in depth the current MagNav systems, their origins, potential limitations, requirements, and capabilities. From this detailed review it is clear that procedure presented in the next chapter stands upon a firm foundation of both need and result proven systems.

III. Methodology

This chapter covers the tools, key assumptions, and test setup for the hypersonic Magnetic Navigation (MagNav) simulations. The first key component of these simulations is the utilization of NavToolKit, a navigation framework. Next the key assumptions and their implications for navigation results are covered. Lastly, the simulation setup and design is covered in the final section.

3.1 Tools

3.1.1 NavToolKit

All navigation systems require a filtering system. Typically, this takes the form of an Extended Kalman Filter (EKF) or a derivative of this filter type. Fortunately, there are libraries available which are capable of handling the backend filtering operations. One such example of these libraries is NavToolKit. NavToolKit is the next iteration of Scorpion [36]. Like Scorpion, NavToolKit abstracts the backend of the filtering operation. As discussed in Section 2.1.2, the EKF has implementation dependent properties for both updating and propagating the filter. These dependencies vary by implementation. In NavToolKit, the implementation for updating is the measurement processor block. The purpose of the measurement processor bock is to handle estimation of measurements and their covariances. Since both of these are dependent on the user's application, they must be user defined. In the case of NavToolKit, this user definition takes the form of Python methods. This ease of use is a key contributor towards the selection of NavToolKit as the navigation framework.

NavToolKit was selected over other filtering libraries for two major reasons. Most importantly is that there is already an implementation for MagNav in NavToolKit. This eliminates the need to write the filter from scratch, and allows results in the

filter design process to be reduced to filter tuning. The second major reason that NavToolKit was selected is the ease of access. Installing and using NavToolKit is simple. For both the base library and the MagNav libraries, there are pre-existing Docker containers. This results in setup being greatly simplified. A block diagram of a MagNav filter that is designed in NavToolKit can be seen in Figure 2.

Filter design consisted mainly of components that were pre-existing in NavToolKit. To implement the filter outlined in Section 2.1.3, pre-existing Pinson15, and altimeter processors were utilized. These processors provided the needed filter implementation for both inertial measurement unit (IMU) and altimeter measurements. In addition, a general MagNav processor was created, this processor was capable of handling magnetometer measurements and providing aiding using a magnetic anomaly map. This implementation was not unique to hypersonic MagNav. It should be noted that all math was implemented as demonstrated by Canciani [2]. The final filter components that were required were bias and FOGM processors to process these aspects of MagNav. To aid stability, position, velocity, and attitude errors were compounded into the filter solution every sixty seconds. This completed the filter implementation in NavToolKit.

When running a filter for MagNav in NavToolKit the following information needs to be provided: IMU data, altimeter data, magnetometer data, and a properly formatted magnetic map. Additionally, true trajectory information should be provided to analyze results. However, this truth data is not required to run the filter. The process of providing the required measurements is the topic of the next section. Since map formatting posed a significant challenge for this thesis, it is covered in sections 3.2 and 4.2.

3.1.2 Hypersonic Path Maker

As discussed in Section 2.4.1, hypersonic trajectories are complex. A realistic hypersonic trajectory is not a straight line at a constant altitude between two points. A system that is capable of generating these trajectories is needed due to their complexity. Fortunately the machine learning system from Lysak's work [8] is available. However, due to updates in the library code, the system has to be retrained. This retraining was beneficial as it allowed for the removal of non-relevant data points in saved data. For the case of navigation we only are interested in latitude, longitude, altitude (as height above ellipsoid), roll, pitch, and yaw. Simple tweaks and a few hours of computation time allowed for Lysak's system to output 20 trajectories with the required data. This system was trained until it achieved performance on par with the results presented in Lysak's research.

Lysak assumed that all trajectories started at 50 km in altitude and terminated at 0 km in altitude. This assumption is accurate for a Hypersonic Glide Vehicle (HGV), but challenging for MagNav. For MagNav, lower altitudes require many finely sampled maps. This results in greatly increased memory usage on the simulation computer. In addition to the cumbersome map requirements for the low altitude, there is the issue of map availability. Most large scale maps are not accurate at altitudes under 300 m. Flying below these altitudes requires downwards continuation, which is unstable. As a result of these challenges, all altitudes were shifted up by 1200 m. This results in trajectories ranging from 51.2 km to 1.2 km. This is a relatively minor shift in altitudes. In a realistic scenario with altitudes under 1 km, the time to impact below map altitudes during which an IMU could drift would be minimal. Therefore, this assumption does not invalidate the realistic capabilities of MagNav for a hypersonic vehicle. This approach was chosen over turning off MagNav at the end of the trajectory to save memory and allow the use of a higher altitude base map.

The final adjustment to Lysak's algorithm was the need to select a starting location. The trajectories start at 0° N, 0° E. Since HGV trajectories can span several hundred kilometers, map availability was the deciding factor in origin selection. There are few maps that provide sufficient coverage as well as overall size to be upwards continued to the needed altitudes. There are some global maps such as Enhanced Magnetic Model (EMM), that allow for worldwide coverage. However, this coverage is at higher altitudes, with worse quality. Thus, all simulations were run within Australia. This provided access to the Australia Magnetic Anomaly Map, as well as the EMM.

The result of all the transformations and shifting of the trajectories can be seen in figures 14 and 15. These trajectories are compatible with NavToolKit, and ready to be used as a source of truth data. The final step that needs to be taken is the sourcing of measurement data. This process varied by sensor. For IMU data, raw measurements without noise were calculated with a reverse mechanization process. This process takes true latitude, longitude, height, roll, pitch, and yaw data and turns it into raw accelerometer and gyroscope measurements. For the required altitude data, this measurement is stripped directly off of the truth data, as a barometric or LiDAR altimeter will be able to provide such a measurement. Lastly, magnetometer data is read from the desired map at the true location. Since all of these processes are noiseless, they are not reflective of reality. As a result, noise must be added to each of the measurements. These noises are specified in Section 3.6.

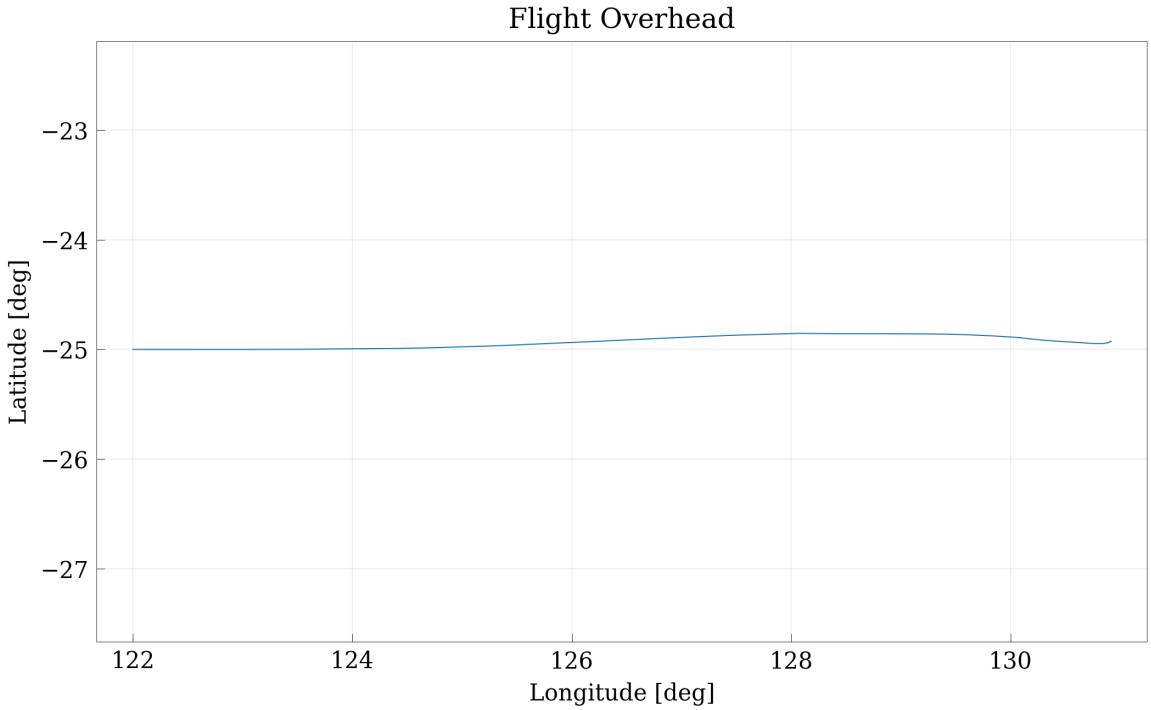

Figure 14: Example HGV trajectory (top view).

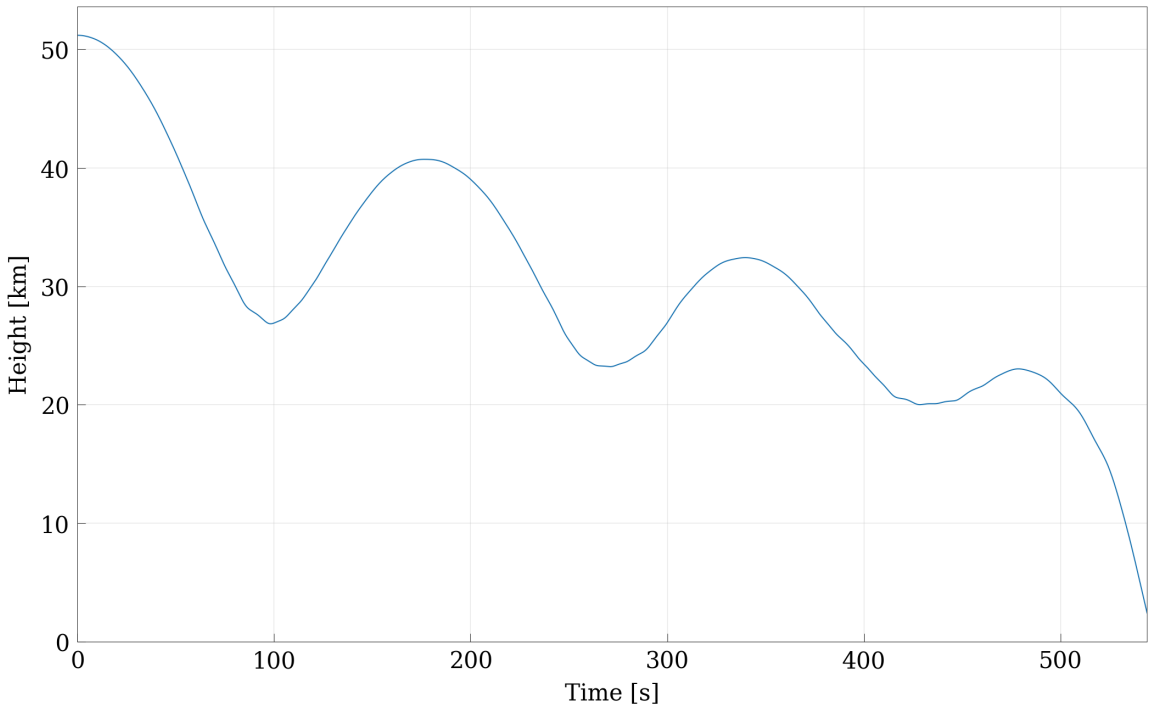

Figure 15: Example HGV trajectory (side view).

3.2 Map Analysis

All MagNav systems require maps. As discussed in Section 2.2, map quality is highly dependent on altitude, and spacing. A high quality map tends to be a modern map, with low altitude and tight spacing. These later two factors come with the cost of increased memory usage. Since hypersonic fights cover vast distances in short time, they require large maps. As discussed in Section 3.1.2, the trajectories were shifted upwards to help mitigate this issue. A higher altitude map can be down-sampled and still maintain the Nyquest sampling rate. This results in significantly reduced memory usage without negatively effecting navigation results..

Another factor that significantly increases memory usage is upwards continuation frequency. The prior map upwards continuation method was to upwards continue a short fixed distance, then use linear interpolation to obtain map values between the upwards continued altitudes. An example side profile of a map processed in such a way can be seen in Figure 16. Linear interpolation has the advantage of greatly reducing computation times as maps do not have to be upwards continued with every measurement. For large maps, upwards continuation can take close to a minute. Linear interpolation's computational speedup comes at the expense of introducing some map error. Due to the decreased computation time, this simplification strategy is a necessity for maps used in hypersonic MagNav. Map interpolation makes the assumption that all maps that are interpolated between have equal sampling spacing for the interpolation to properly work. The interpolation becomes more complex if sample spacing is not equal through the layers as vertical columns will be offset. Offset vertical columns invalidate the assumptions made in the interpolation code in libraries such as SciPy, which are used to implement these systems. Constant horizontal spacing means that the computer will have to have enough memory to store as many as 500 maps stacked vertically every 100 m in the case of our hypersonic

trajectories. With maps large enough for hypersonic trajectories, the interpolation and caching system becomes too memory intensive for most computers. For example, a single map layer that is large enough to cover an entire hypersonic trajectory can take up to 1GB of a computer's RAM. In the end, the best way to reduce memory usage would be to increase the vertical spacing between maps, thus lowering the number of maps required. Ideally map vertical spacing would be a fitted function that provides the needed delta distance up to the next map. This distance would result in less than 1 nT of error when linearly interpolating between maps. This error bound is chosen as it is both less 1% of the magnetic anomaly field and around the error that will be indistinguishable from sensor or calibration error. Ideally, this map system would result in a non-linearly vertically spaced map. This non-linear spacing is expected as the map information decays exponentially with respect to altitude. The attenuation of the magnetic fields is a decaying exponential process, and therefore it can be expected that most information lost from signal attenuation will occur at low altitudes. An example of such a map can be seen in Figure 17. There are two ways that this sparser spacing can be determined. The first is with the Power Spectral Density (PSD) of the maps, and the second is by simply measuring the interpolation error.

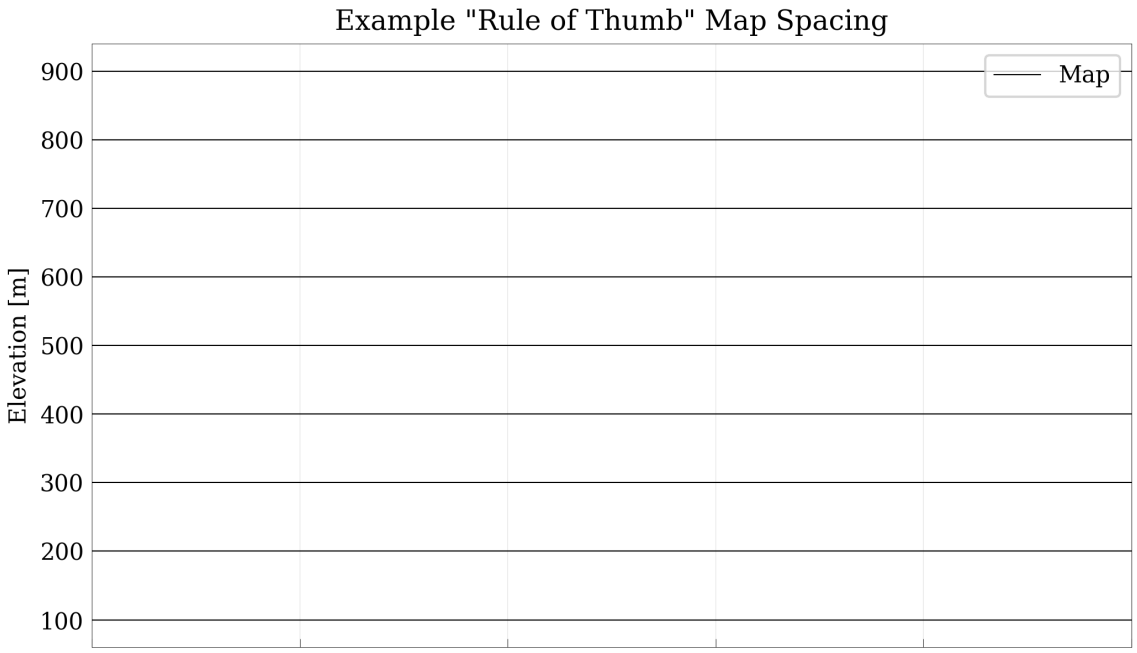

Figure 16: Example plot of linearly spaced map upwards continuation.

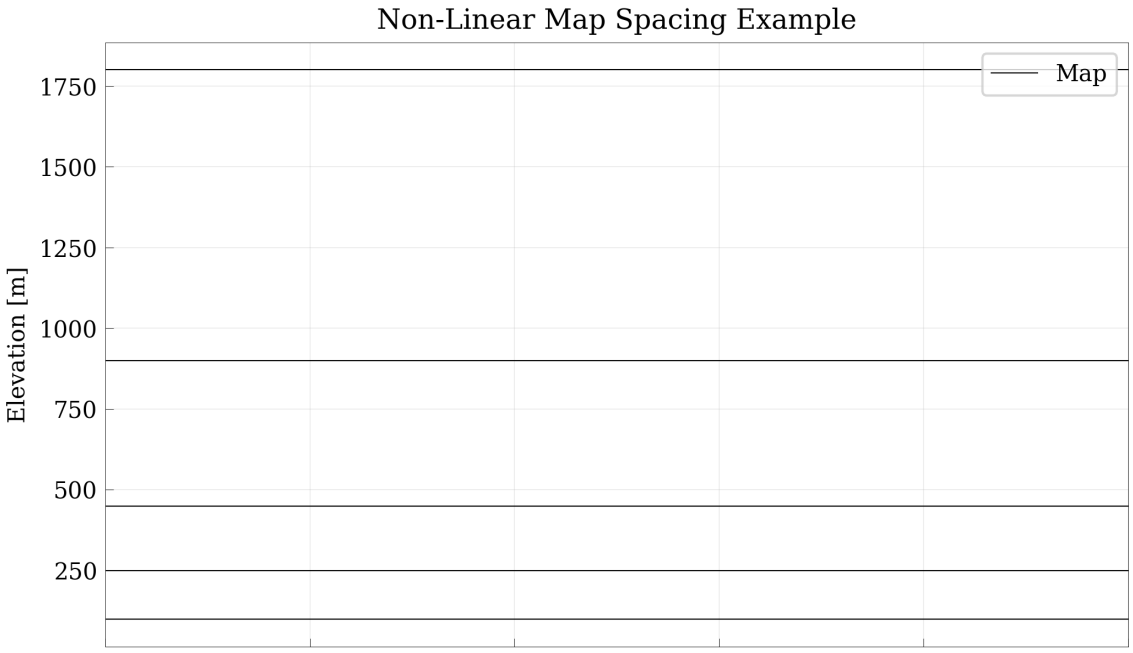

Figure 17: Example plot of non-linearly spaced map upwards continuation.

3.2.1 Power Spectral Density Map Analysis

The PSD of any signal shows how much of a signals power is contained in a certain frequency. This introduces a new method for determining the ideal upwards continuation interval. The average PSD shows the map power density with respect to upwards continuation distance. The goal of the PSD analysis is to show the upwards continuation interval which captures 99% of map power. In order to do this, maps are first finely upwards continued in a selected altitude interval. Then, for each latitude and longitude location on the map, a PSD along the vertical columns is computed. The result of this computation is the PSD of the frequencies in the vertical channel. Next, the grid of PSDs are averaged across all locations. Lastly, we can examine this average PSD and find the altitude spacing at the -20 dB point. For any spacial frequencies that are not captured by this altitude spacing, finer sampling becomes unneeded as 99% of all map information is already captured. This process is outlined in the flowchart seen in Figure 18.

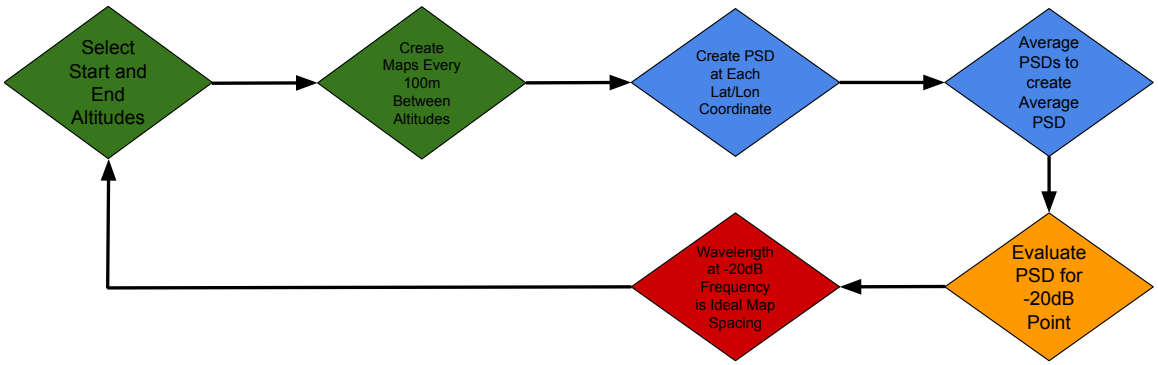

Figure 18: Flow chart of PSD analysis algorithm

This determined spacing from this algorithm is only valid in the selected altitude interval. After the algorithm has been ran for the interval, it will need to be repeated at the next altitude interval. This segmenting into altitude ranges is needed because this algorithm only produces a single altitude spacing and not a new rule of thumb.

An example of the end result of this algorithm for a single altitude range can be seen in Figure 19.

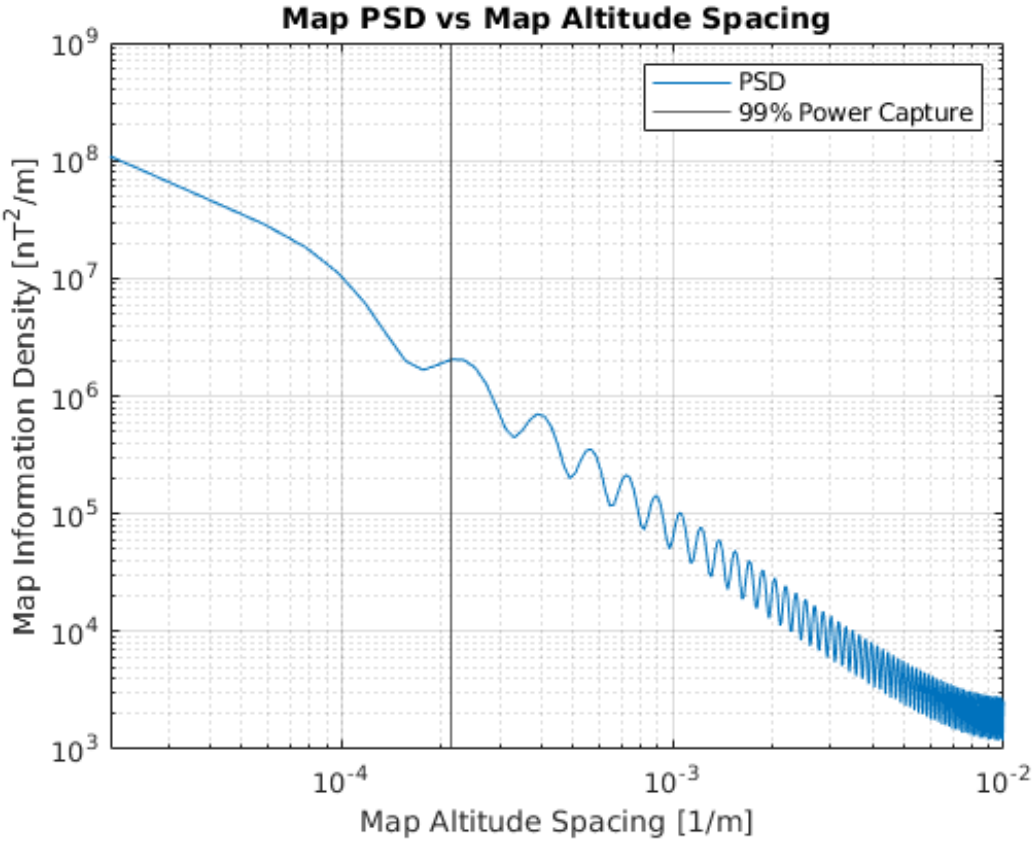

Figure 19: Plot of average PSD of Australia Magnetic Anomaly Map

It is important to perform map analysis over a large area. This is necessary as different areas have unique geological formations, which attribute to unique magnetic anomalies. This tends to create magnetically quiet and noisy areas. These areas in and of themselves can greatly impact navigation results. Thus, to get a significant result, a large map must be used. For this particular case, a finely sampled version of the Australia Magnetic Anomaly Map discussed in Section 2.2.3 was selected. A map of this scale provides more than sufficient data to provide a significant average for the required upwards continuation interval. This method is limited, as the map of Australia takes up a considerable portion of a computer's memory. To be viable, the

map of Australia has to be upwards continued and decimated reducing the overall information in the map and skewing the results. For example, a map of Australia that was upwards continued to 5 km and decimated to obey the Nyquest Sampling Theorem, when used in the above method, will produce different results compared to a 1 km in altitude map of the same area, regardless of altitude interval. This means that in order to produce significant results, low altitude, finely sampled maps must be used. This is not feasible due to memory requirements.

3.2.2 Measurement Error Map Analysis

The previous section outlined a method to determine the ideal map upwards continuation spacing. However, utilizing the PSDs becomes cumbersome to work with. A more computationally friendly process would be to simply compare the error between an upwards continued map and an interpolated map. This naïve process of determining error with this method is as follows. First, create an arbitrary list of test altitudes. Next create a set of finely spaced upwards continued maps, for example every 100 m. Then for each finely sampled map, calculate the mean absolute error between the upwards continued map and interpolated maps at each altitude. The results of this process can be seen in Figure 20. In this figure, the results were evaluated from 5 km to 50 km with a minimally sampled 5 km map.

Since the simple error analysis process requires maps every 100 m, the memory and computational burden of creating this analysis is significant. In addition, the maximum errors derived by this process range from 0.2 nT to 0.9 nT. This error range is not constant, which is a suboptimal result. The results from this simple process give an indication on how to improve the search. From the results in Figure 20, we can make the key observation that maximum error always occurs at approximately half of the delta altitude. This means that to see the maximum interpolation error,

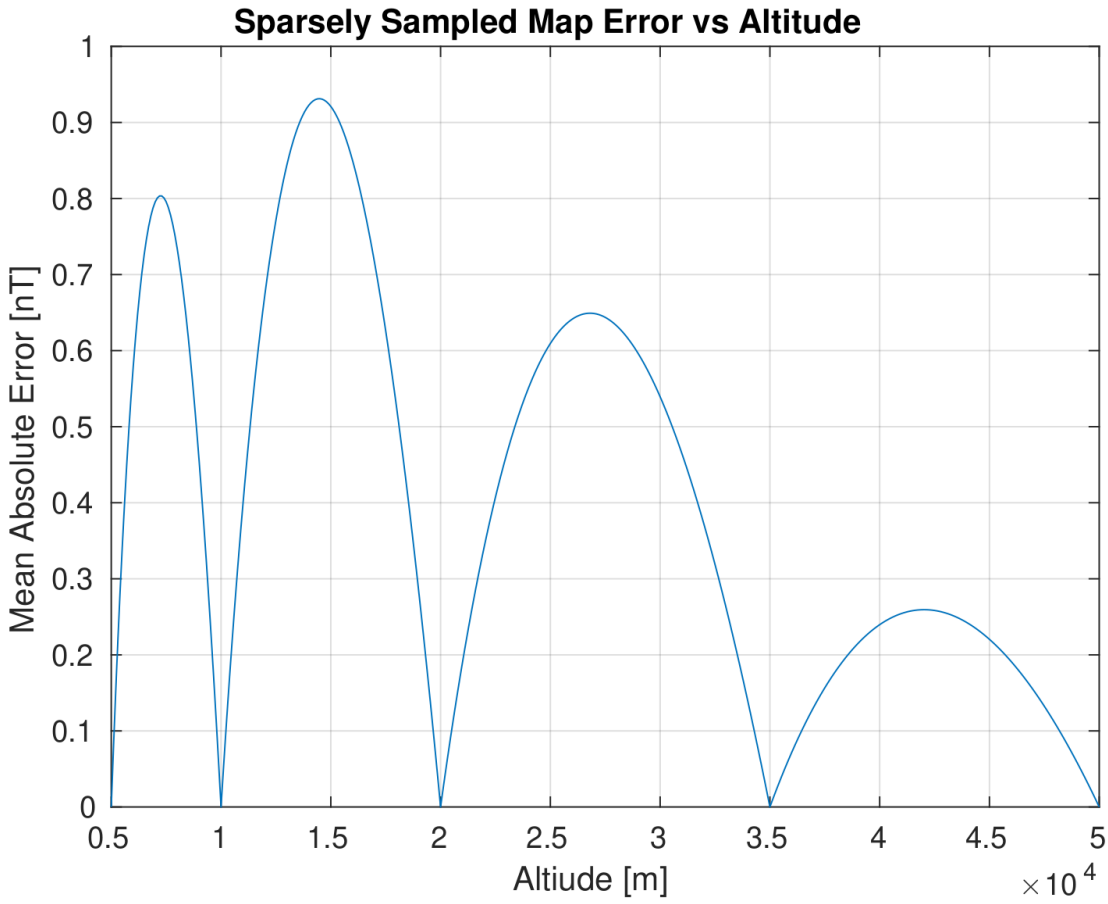

Figure 20: Naïve analysis of interpolation error

we only need to create two upwards continued maps, one at the maximum distance between maps, and one at half that distance. This leads to a computationally friendly algorithm which can be used to iteratively compute error to the desired value. The steps of the algorithm for the given parameters: starting altitude h, ending altitude h_{max}, max error err_{max}, min error err_{min}, and starting map map_{base} are shown in Algorithm 1. To clarify this process, a single iteration of this algorithm is illustrated in Figure 21. A flow chart of the entire process can be seen in Figure 22.

A 1 km upwards continued and down-sampled map of Australia was selected, to fully analyze the required upwards continuation distance with this method. This map was selected as it is the lowest altitude and finely spaced map of Australia that

Algorithm 1 Map Upwards Continuation Error Evaluation Algorithm

$\delta h \leftarrow 1000$
while $h < h_{max}$ **do**
    $map_{top} \leftarrow$ upwards continue map_{base} by δh
    $map_{mid} \leftarrow$ upwards continue map_{base} by $\frac{\delta h}{2}$
    $map_{interp} \leftarrow$ Interpolate all latitude and longitude points between map_{base} and map_{top}
    $err \leftarrow \text{MAE}[map_{mid} - map_{interp}]$
    if $err > err_{max}$ **then**
        $\delta h \leftarrow 0.75\delta_h$
    else if $err < err_{min}$ **then**
        $\delta h \leftarrow 2\delta_h$
    else
        $map_{base} \leftarrow map_{top}$
        $h \leftarrow h + \delta h$
        $\delta h \leftarrow 1000$
    end if
end while

could fit in memory with three copies. This map was then ran through the algorithm outlined above. The starting altitude was 1 km and the termination altitude was 60 km. The error bounds were between 0.89 nT and 0.9 nT. If a step (δh) was too small it was increased by a factor of 2, however if it was too large it was decreased by 25%. Since δh is expected to increase as altitude increases, these step adjustment parameters were established to favor higher altitudes. In addition, the initial δh was assumed to be an under-estimate thus it would be ideal to favor an increase of δh. The results of this analysis were then fitted to a 3rd degree polynomial function. For this function, the input is altitude and output is maximum map altitude separation. This implementation of the algorithm outlined above is capable of providing the desired results outlined at the start of this section. In addition, this method requires few maps to be stored in RAM at any given time, meaning that it can be run on a powerful personal computer instead of a server.

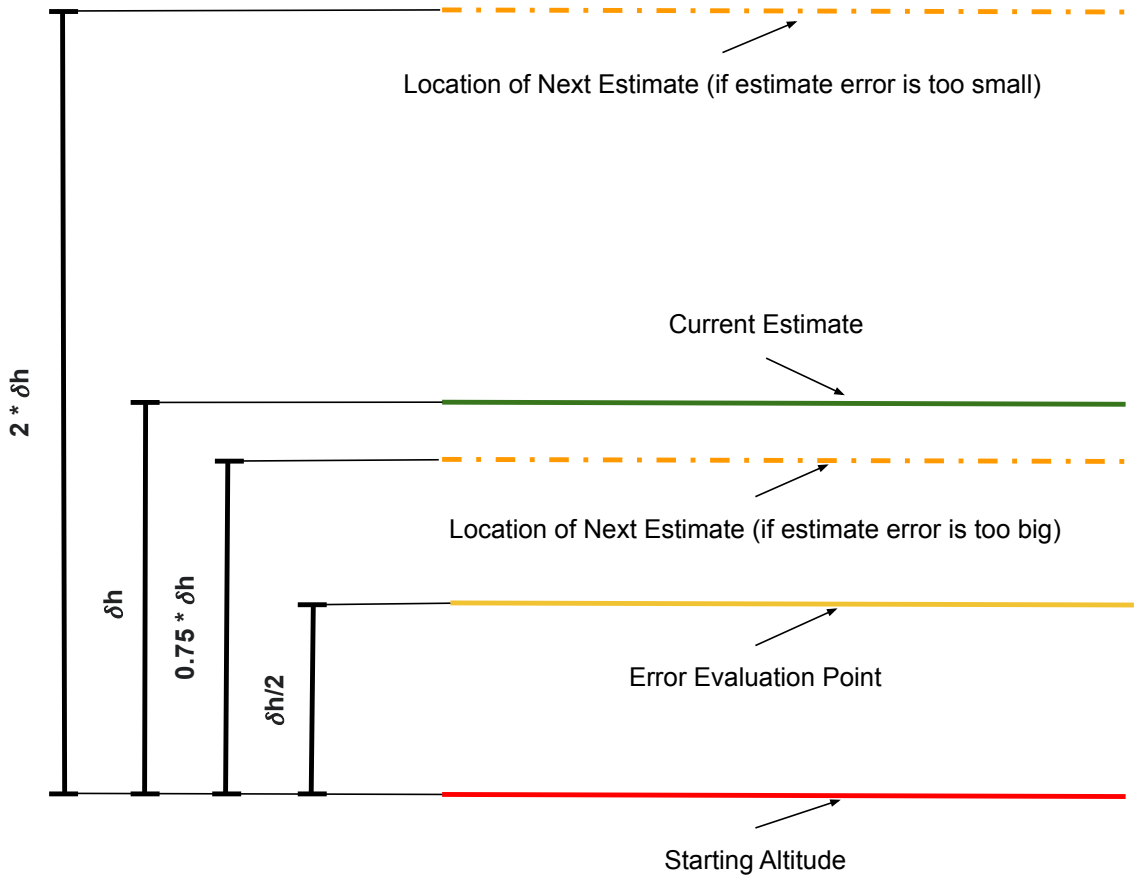

Figure 21: Illustration of single iteration of map error analysis algorithm

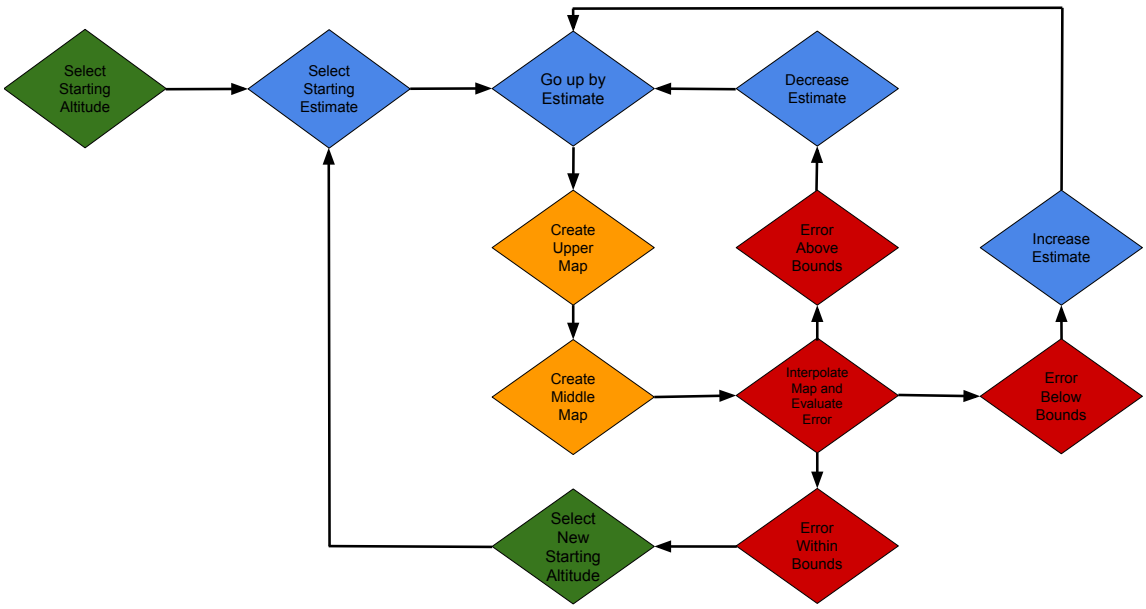

Figure 22: Flow chart of map error analysis algorithm

3.3 Map Availability

Aircraft surveyed magnetic anomaly maps that provide sufficient coverage to complete hypersonic trajectories are few and far between. The most desirable option for a large, finely sampled map is the anomaly map of Australia. This map can be seen in Figure 23. Due to the low survey altitude and finely sampled nature of this map, it is an ideal candidate for all forms of MagNav simulation. Most importantly however, the scale of the Australia map prohibits dominate edge effects at high altitudes. The standard practice for avoiding edge effects is utilizing the rule of thumb of 50:1 as discussed in Section 2.2.1. If the rule of thumb is followed, the outer 10% of the map becomes invalid. However, due to the substantial size of the map in comparison to the flown altitudes, most of the central areas of the map are valid for all altitudes of concern.

A second viable map type is a satellite surveyed map. These maps are discussed in detail in Section 2.2.1. The present major advantage of using these maps is that they are available world-wide. This means that any results presented are viable without any additional mapping required. The disadvantage to these maps is that they are inherently less accurate due to under-sampling. For the case of this simulation, the EMM [4] (see Section 2.2.1) will be used. Since the surveyed map of Australia represents the best possible case and the EMM is the best world-wide map readily available, simulations will be completed on both types of maps. For the case of the simulations using the EMM, magnetometer measurements will be provided from the Australia map. This is to model any potential disconnects between the map and the sensor values that may occur when flying with a world-wide map like the EMM.

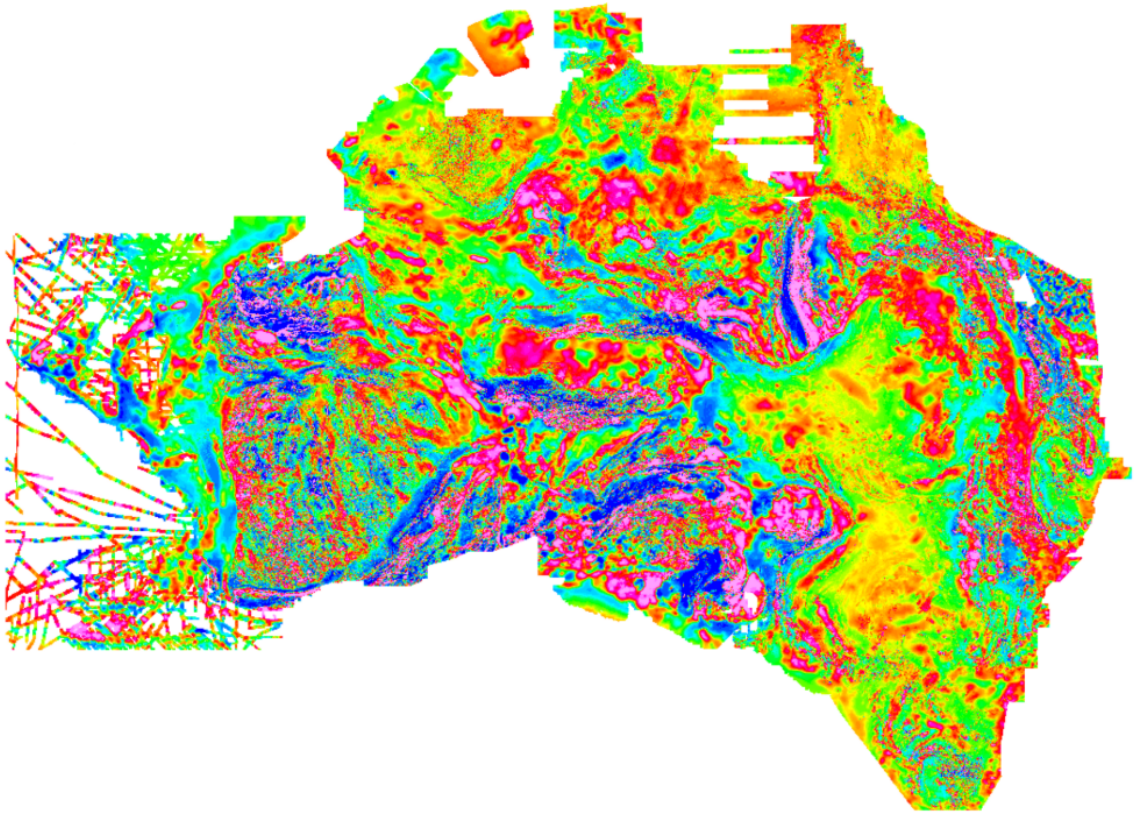

Figure 23: Australia Magnetic Anomaly Map [11].

3.4 Noise Sources

All noise sources need to be accurately profiled, to model MagNav on a hypersonic vehicle. Noise sources fall into two unique classes, magnetic noises and all other sensor noises. As discussed in Section 2.3 there are aircraft, space weather, and measurement error noises. These noises are non-unique to hypersonic MagNav. In addition to these three noise sources, hypersonic MagNav has to deal with plasma induced noise. Since IMUs and altimeters should be unaffected by hypersonic speeds, their noise models are also unaffected.

3.4.1 Aircraft Noise

To accurately simulate MagNav on a hypersonic aircraft, assumptions on must be made with regard to aircraft calibration and sensor noise. These assumptions are crucial for navigation quality, since access or flight testing is not possible on such an aircraft. The first key assumption rests on the improvement of magnetic calibration techniques. Approaches such as Online Calibration [3] show potential in reducing aircraft effects as discussed in Section 2.3.4. This points towards these effects becoming negligible. A second reasonable assumption lies in the use of composite materials and alloys in aircraft design. As discussed in Section 2.3.4, aircraft noise can mitigated by the use of composite materials. Lastly, the magnetometer used for navigation can be placed in a more magnetically quiet location on the aircraft. Calibration methods are able to remove most noise, based on both aircraft materials and calibration improvements. Remaining noise will be indistinguishable from sensor measurement noise since the remaining noise is marginal.

3.4.2 Space Weather Magnetic Noise

Magnetic noise from space weather is well modeled as a First Order Gauss-Markov (FOGM) noise, as discussed in Section 2.3.2. For these simulations, space weather noise is modeled with a time constant $\tau = 600$ and deviation $\sigma = 1$. This is a conservative estimate for space weather noise. This noise profile is a sufficient model, as space weather noise is correlated with the daylight cycle and hypersonic flights are short in comparison.

3.4.3 Magnetic Sensor Measurement Noise

1 nT of white noise is added to all measurements to model sensor errors. This noise profile is in range with readily available magnetometers. So far, these noise sources

are not specific to hypersonic MagNav. The next section will cover the hypersonic specific case of magnetic noise from plasma sources.

3.4.4 Plasma Noise

The noise generated from plasma can be significant as discussed in Section 2.4.3. However, the following assumptions are made:

1. Magnetic Noise from plasma is a high-frequency noise that can be removed with a low-pass filter.

2. High Frequency noise does not alias with the sensor readings.

3. Remaining noise can be mitigated by moving the sensor as far away from plasma as possible.

Plasma's magnetic effects, and its removal by calibration, filtering, and physical separation remain a mostly unexplored area of research and will be left to future works. We will assume that plasma effects can be removed with a low pass filter in this research. An example of the total noise, that is added to magnetometer readings can be seen in Figure 24.

3.4.5 Other Sensor Noises

IMU model(s) had to be selected to establish noise parameters. Two different IMUs were selected for these simulations. The first was a Novatel HG9900 navigation grade IMU and the second was a Novatel HG1700 tactical grade IMU. The noise parameters from the data sheets for these two IMUs can be seen in Table 2.

For all trajectories, a significant improvement with the HG9900 navigation grade IMU is expected. However, due to the short duration of the typical hypersonic flight,

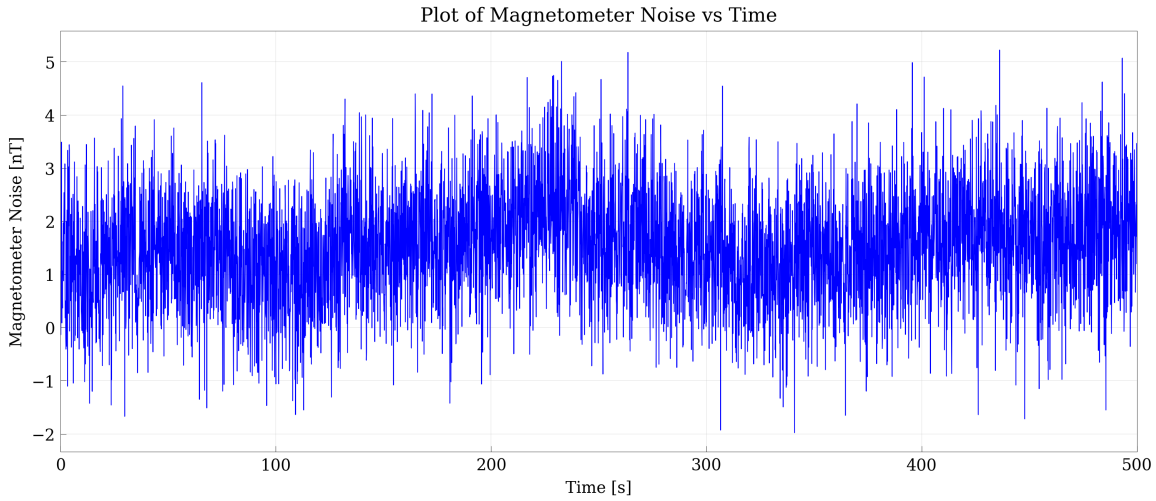

Figure 24: Magnetometer corrupting noise profile. Note that since this profile is of noise, it will vary significantly with each realization. This noise is a FOGM noise with $\tau = 600$ s and σ=1 nT, with additional zero mean white noise with $\sigma = 1$nT

Table 2: Table of IMU Noise Specs

Noise Parameter	**HG9900**	**HG1700**
Accel Bias (ug)	25	1000
VRW (fps/sqrt(hr))	0	0.65
Gyro Bias (deg/hr)	0.003	1
ARW (deg/sqrt(hr))	0.002	0.125
Accel Scale Factor (ppm)	100	0
Gyro Scale Factor (ppm)	5	0

running a lower grade IMU such as the HG1700 will produce results that better highlight the function of the navigation algorithm.

An altimeter is used to assist the IMU. This altimeter measurement provided to the filter is the true altitude, but corrupted with white noise with a standard deviation of 1 m. This noise is representative of a LiDAR altimeter. Since IMU mechanization is extremely sensitive to errors in the vertical channel, altimeter aiding is a key tool to help constrain IMU instability. The altimeter is a requirement for all IMU based navigation systems as the IMU is unstable in the vertical channel.

3.5 Vector MagNav Simulation

As discussed in Section 2.2.1, the EMM also functions as a vector map. This will allow for simulations of hypersonic trajectories using vector MagNav. Establishing the filter and simulations for vector MagNav is mostly trivial given prior assumptions.

The first step of establishing the filter for vector MagNav requires the creation of a new measurement processor for NavToolKit. While this process is normally non-trivial, there is the advantage of a pre-existing scalar measurement processor. This results in the majority of the code being exchangeable between the two systems. The second simplification rests on the calibration assumptions outlined in Section 3.4. For all simulation cases it is assumed that all magnetometer readings arrive to the filter pre-calibrated, this greatly simplifies the process and is consistent with the assumptions made for scalar MagNav. This means that no additional effort is needed to implement the calibration system for vector MagNav outlined in [12]. One potential issue that can arise in the creation of the measurement processor is the transformation of map measurements to the correct coordinate frame. Map measurements and sensor measurements need to be in the same coordinate frames for the filter to function correctly. For this implementation, the map measurements were transformed to the body frame which is the same frame as the sensor. This transformation was completed using the aircraft's estimated attitude and the following rotation matrix [17].

$$\boldsymbol{R}_n^b = \begin{bmatrix} \mathrm{c}_\theta \mathrm{c}_\psi & \mathrm{c}_\theta \mathrm{s}_\psi & -\mathrm{s}_\theta \\ \mathrm{c}_\phi \mathrm{s}_\psi + \mathrm{s}_\phi \mathrm{s}_\theta \mathrm{c}_\psi & \mathrm{c}_\phi \mathrm{c}_\psi + \mathrm{s}_\phi \mathrm{s}_\theta \mathrm{s}_\psi & \mathrm{s}_\phi \mathrm{c}_\theta \\ \mathrm{s}_\phi \mathrm{s}_\psi + \mathrm{c}_\phi \mathrm{s}_\theta \mathrm{c}_\phi & -\mathrm{s}_\phi \mathrm{c}_\psi + \mathrm{c}_\phi \mathrm{s}_\theta \mathrm{s}_\psi & \mathrm{c}_\phi \mathrm{c}_\theta \end{bmatrix}, \tag{22}$$

Where 's' and 'c' are the sine and cosine functions, respectively. In this rotation matrix ϕ is roll, θ is pitch, and ψ is yaw. Using this rotation matrix, all vector magnetometer measurements can be rotated into the body frame from the navigation

frame by simple matrix multiplication.

Simulation for vector MagNav mostly follows the same parameters for noise and trajectories as the other simulations. The only exception to this is for the vector magnetometer measurements. All these measurements are sourced from the EMM. Since the EMM only provides measurements in the navigation frame, they must be rotated into the aircraft's body frame to simulate what a real sensor would observe. This transformation is done using the trajectory's true attitude measurements. Noise of an identical profile to the scalar magnetometer's noise is added to each of the vector magnetometers axes independently. This is an overly optimistic profile of an existing vector magnetometer, however not outside the realm of future improvements to sensors. After the new filter components are created and sensor measurements are simulated, the filter is run using the same parameters used for the other MagNav simulations.

3.6 Simulation Design

A simulation environment was created with a NavToolKit based filter, to simulate hypersonic MagNav. This simulation environment takes the form of a Monte Carlo Simulation. Monte Carlo simulation allows for performance analysis of a myriad of potential magnetic anomaly fields. The performance of MagNav is dependent on these anomaly fields, and varying the trajectories on a series of fields provides a more complete analysis of overall system performance. In addition, Monte Carlo Simulations are necessary to simulate the varying sensor noise that will occur. The program performs the following operations for the Monte Carlo Simulations:

1. Read in HGV trajectory
2. Optionally shift HGV trajectories to a random location in Australia.

(a) If trajectories are not shifted start the trajectory at -25° N, 122.0° E and fly mostly eastward.

3. Ensure that the randomized HGV trajectories are bounded by the following locations:

   (a) Trajectory cannot exceed -19° North

   (b) Trajectory cannot be below -29° North

   (c) Trajectory cannot exceed 143° East

   (d) Trajectory cannot be below 126° East

4. Corrupt the true altitude readings from the trajectory with a realistic altimeter noise profile.

5. Generate magnetometer readings from the respective magnetic maps.

6. Corrupt the magnetometer readings with a realistic sensor noise profile.

7. Reverse-mechanize noiseless IMU data with the true trajectory.

8. Corrupt IMU with noise based off of specified model.

9. To simulate longer flights, provide the filter with a randomly distorted initial positions. This simulates initial position uncertainty.

Each trajectory's respective Monte Carlo Simulation was run fifty times with each applicable setting. The following Monte Carlo Simulations are planned to fulfil our simulation goals:

1. One trajectory with the same starting location performing MagNav on the Australia map with a navigation grade IMU. This is to test filter tuning and will take 50 runs of the simulation to complete.

2. One trajectory with the same starting location performing MagNav on the Australia map with a tactical grade IMU. This is to test filter tuning and will take 50 runs of the simulation to complete.

3. Five trajectories with a random starting location performing MagNav on the Australia map with a navigation grade IMU. This will provide system performance analysis with a high quality map and navigation grade IMU and will take 250 runs of the simulation to complete.

4. Five trajectories with a random starting location performing MagNav on the Australia map with a tactical grade IMU. This will provide system performance analysis with a high quality map and tactical grade IMU and will take 250 runs of the simulation to complete.

5. One trajectory with the same starting location performing MagNav using the EMM as the map with a navigation grade IMU. This is to test filter tuning and will take 50 runs of the simulation to complete.

6. One trajectory with the same starting location performing MagNav using the EMM as the map with a tactical grade IMU. This is to test filter tuning and viability of using a tactical grade IMU for this navigation problem and will take 50 runs of the simulation to complete.

7. Five trajectories with a random starting location performing MagNav using the EMM as the map with a navigation grade IMU. This will provide system performance analysis when using the lower quality EMM and flying with a slight sensor and map mismatch. This will take 250 runs of the simulation to complete.

8. One trajectory with the same starting location performing vector MagNav to

test filter tuning. This will take 50 runs of the simulation to complete.

9. Five trajectories with a random starting location performing vector MagNav to test the overall performance of vector MagNav. This will take 250 runs of the simulation to complete.

10. Five trajectories with an unaided navigation grade IMU for an IMU only baseline. This will take 250 runs of the simulation to complete.

11. Five trajectories with an unaided tactical grade IMU for an IMU only baseline. This will take 250 runs of the simulation to complete.

In total 11 different types of simulations will be run, resulting in 1 750 individual Monte Carlo runs. This is to provide a complete performance analysis of MagNav's performance characteristics for hypersonic flight.

3.7 Conclusion

In this chapter we established the key requirements, assumptions, and simulation parameters needed for hypersonic MagNav. Many of the parameters set here dictated the direction of research presented in this thesis. The results of simulation for hypersonic MagNav are presented in the next chapter. The twofold goal of these simulations are to reduce the computational burden of MagNav on large trajectories, and to test the viability of MagNav on hypersonic aircraft.

IV. Results and Analysis

4.1 Introduction

This chapter will analyze the results from the simulation process. The results are broken down into four major sections: Map Analysis results, Australia Magnetic Anomaly Map navigation results, Enhanced Magnetic Model (EMM) map navigation results, and vector Magnetic Navigation (MagNav) results. Since map analysis was a requirement for all other results, this chapter will begin with the results from this process.

4.2 Map Analysis Results

Extensive refinements for map processing were required, due to the significant map area requirements for hypersonic MagNav. Maps must be both large and multi-layered, since hypersonic trajectories cover significant areas and altitude ranges. The target for simplifying these maps is reducing the total number of layers as discussed in Section 3.2. The Australia Magnetic Anomaly Map was prepared for use in the algorithm outlined in Algorithm 1. This map started as the base version of the Australia Magnetic Anomaly Map, with 300 m altitude. Sample spacing is 92 m and 82 m in the North and East directions respectively. The map was upwards continued to 1 km, to make the map more memory friendly. Then the map was down-sampled with decimation to sample spacings of 828 m and 738 m in the North and East directions respectively. The map was saved to disk for future use, as this process was memory and somewhat time intensive.

The next process of the map analysis was to create Algorithm 1 in MATLAB. MATLAB was chosen, as at the time, there was no way to load the Australia Magnetic Anomaly Map in Python. After creating the algorithm, error bounds and altitude

bounds were selected. Since map interpolation error should never exceed 1 nT, the err_{max} bound was selected as 0.9 nT. Allowing an error margin of 0.1 nT. Minimum error, err_{min}, of 0.89 nT of was selected to provide a tight bound. Since the hypersonic trajectories ranged from 1.2 km to 51.2 km, the altitude range of $h = 1$ km and h_{max} = 60 km were chosen. These altitudes fully encompassed the hypersonic trajectories.

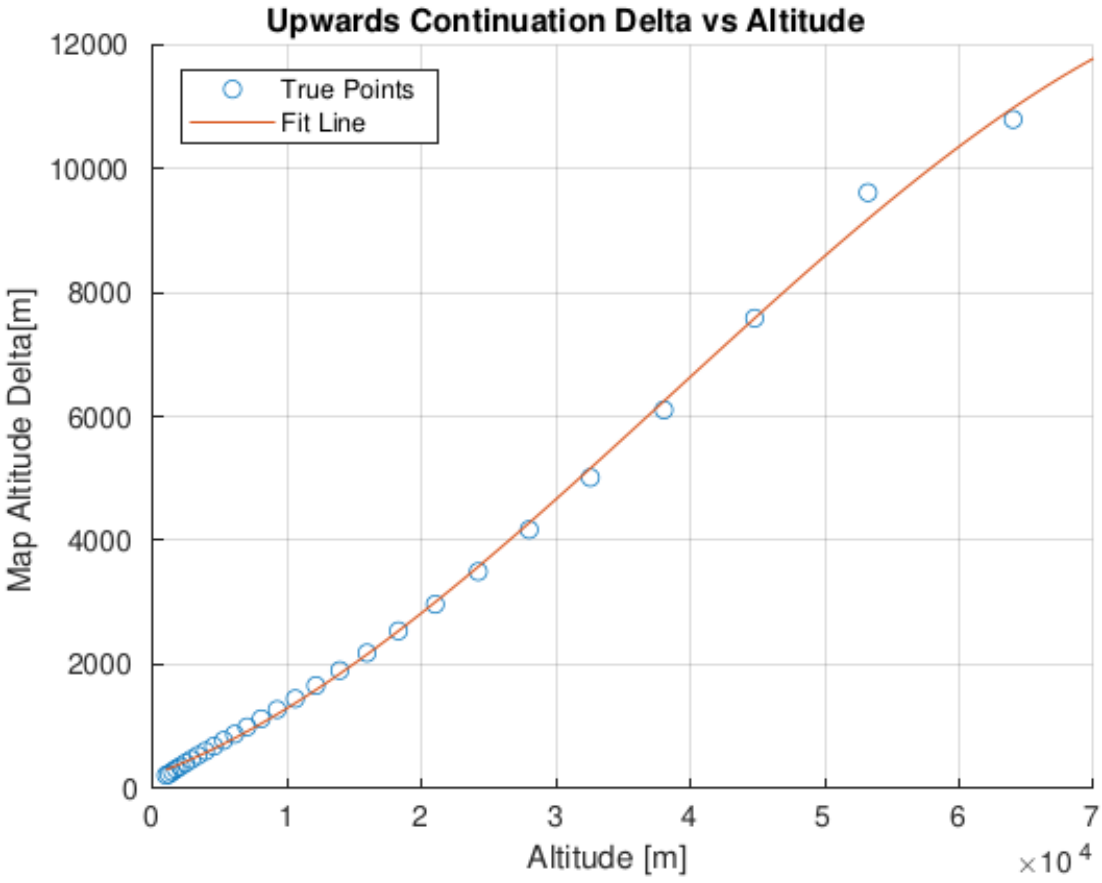

Figure 25: Map vertical spacing with error not exceeding 1 nT. Fitted polynomial shown in orange.

The final map vertical separation can be seen in Figure 25. This y-axis of this figure shows us the map vertical separation distance in meters given the altitude in meters indicated on the x-axis. The polynomial that can be used to estimate this is

seen below in (23).

$$\delta h = -2.69 \cdot 10^{-11} h^3 + 3.1122423 \cdot 10^{-6} h^2 + 7.91633650395 \cdot 10^{-2} h + 214.1758332070125 \quad (23)$$

In (23), the delta altitude is represented by δh and the current altitude is represented by h. The true points indicate that for altitudes contained within the used hypersonic trajectories, only 28 maps will be required. This means that memory usage will be under 30 GB. This is a significant improvement from the 100s of gigabytes that would be required by the old system which would require 500 maps to span this same altitude range. As a result of these improvements, further simulation is feasible. These simulations will be covered in the next section.

4.3 Map Based Simulations

For this section of navigation simulations, the Australia Magnetic Anomaly Map was used as the base map. As was the case in Section 4.2, the map was upwards continued to 1 km and down-sampled to sample spacings of 828 m and 738 m in the North and East directions respectively. With improvements in the MagNav utilities for NavToolKit and the sparse map spacing discussed in Section 4.2, this map and all required altitudes were able to easily fit in system memory. To avoid repeat computation, all map layers were precalculated and saved to disk, saving countless hours of time in debugging and simulation. This was all the needed preparation required for the magnetic anomaly maps.

To ensure that the filter was functioning correctly the filter was evaluated over the same trajectory with an initial position of $-25°$ N, $122.0°$ E. Since this trajectory covers the same location, filter estimated covariance will be consistent. With

the results from the fifty Monte Carlo simulations, the true filter covariance can be calculated and compared to the estimated covariance. If the filter's estimated and true covariance from the Monte Carlo simulation are close, and the covariance bounds the majority of the solutions, then the filter is functioning as intended.

The first step to perform these simulations is selecting initial position uncertainty. For these simulations the initial position uncertainty was selected to be 500 m in both the northing and easting directions, and 10 m in the vertical direction. These bounds were selected to demonstrate the constraining capabilities of MagNav for hypersonic trajectories. Next, measurements were generated and corrupted with the process outlined in Section 3.6. Lastly, the filter could be run. To preserve results between filter runs in the event of an unexpected error, filter results were saved to the disk after each run of the filter.

The filter was run for both navigation and tactical grade inertial measurement unit (IMU)s. The results of these simulations can be seen in figures 26 - 31. These figures show that the filters are well tuned, and the covariance is well bounded. Since this is the case, the filter is functioning as intended. The overall achieved performance for these Monte Carlo simulations is 547.86 m and 2252.91 m of Distance Root Mean Squared (DRMS) error for navigation and tactical grade IMUs respectively.

Running MagNav is highly dependent on magnetic anomaly information for navigation accuracy. To showcase the magnetic information available, the raw magnetometer readings that have not been corrupted by noise for the trajectories analyzed can be seen in Figure 32 below.

These results, especially in the northing direction, seem underwhelming. One explanation for the poor performance is the relatively flat north/south magnetic field gradient in comparison to the east/west gradient. This flat gradient reduces the information that MagNav is able to provide to reduce IMU drift. The two gradients

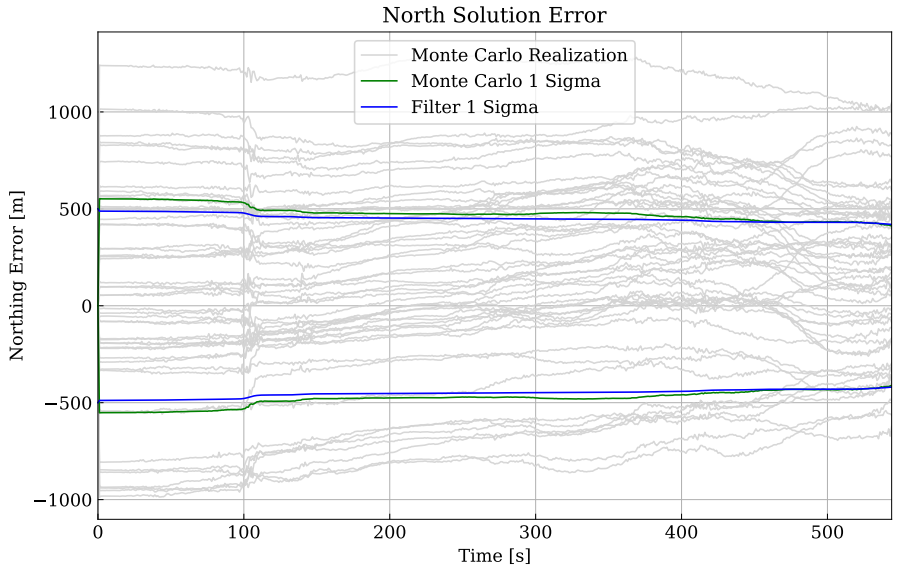

Figure 26: Navigation grade IMU filter tuning northing results. In these results we see that the estimated filter standard deviation (blue) closely follows the Monte Carlo standard deviation (green). Both of these standard deviations well bound the Monte Carlo runs shown in gray.

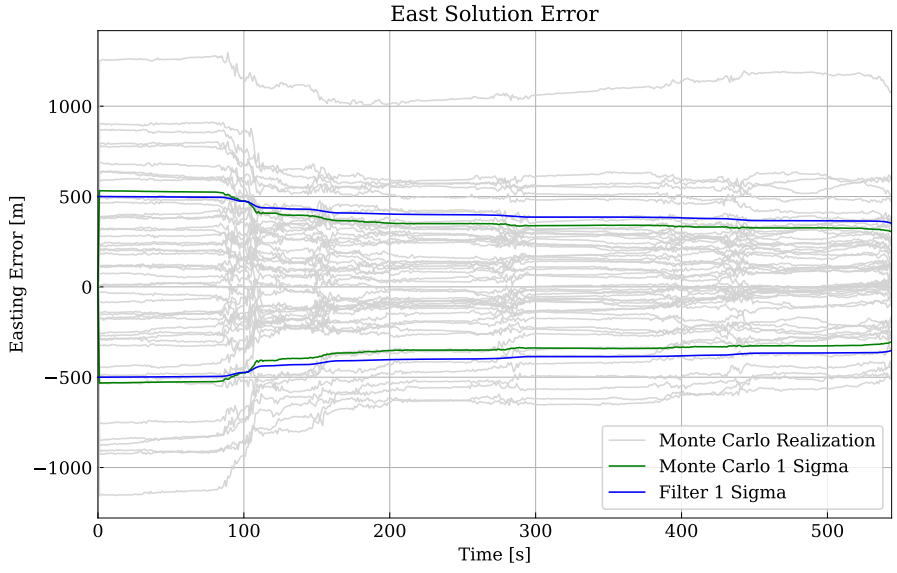

Figure 27: Navigation grade IMU filter easting evaluation results.

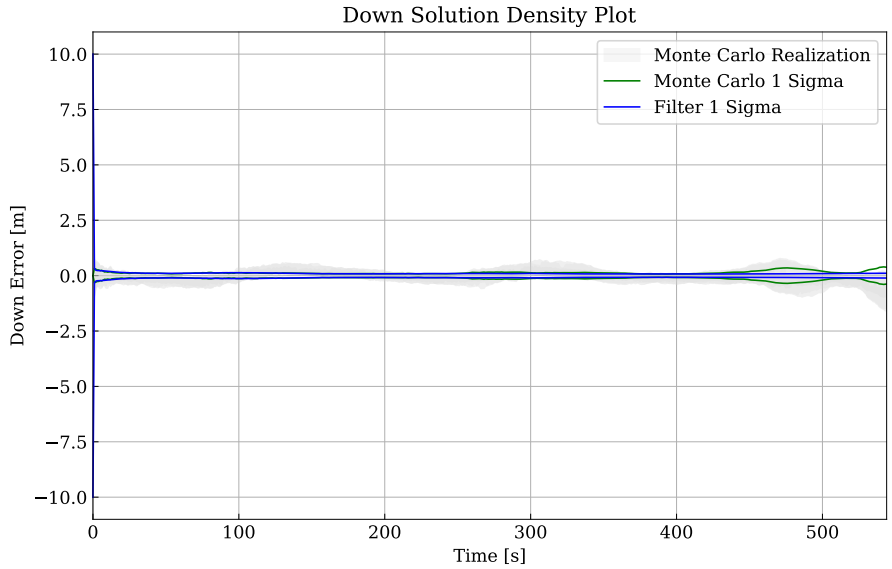

Figure 28: Navigation grade IMU filter down evaluation results.

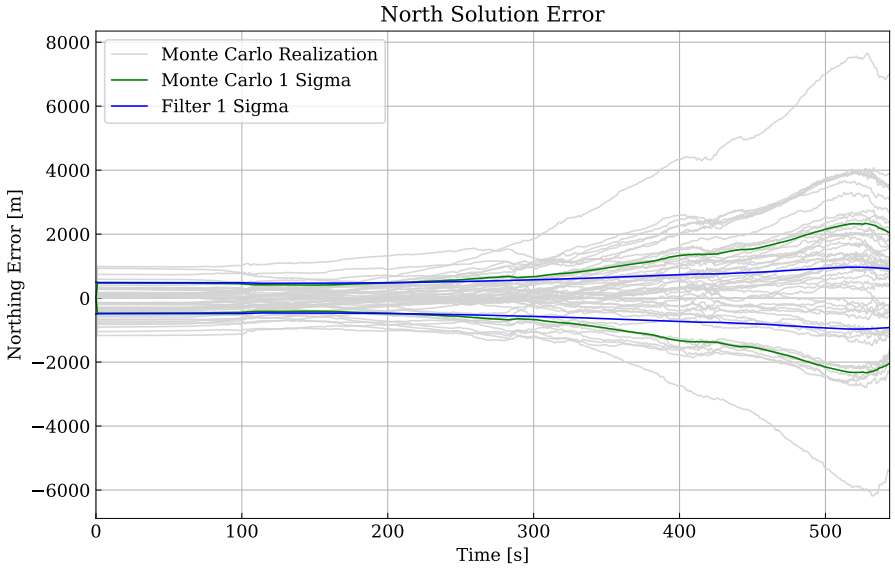

Figure 29: Tactical grade IMU filter tuning northing results. In these results we see that the estimated filter standard deviation (blue) resembles the Monte Carlo standard deviation (green). These results show that the filter is slightly optimistic for the tactical grade IMU.

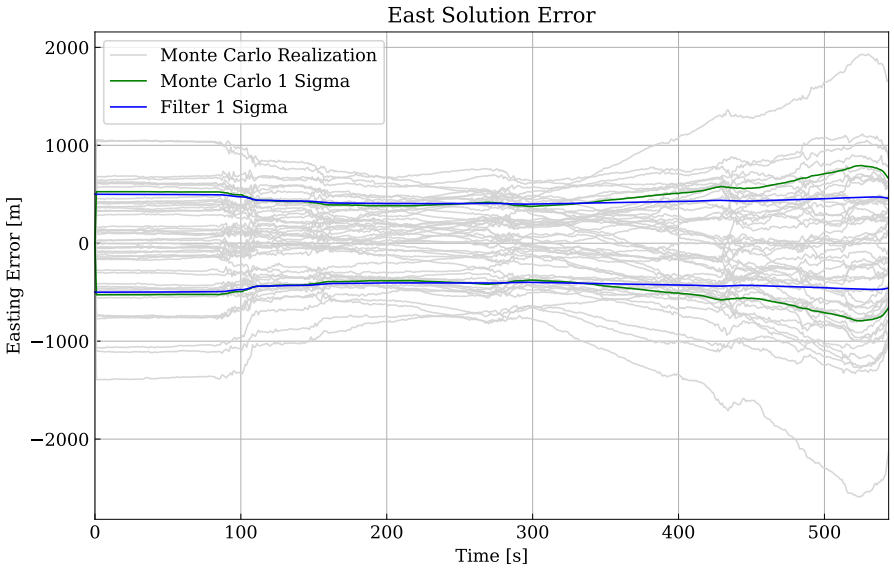

Figure 30: Tactical grade IMU filter easting evaluation results.

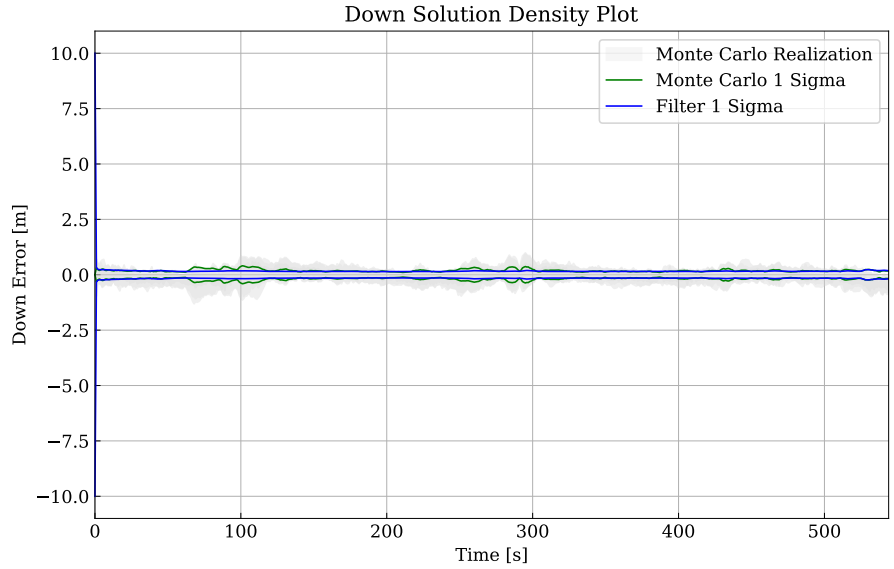

Figure 31: Tactical grade IMU filter down evaluation results.

are seen in figures 33 and 34.

Since both of these trajectories show that the filter is well tuned with stable performance, the Monte Carlo simulation was changed to provide a random starting

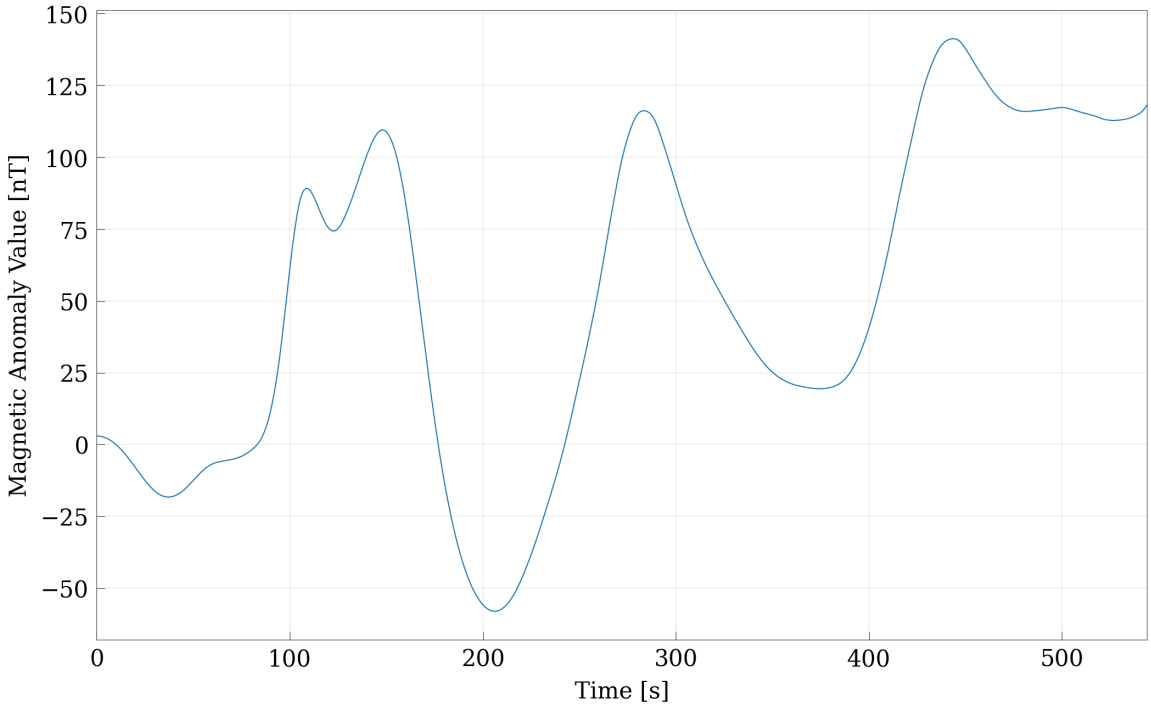

Figure 32: Noiseless scalar magnetometer readings for navigation results in figures 26 to 31. Note how the signal becomes less smooth over time, this is a result of higher frequency information coming available as the HGV descends in altitude.

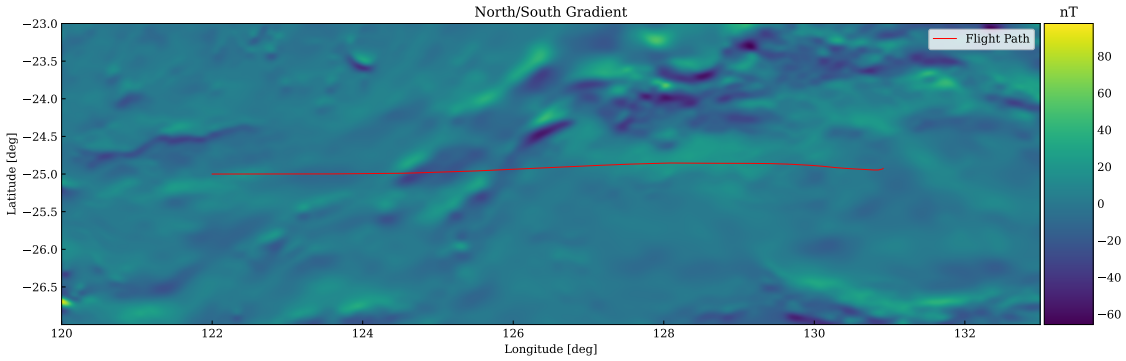

Figure 33: North/South Magnetic Field Gradient. Notice the smoothness of this gradient, especially along the flight path.

location. Magnetic anomalies vary by location, and a location's magnetic anomaly field can greatly effect the performance of a MagNav system. Thus, the trajectory location (and effectively the magnetic anomaly signal) must be varied to provide an average performance result. For all simulations with randomly varying starting lo-

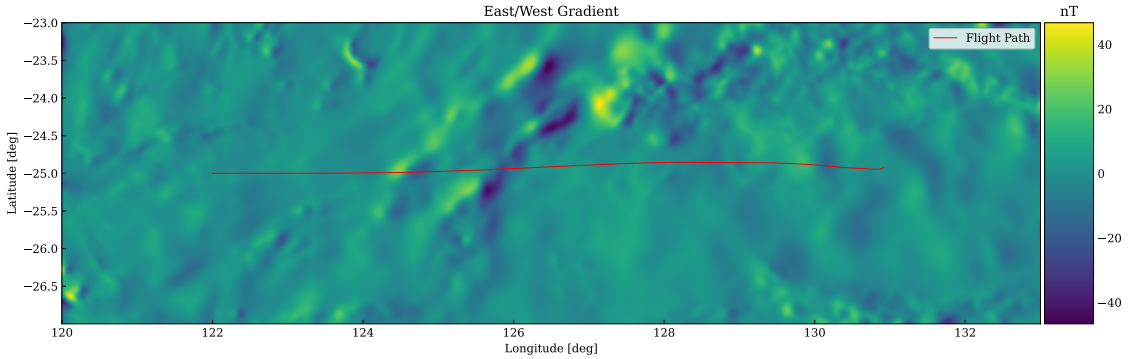

Figure 34: East/West Magnetic Field Gradient. Notice how the field gradient contains much more information, which results in a better navigation result.

cations, the trajectories are bound within the following box: $[-29°, -19°]$ N, $[126°, 143°]$ E. This constrains the trajectories to the more central areas of the Australia Magnetic Anomaly Map, while still providing a large sampling area of potential magnetic anomaly signals. The potential trajectories must stay away from the edge of the map to avoid edge effects. The testing area magnetic anomaly map, and some sample trajectories are overlaid on a map of Australia in Figure 35. Simulation time is unfortunately increased significantly as a result of using random trajectory origins. This occurs as measurements, and their respective noises must be recalculated with each Monte Carlo run. This greatly increases the computational complexity of the simulations, however it is a requirement for robustness.

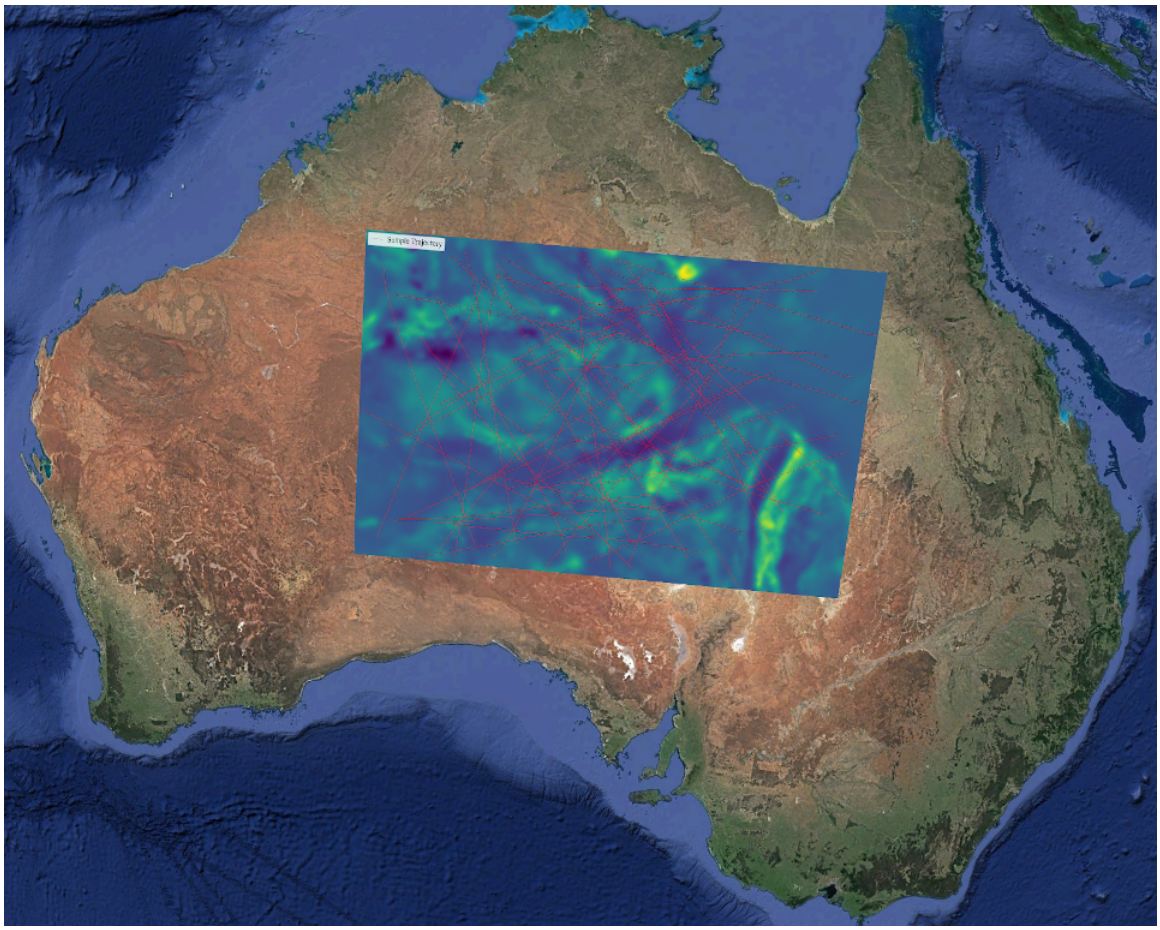

Figure 35: Australia Magnetic Anomaly Map overlaid on Australia. Potential flight paths can be seen in red.

To simulate a range of potential trajectories, 4 additional trajectories were introduced. These trajectories range in length from 532 to 652 seconds. As a result, they are not plotted on the same plot. The Monte Carlo plots presented in this chapter are only for the first trajectory and for 50 Monte Carlo runs, and additional plots for the remaining 4 navigation grade trajectories and 200 Monte Carlo runs can be seen in Appendix A. The tables contain averages across all five simulated trajectories. These averages were computed at the last time step. The results from this diversified Monte Carlo simulation for the navigation grade IMU are in figures 36-37. These

figures showcase the ability of MagNav to constrain IMU drift. To properly compare the performance of MagNav to an IMU only system, the MagNav portion of the filter was disabled, and the simulations were re-ran. These results can be seen in figures 38-39.

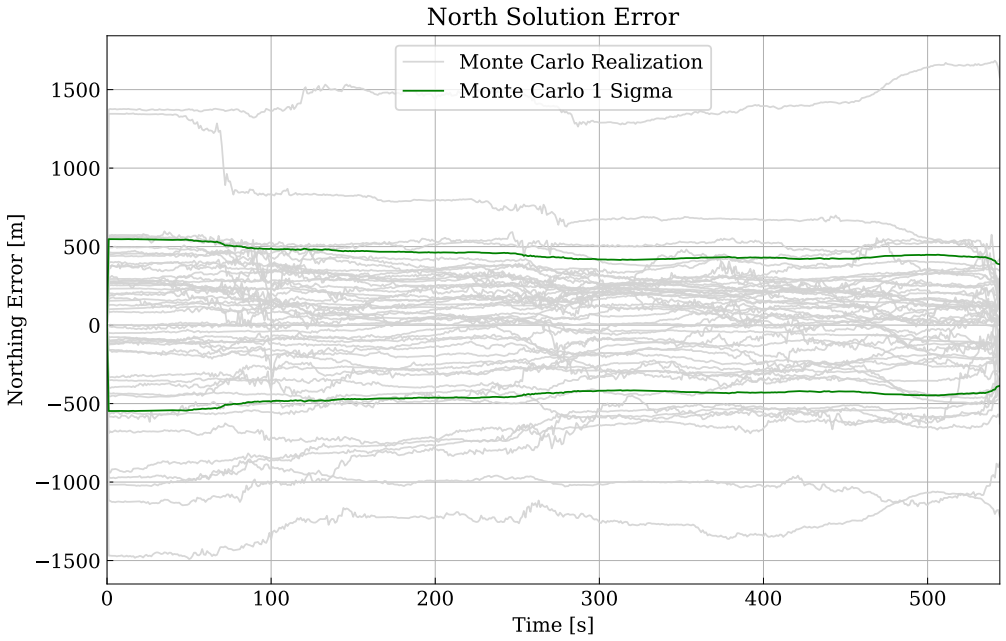

Figure 36: Hypersonic MagNav Monte Carlo Simulation northing error results using a navigation grade IMU. These results are position errors. Australia Magnetic Anomaly Map as map source. Notice how the covariance bounds decrease over time.

In total all five trajectories produced the following average performance statistics with the navigation grade IMU as shown in Table 3.

These results show a DRMS error of 437.3 m, which demonstrates the viability of MagNav on a HGV as they significantly outperform the unaided IMU which achieves 827.2 m DRMS error. These trajectories started with an initial uncertainty of 500 m in the northing and easting directions, so MagNav was able to constrain this uncertainty slightly, but most importantly prevent further drift. This is in contrast to the IMU only simulations which continued to drift and diverge further over time.

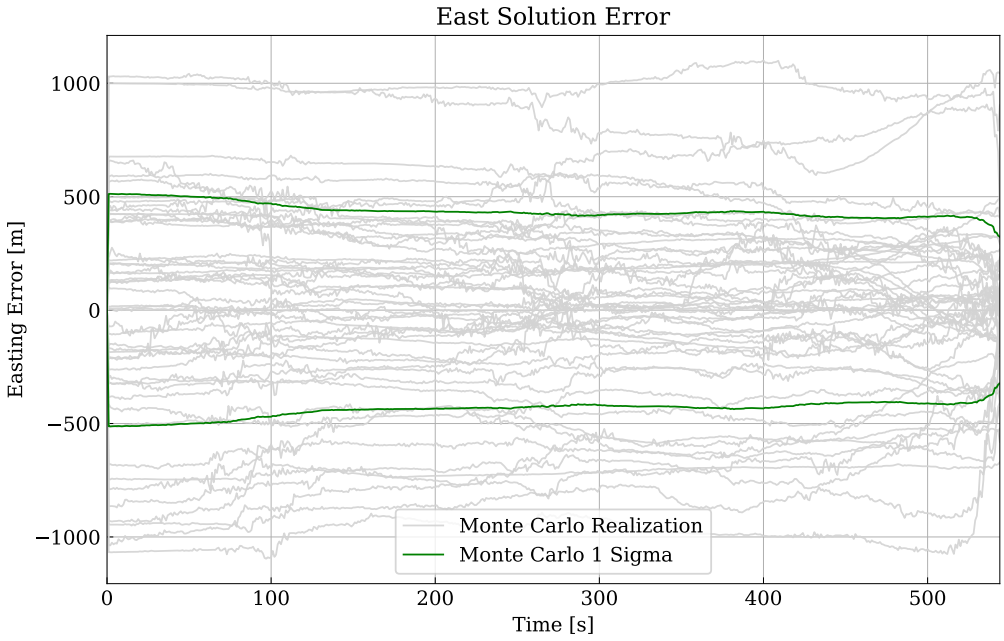

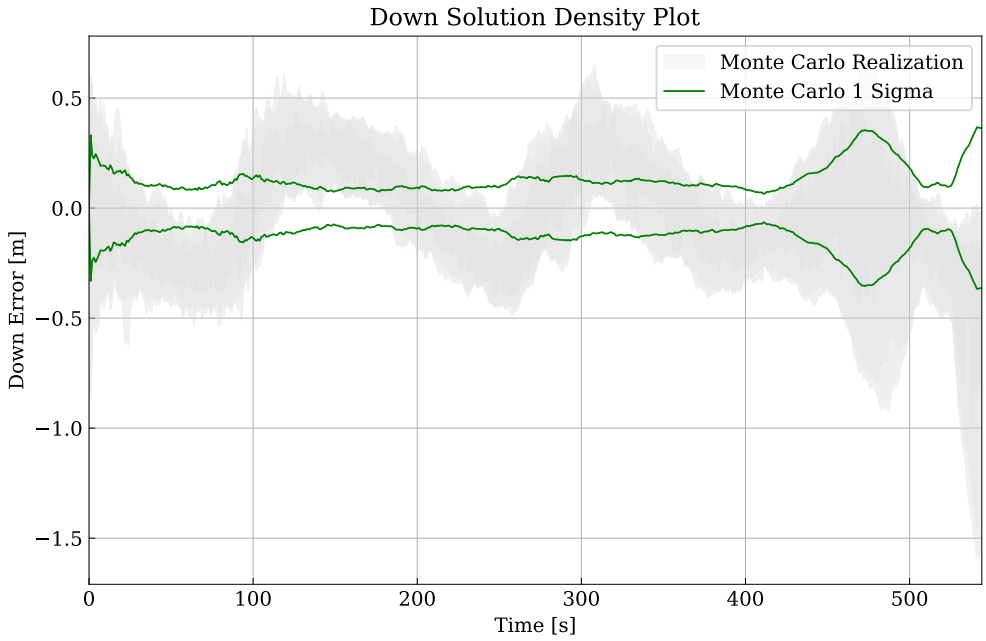

Figure 37: High quality map MagNav Monte Carlo Simulation navigation easting and down results using a navigation grade IMU

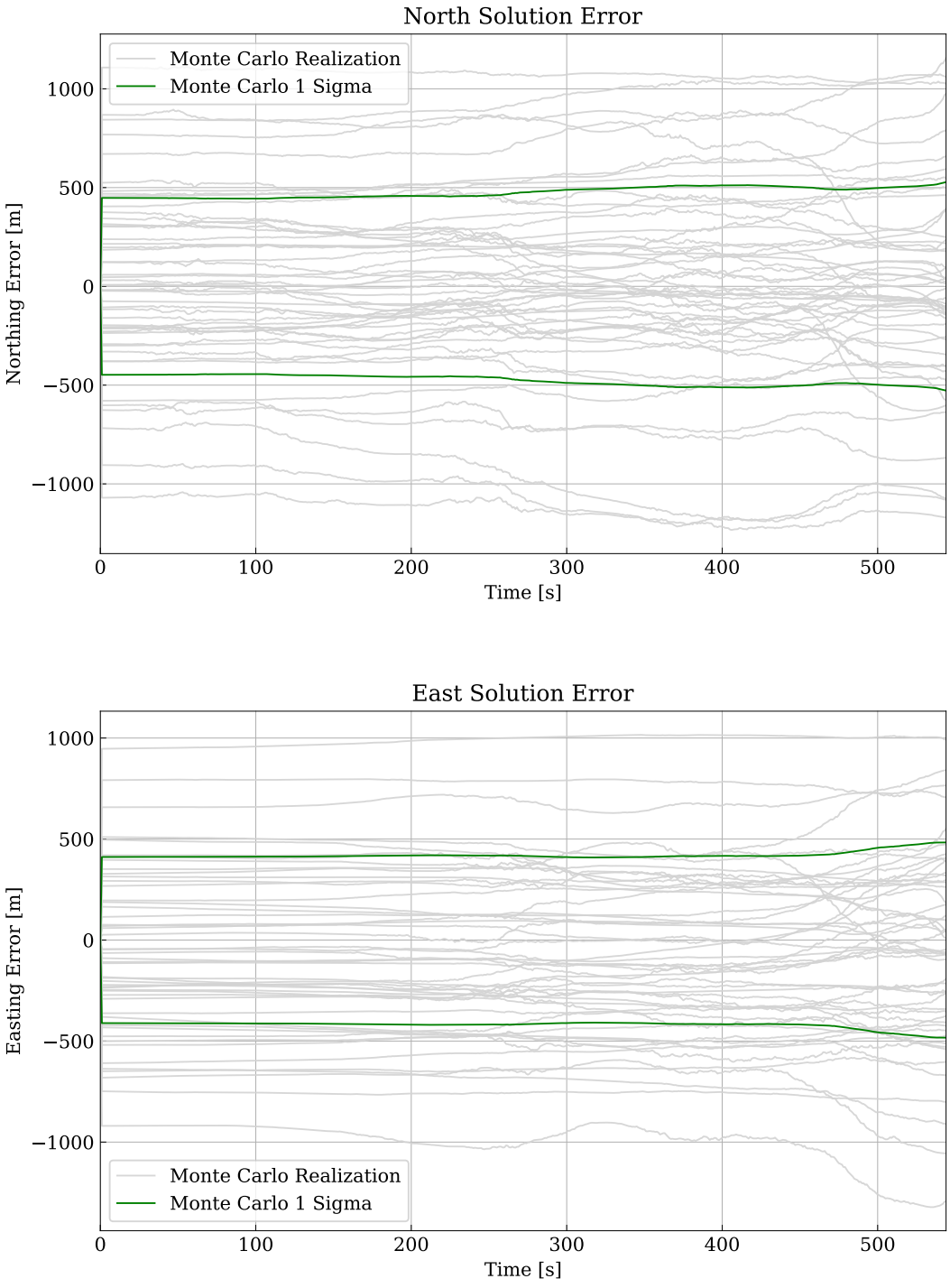

Figure 38: Navigation grade IMU only Monte Carlo Simulation results. Notice how the covariance bounds increase over time.

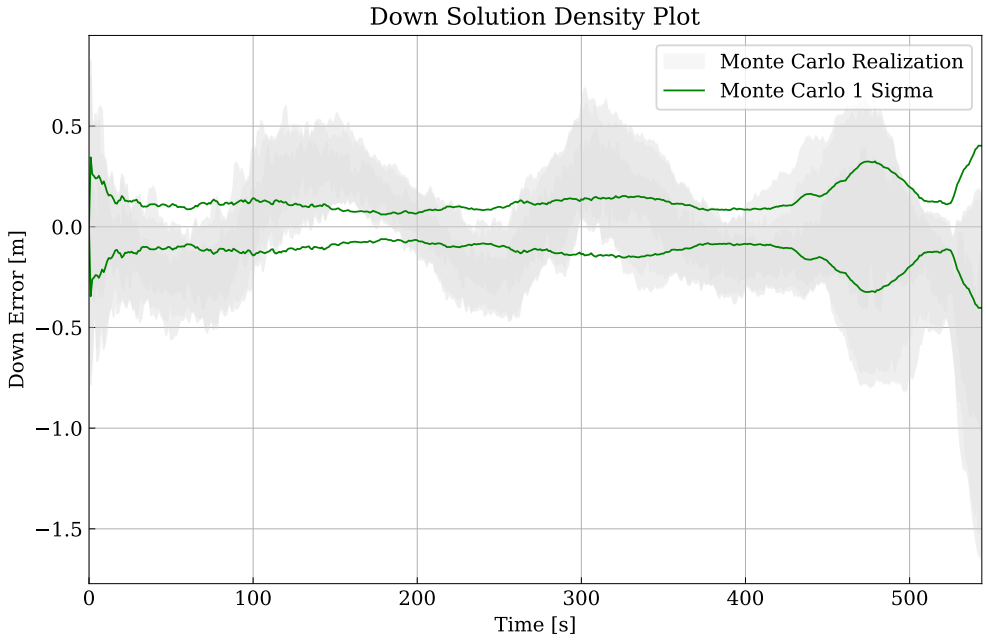

Figure 39: Unaided navigation grade IMU Monte Carlo Simulation down results.

Table 3: Average navigation grade IMU MagNav Monte Carlo Simulation results.

Measurement	**MagNav**	**IMU Only**
MAE North Error (m)	231.93	490.3
STD North Error (m)	322.0	613.3
MAE East Error (m)	206.31	443.1
STD East Error (m)	288.3	544.0
MAE Down Error (m)	0.30	0.32
STD Down Error (m)	0.23	0.26
DRMS Error (m)	437.3	827.2

Next the simulations were repeated with the HG1700 tactical grade IMU. Like with the navigation grade IMU, the simulations had a random origin and 500 m of initial northing and easting uncertainty. Each trajectory of the five trajectories were run 50 times in the Monte Carlo simulation. The results from the first trajectory can be seen in figures 40 and 41. Results from the four additional trajectories can be seen in Appendix B. For comparison, the unaided IMU results are shown in figures 42-44.

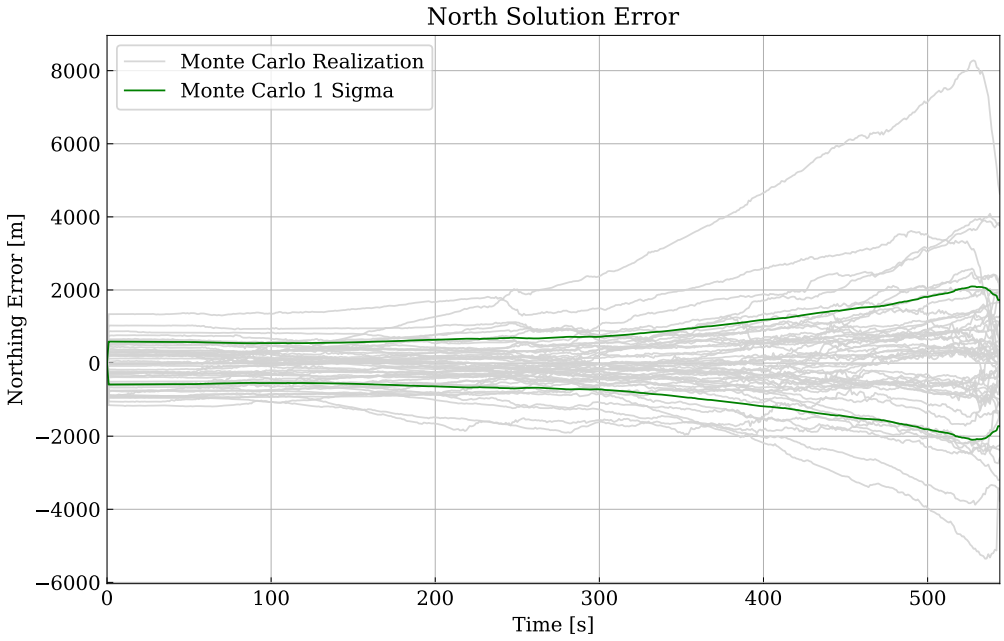

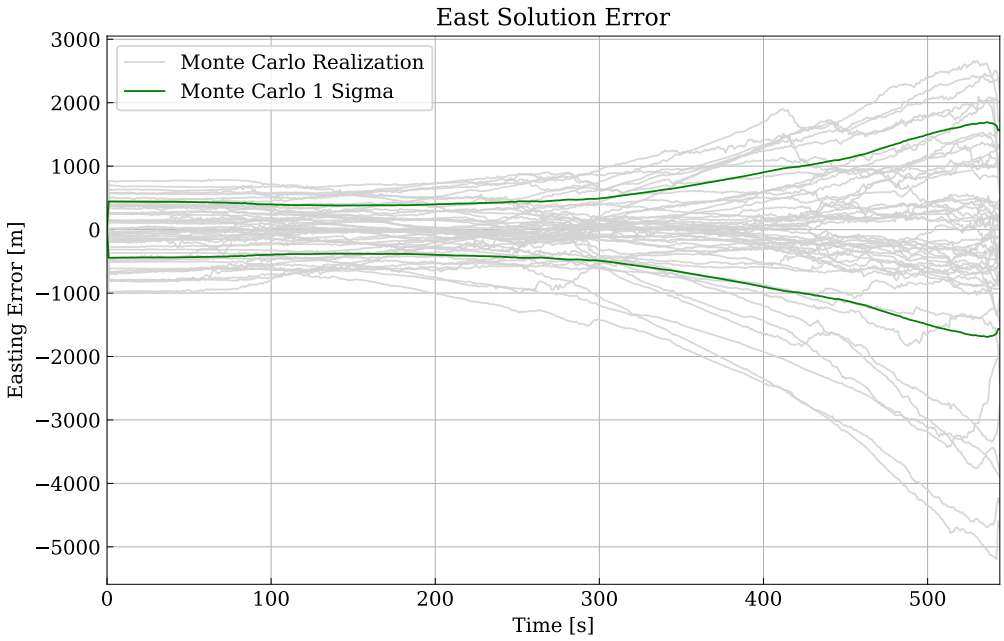

Figure 40: Tactical grade IMU MagNav Monte Carlo Simulation results. Notice how the covariance bounds increase over time, then constrain as more information becomes available.

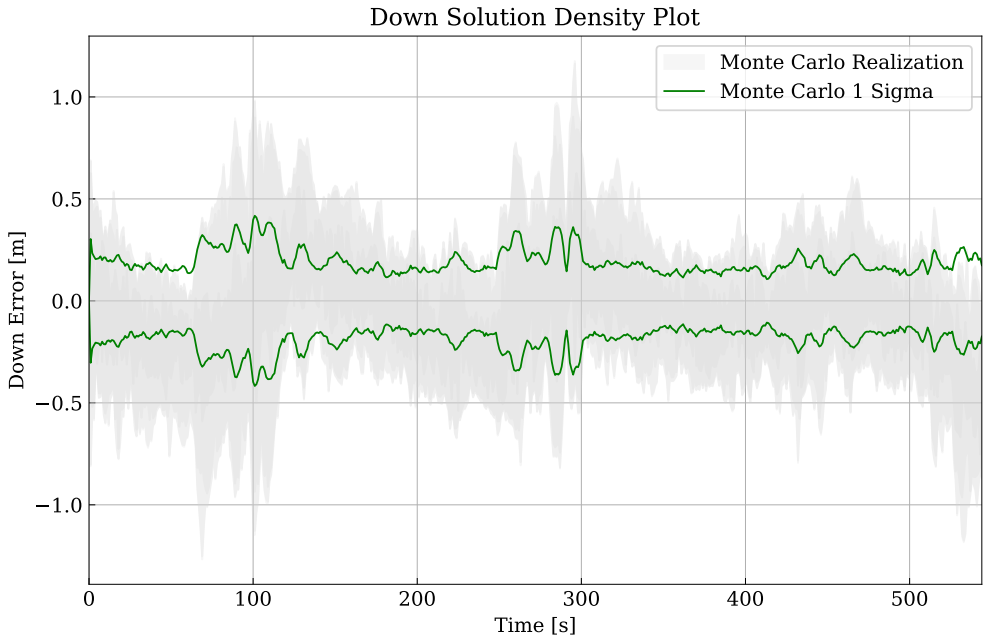

Figure 41: Tactical grade IMU Monte Carlo Simulation down results.

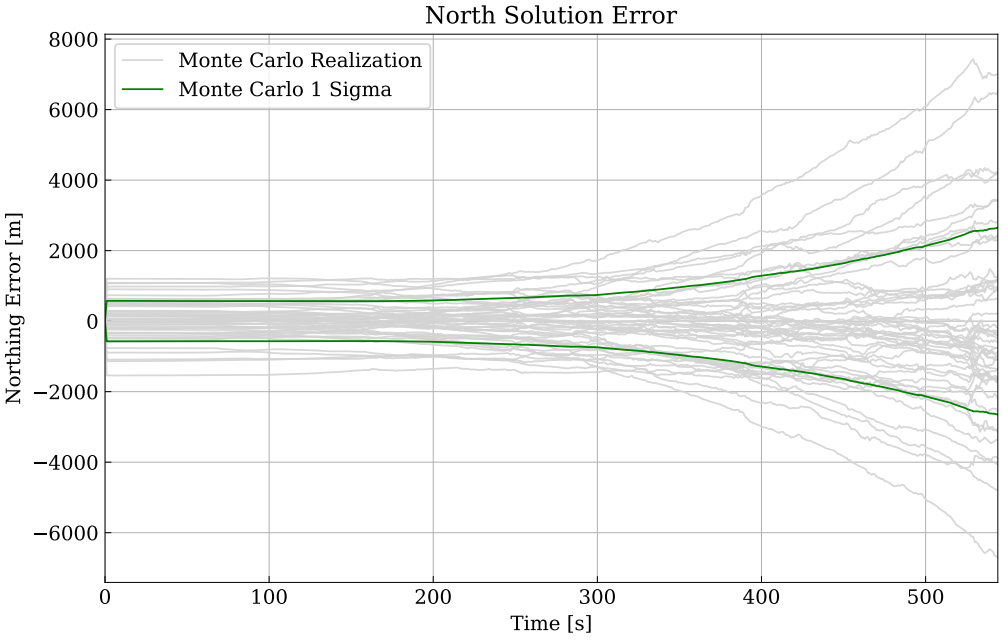

Figure 42: Unaided tactical grade IMU only Monte Carlo Simulation results. Notice how the covariance bounds increase over time.

In total all five trajectories produced the average performance statistics with the tactical grade IMU as shown in Table 4.

Table 4: Average tactical grade IMU MagNav Monte Carlo Simulation results.

Measurement	**MagNav**	**IMU Only**
MAE North Error (m)	1 628.8	2 704.8
STD North Error (m)	2 833.7	3 516.5
MAE East Error (m)	1 223.5	1 872.7
STD East Error (m)	1 865.6	2596.5
MAE Down Error (m)	0.26	0.27
STD Down Error (m)	0.19	0.19
DRMS Error (m)	3 455.5	4 427.5

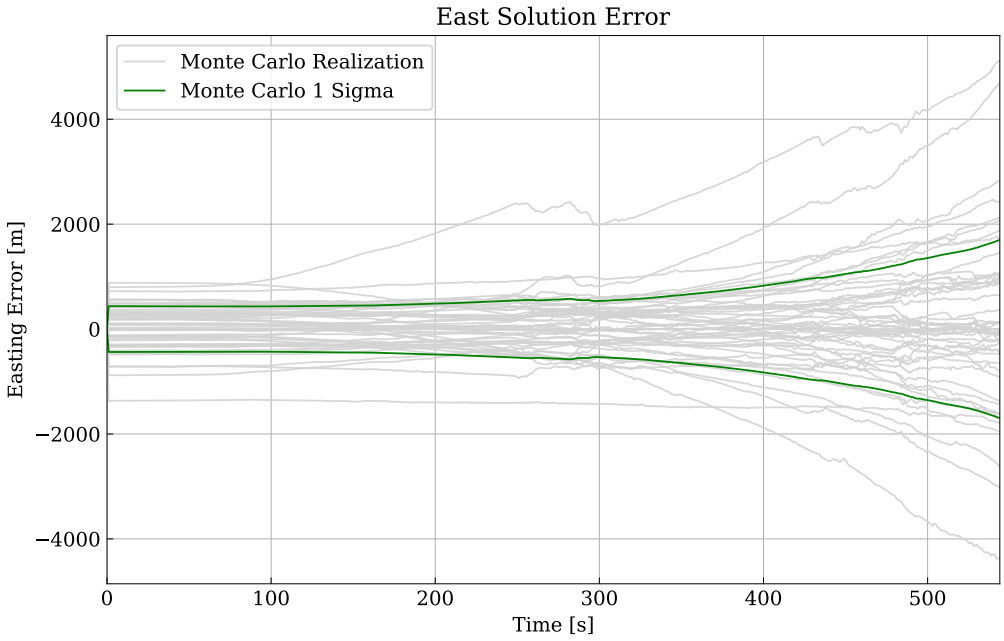

Figure 43: Unaided tactical grade IMU only Monte Carlo Simulation easting results.

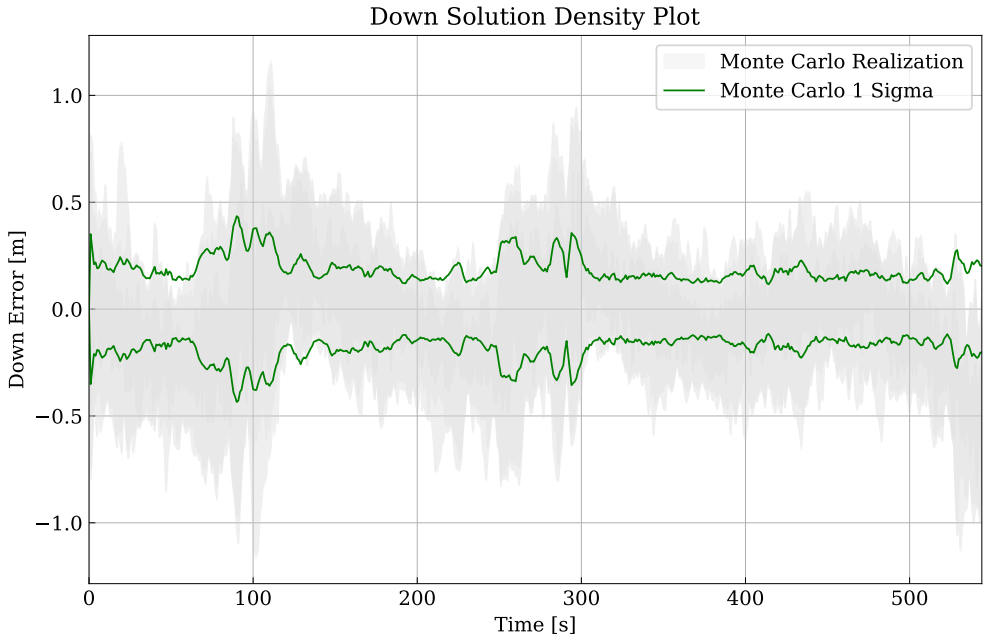

Figure 44: Unaided tactical grade IMU only Monte Carlo Simulation down results.

These results show a significant decrease in filter performance as expected. However, the MagNav system showed nearly 1 km improvement in DRMS. As expected there was little difference in altitude performance due to the aiding provided by the altimeter. Both the navigation and tactical grade IMUs showed a slight bias in performance towards the easting direction. This can be explained as the trajectory generation system has a slight bias towards allowing the trajectories to be east/west trajectories. The bias was an unintended result of making the box rectangular over square. With the rectangular box, the trajectories are slightly more likely to be an east/west trajectory as those fit in the box better. When a trajectory is heavily dominate in one direction, it is able to better constrain the drift better in that direction. However, since the differences are not significant this difference could be resolved by making the potential location box square. This would however reduce the potential area of simulation. Overall, simulations using the Australia Magnetic Anomaly Map

show that MagNav outperforms unaided tactical and navigation grade IMUs. As a result we can say that MagNav is viable for a hypersonic aircraft with a high quality map.

4.4 EMM Based Simulations

To establish realistic expectations for world-wide performance with present maps, simulations were conducted using the EMM. The EMM has two advantages over the Australia map. First the EMM offers world-wide coverage. Second, the EMM is much less RAM intensive and does not require upwards continuation, since it takes advantage of spherical harmonics. However, this is at the expense of increased CPU usage resulting in an approximately a 25% increase in simulation time. The third key advantage to the EMM can also be attributed to spherical harmonics. The EMM does not have to be upwards continued and instead can be queried for any altitude at any latitude and longitude several hundred times per second on an average computer. This greatly simplifies the map processing required for simulation. The downside to utilizing the EMM is that it is both lower resolution and lower accuracy compared to the Australia Magnetic Anomaly Map.

The IMU and altimeter measurements were generated in the same manner outlined in the previous section. All trajectories remained in the same bounds. Therefore, the results in this section can be directly compared to the results in the previous section. To simulate magnetometer sensor readings, the Australia Magnetic Anomaly Map was used. This was chosen as the EMM is not a perfect model, and using the Australia Magnetic Anomaly Map for measurements allows for the inclusion of errors introduced by the difference between reality and the model. As a result of this mismatch, the initial position error had to be increased to show the effect of MagNav. This simulation would be analogous to running the filter with real magnetometer data

while using the EMM as the map source. One key difference between the results from the simulations on the EMM and those seen in Section 4.3 is the exclusion of tactical grade IMU results. This decision was made after a tactical grade IMU was used to simulate one trajectory. The results of this tactical grade IMU simulation can be seen in figures 45 -46 below.

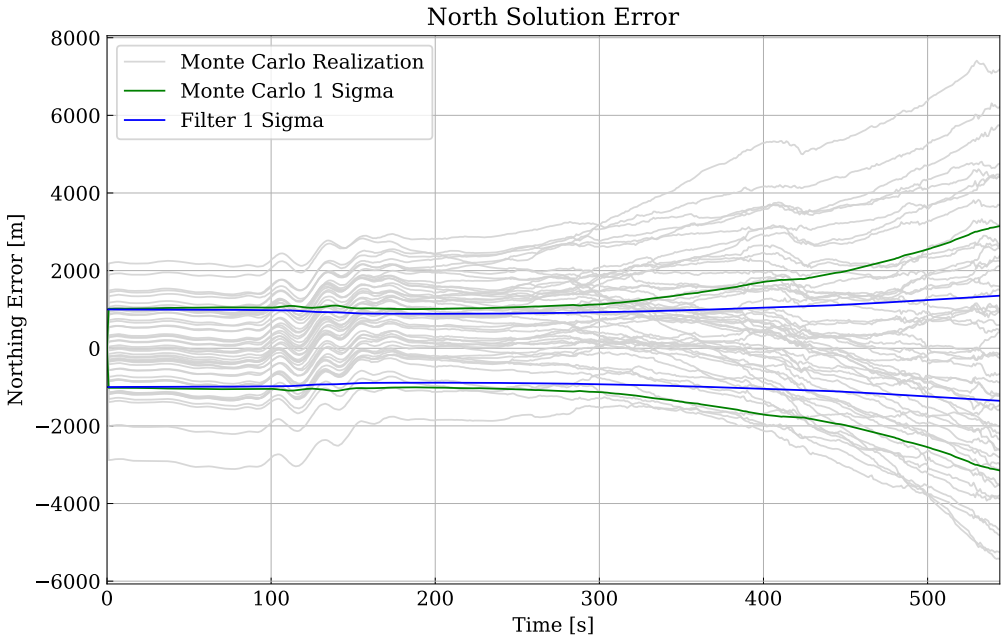

Figure 45: Hypersonic MagNav Monte Carlo Simulation nothing results using a tactical grade IMU. These results are position errors. EMM as map source. Note how MagNav does not constrain solution or filter estimated covariance.

As seen in Figure 45 and Figure 46, the tactical grade IMU does not provide any apparent constraint on IMU drift. Increasing the initial position uncertainty resulted in filter divergence. From these results, navigation on the EMM using a tactical grade IMU is not possible for hypersonic aircraft. To test the navigation grade filter's stability, the filter was initially tested over the same location, as was the case with prior simulations. This location was the same as the previous section, starting at $-25°$ N, $122.0°$ E. The results from this simulation can be seen in figures 47-48.

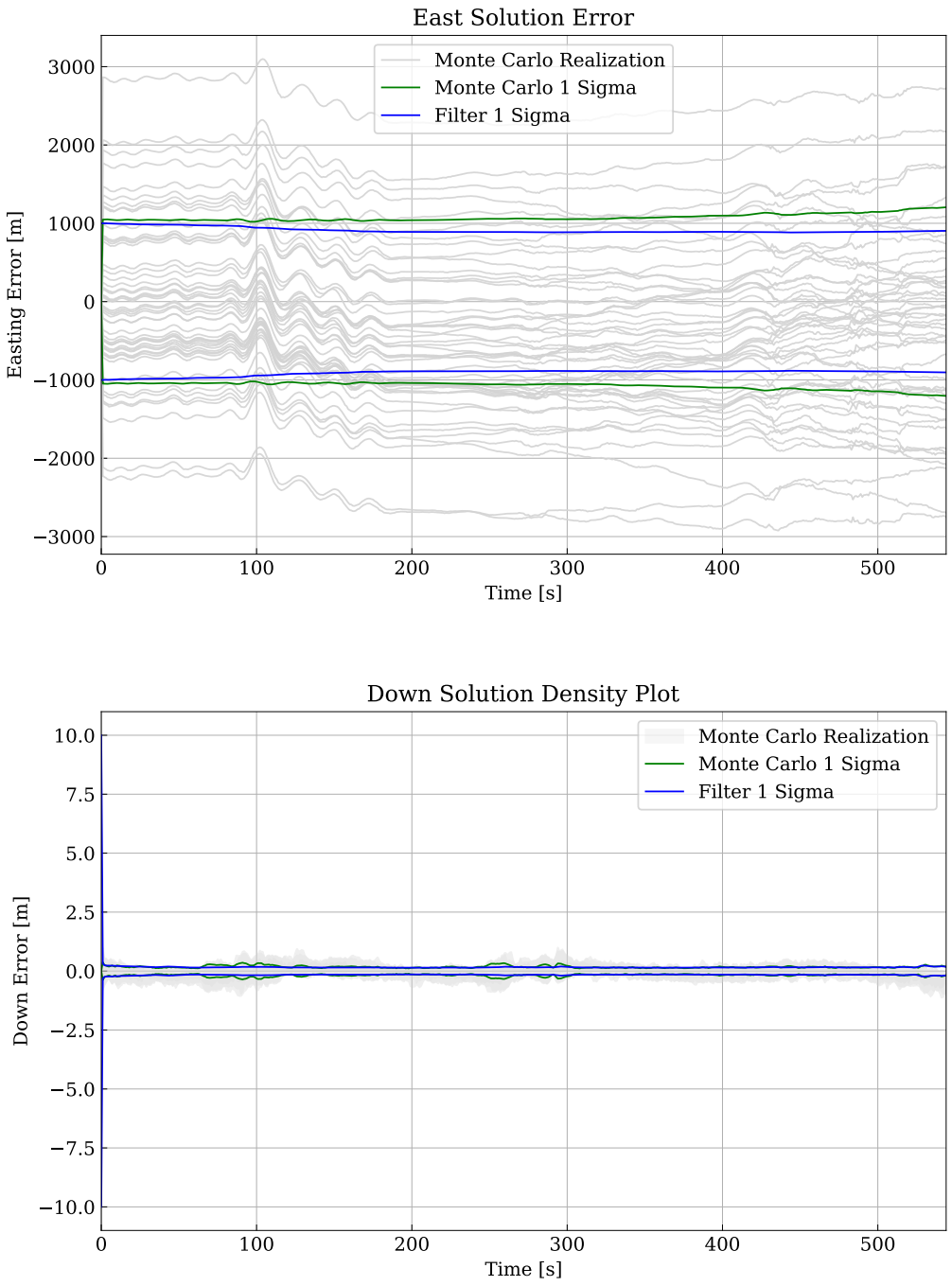

Figure 46: Hypersonic MagNav Monte Carlo Simulation easting and down results using a tactical grade IMU. These results are position errors. EMM as map source.

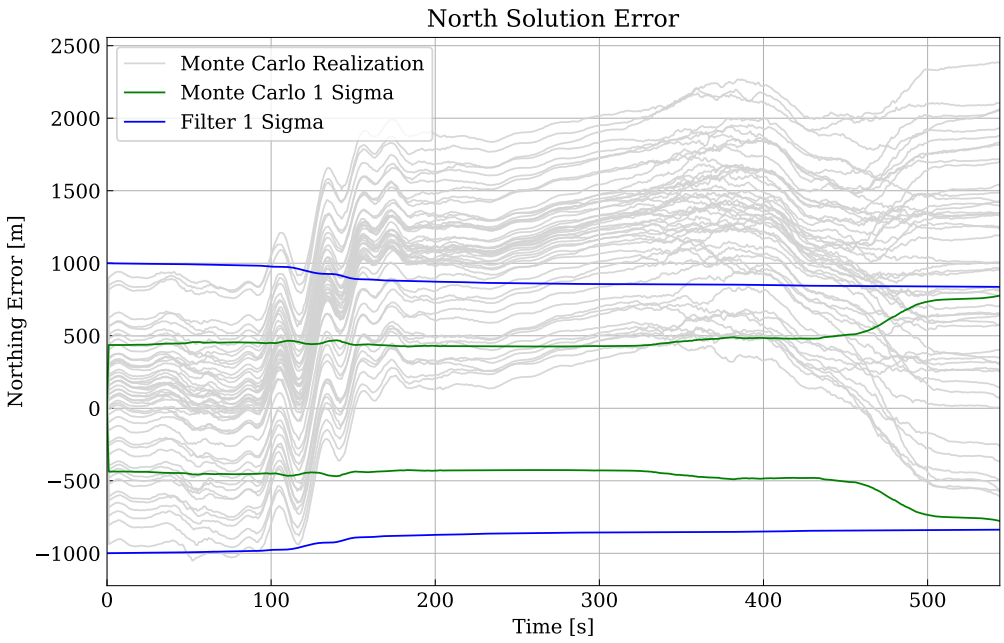

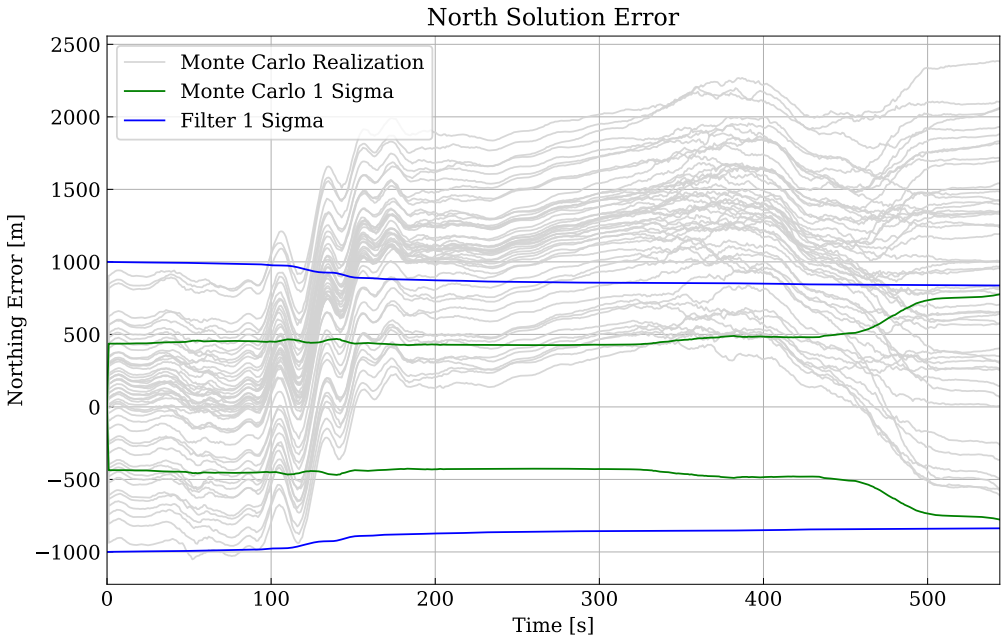

Figure 47: Hypersonic MagNav Monte Carlo Simulation northing and easting results using a navigation grade IMU. These results are position errors. EMM as map source. Note how this MagNav slightly constrains the solution, however performance is poor, and filter does not constrain to covariance bounds well.

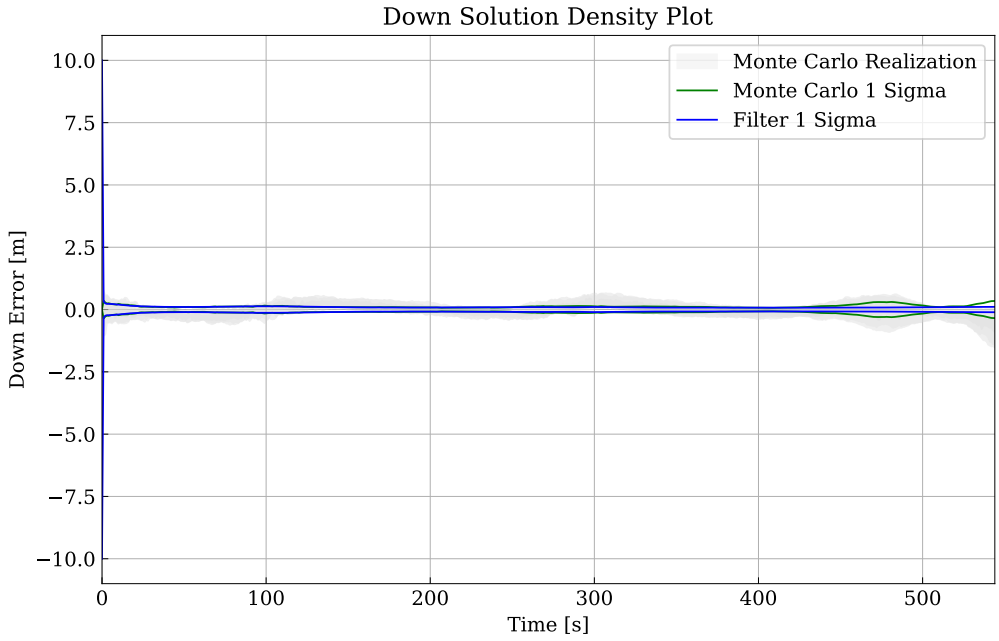

Figure 48: EMM map MagNav Monte Carlo Simulation navigation down results using a navigation grade IMU.

This filter solution with the EMM shows reduced performance. The error increase should be attributed to the map and sensor mismatch. Since the introduction of this error and the change in maps are the only simulation factors that changed between these results and those in Section 4.3, this is not an unreasonable assumption. To provide a thorough analysis of the navigation performance while using the EMM, the simulation was run using all five trajectories with fifty Monte Carlo simulations per trajectory starting from a random location. The results for the first trajectory are seen below in figures 49-50. Additional results are available in Appendix C. Since the initial conditions had changed for this set of simulations, the IMU only solution had to be resimulated to follow the same 1000 m initial position uncertainty of the MagNav system. The navigation grade unaided IMU Monte Carlo Simulation can be seen in figures 51-52.

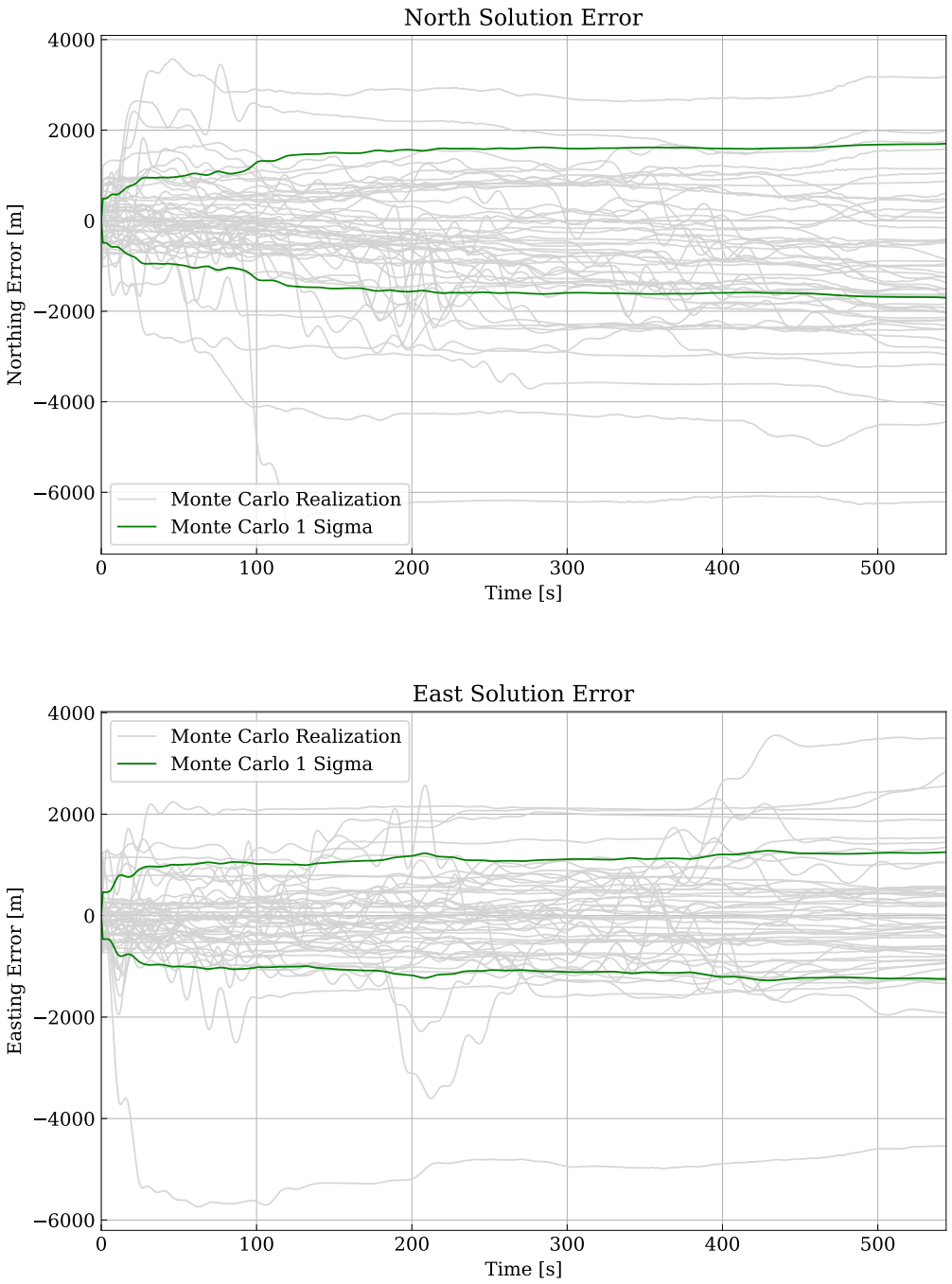

Figure 49: Hypersonic MagNav Monte Carlo Simulation northing and easting results using a navigation grade IMU. These results are position errors. EMM as map source. Notice how the solution does not meaningfully converge.

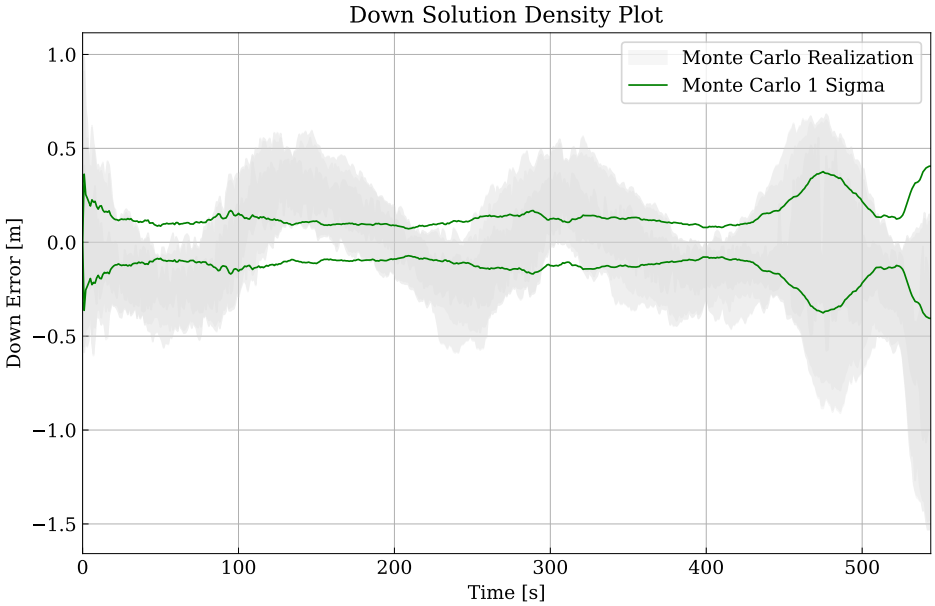

Figure 50: EMM based MagNav Monte Carlo Simulation navigation down results using a navigation grade IMU.

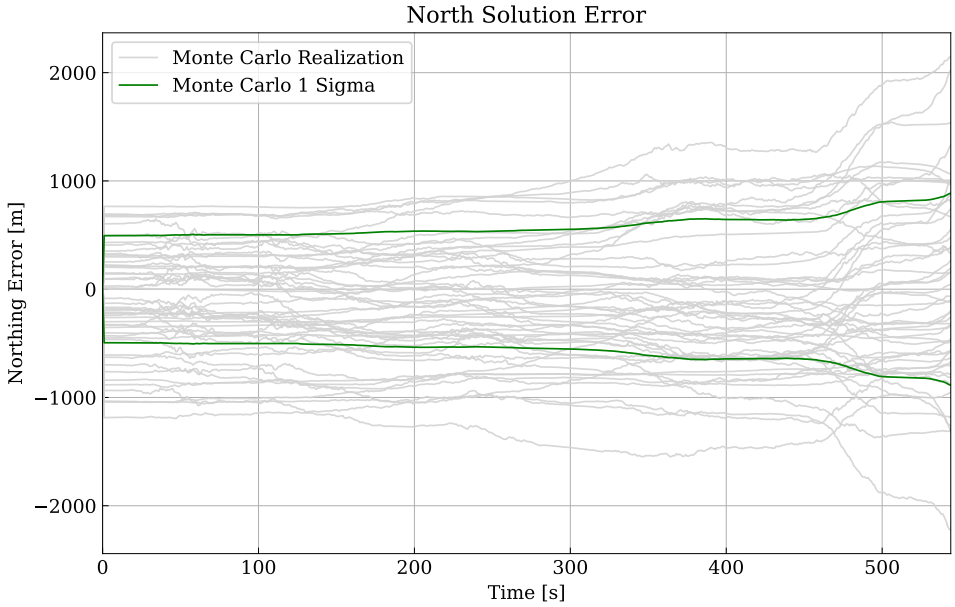

Figure 51: Navigation grade IMU only Monte Carlo Simulation northing results. These results differ from figures 38-39 as they were run with the initial conditions used for the EMM MagNav simulations.

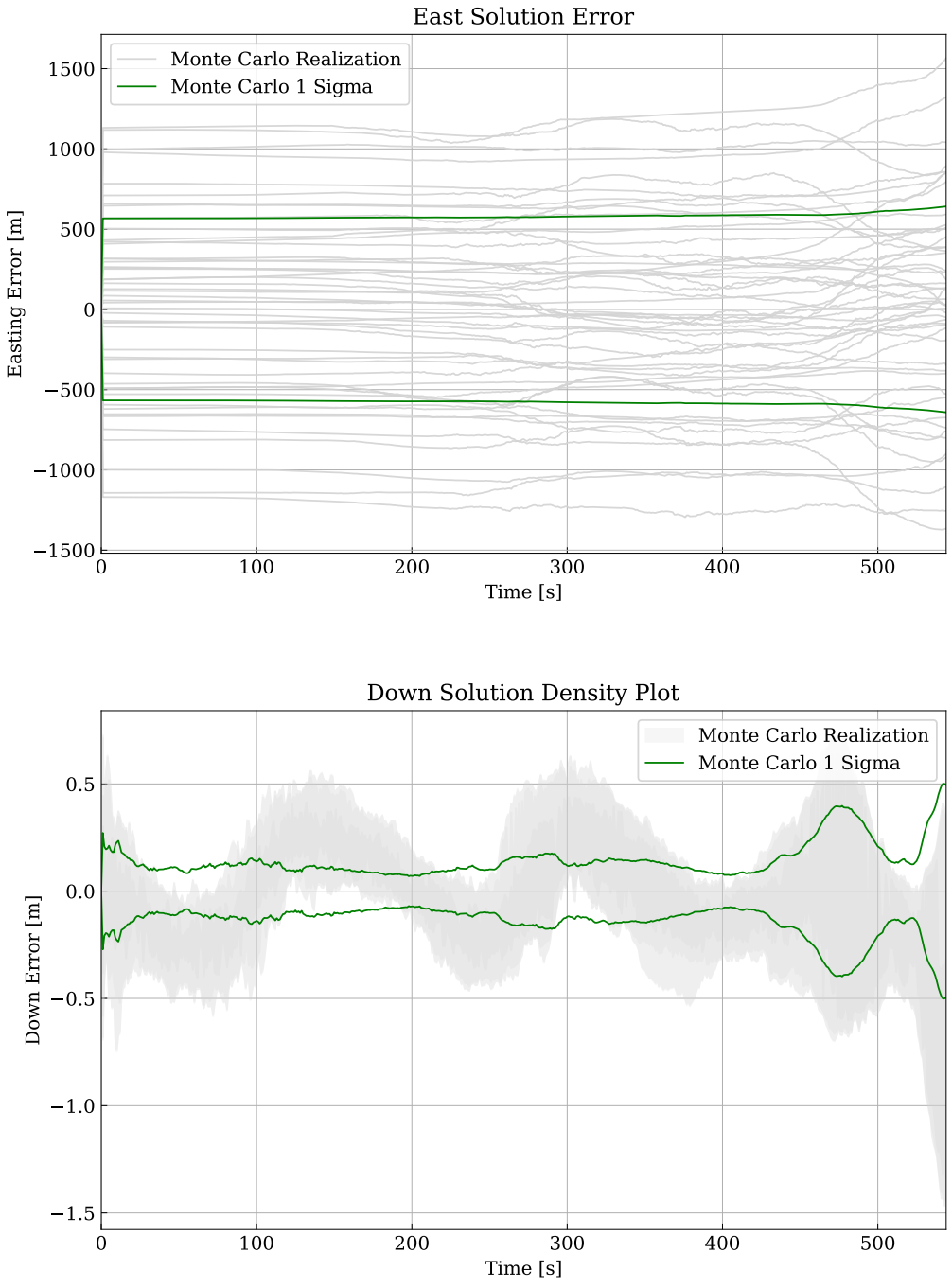

Figure 52: Unaided navigation grade IMU Monte Carlo Simulation (EMM initial conditions) easting and downing results.

The result from Monte Carlo Simulations of all five trajectories were averaged to create the following table:

Table 5: Average navigation grade IMU MagNav Monte Carlo Simulation results using EMM.

Measurement	**MagNav**	**IMU Only**
MAE North Error (m)	1 623.47	664.30
STD North Error (m)	1 877.6	872.3
MAE East Error (m)	1 147.2	463.5
STD East Error (m)	1 709.9	585.87
MAE Down Error (m)	0.32	0.31
STD Down Error (m)	0.26	0.27
DRMS Error (m)	2 717.8	1 062.4

These results are at best inconclusive, but point towards the conclusion that using the EMM as the map for MagNav is not viable. It is possible that for longer time periods, or higher initial position uncertainty that this is a convergent solution. However, higher initial position uncertainty will require the use of a Roa-Blackwellized particle filter, something the MagNav infrastructure around this project does not yet support. If these high initial position uncertainties were both usable, and convergent then they might not be realistic. In this project, initial position uncertainties were utilized to simulate both slight noise at the initial time, and longer flights. Longer flights than those simulated were explored in Lysak's research [8]. However, both the length of flight required to reach the desired uncertainty, and potential noise at the beginning would be unrealistic. The end result is that MagNav is not viable using the EMM for hypersonic aircraft, due entirely to the sensor mismatch problem.

4.5 Vector MagNav Results

The key advantage to vector based MagNav is that the amount of information available to the navigation filter is increased. This information increase is highlighted

in the vector magnetometer readings, which provide the filter with more information, which in turn provides a better navigation solution. A sample of these readings are available in Figure 53.

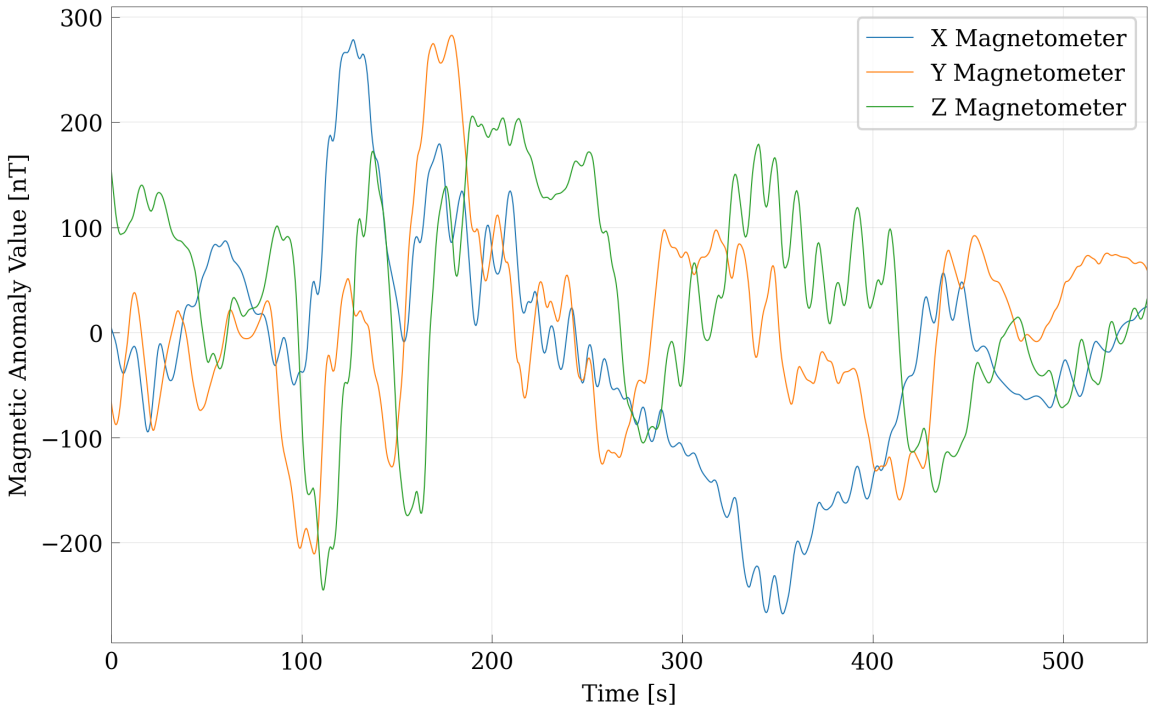

Figure 53: Vector magnetometer readings. These readings show the increased information available to the navigation filter. Note there appears to be some correlation between the axes.

With these readings it is important to remember that the navigation improvement is not linear with respect to unique magnetometer readings as discussed in Section 2.1.4. Thus, it should not be expected to see a 3 times improvement over a scalar magnetometer system. The reason that this is the case is the correlation between the axes of the vector measurements. This can be best exemplified when viewing the maps of each respective vector axis as seen in figures 54 - 56.

From these maps it becomes clear there is spatial correlation between the axes of vector magnetometer. Regardless of the potential decrease in performance by these correlations, it should be expected that vector MagNav should out-perform scalar

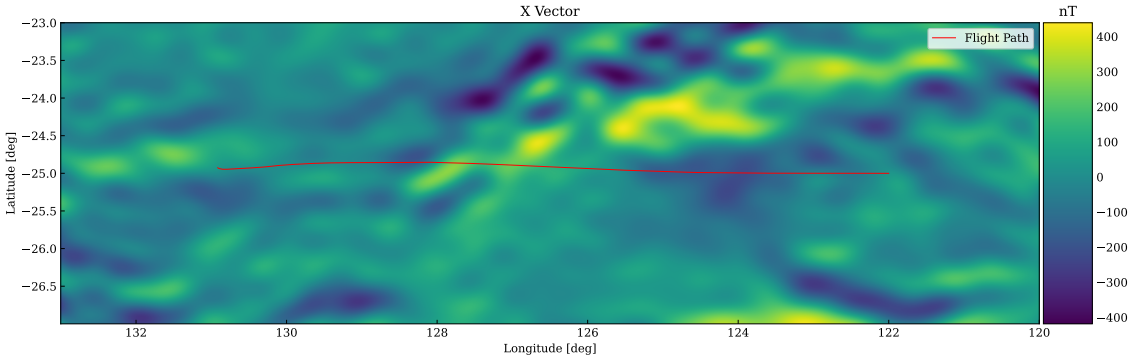

Figure 54: Vector EMM x-axis.

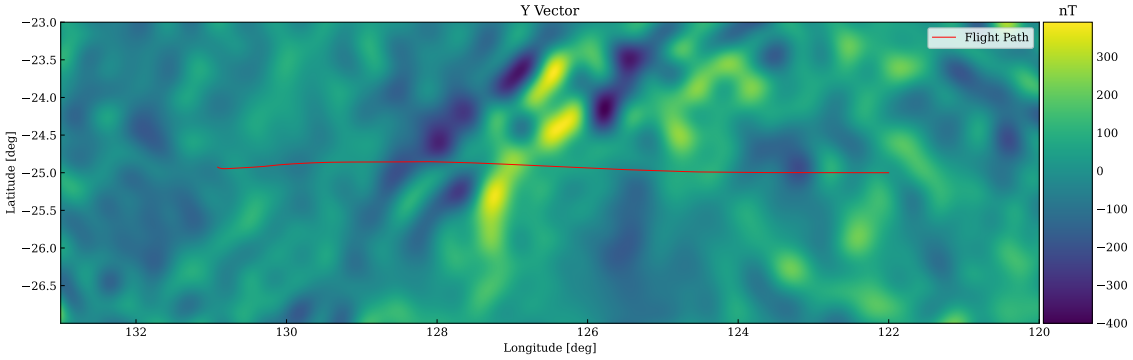

Figure 55: Vector EMM y-axis

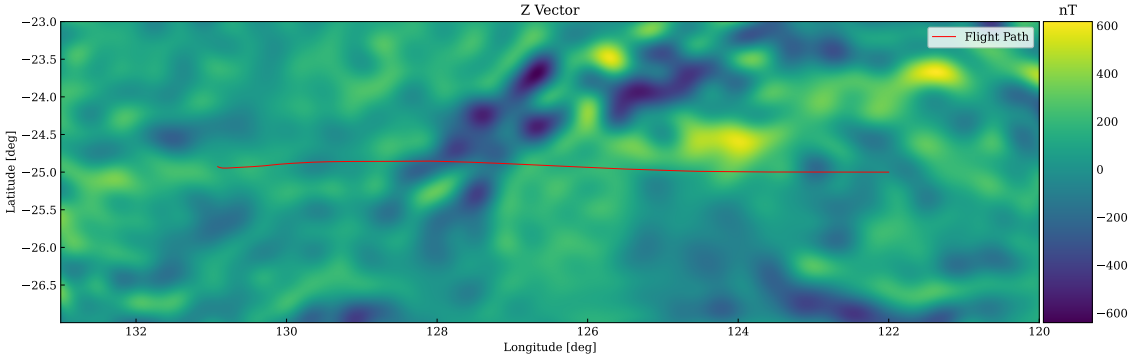

Figure 56: Vector EMM z-axis

MagNav by a significant margin. For the case of vector MagNav, the EMM is the only available map. Vector MagNav is simulated in the same process as the previous two scalar MagNav simulations. However, the primary expected difference is that the provided measurements must vector measurements. These measurements can be

provided by a simple change in the EMM query. The first set of fifty Monte Carlo runs to test filter stability were run starting at $-25°$ N, 122.0° E with 500 m of initial position uncertainty. These results are seen in figures 57 - 58.

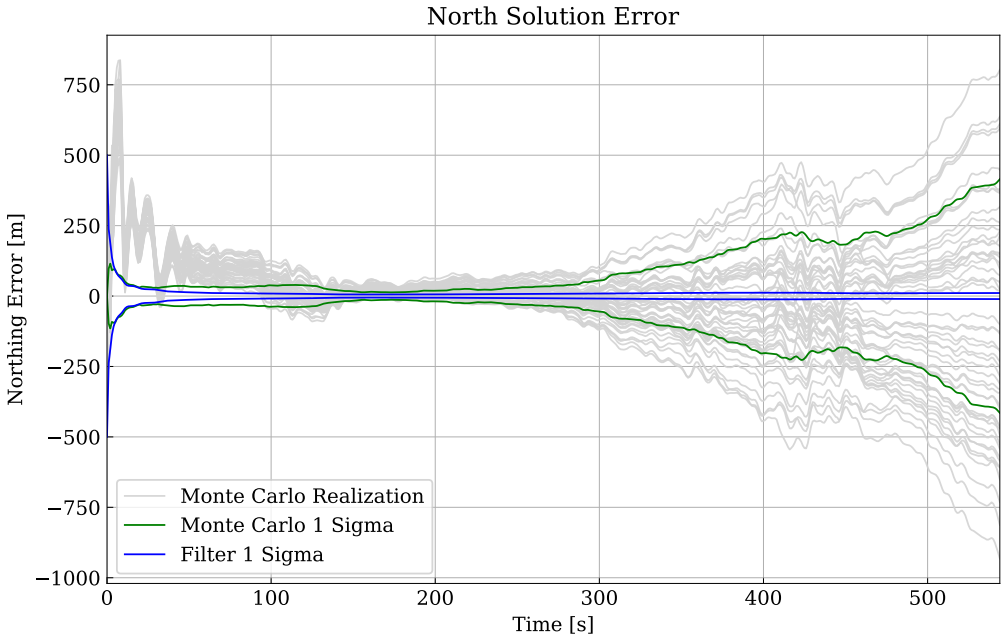

Figure 57: Vector MagNav Monte Carlo Simulation with static initial northing results.

These results show that the filter could be functioning incorrectly, however simulations across all five trajectories were conducted. The performance of the first trajectory is shown in figure 59 - 60. The performance of the other trajectories can be seen in Appendix D.

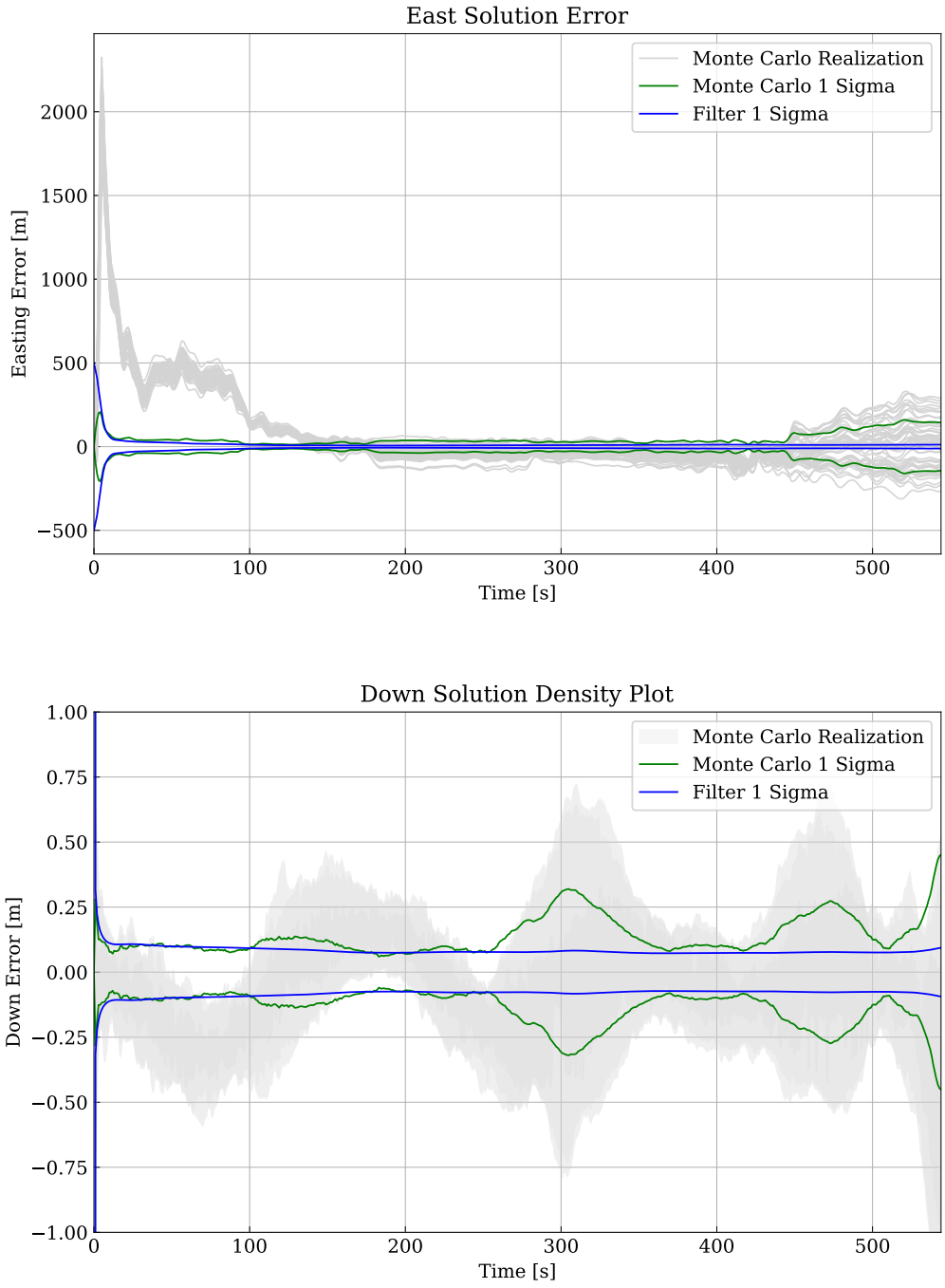

Figure 58: Vector MagNav filter tuning test easting and down results.

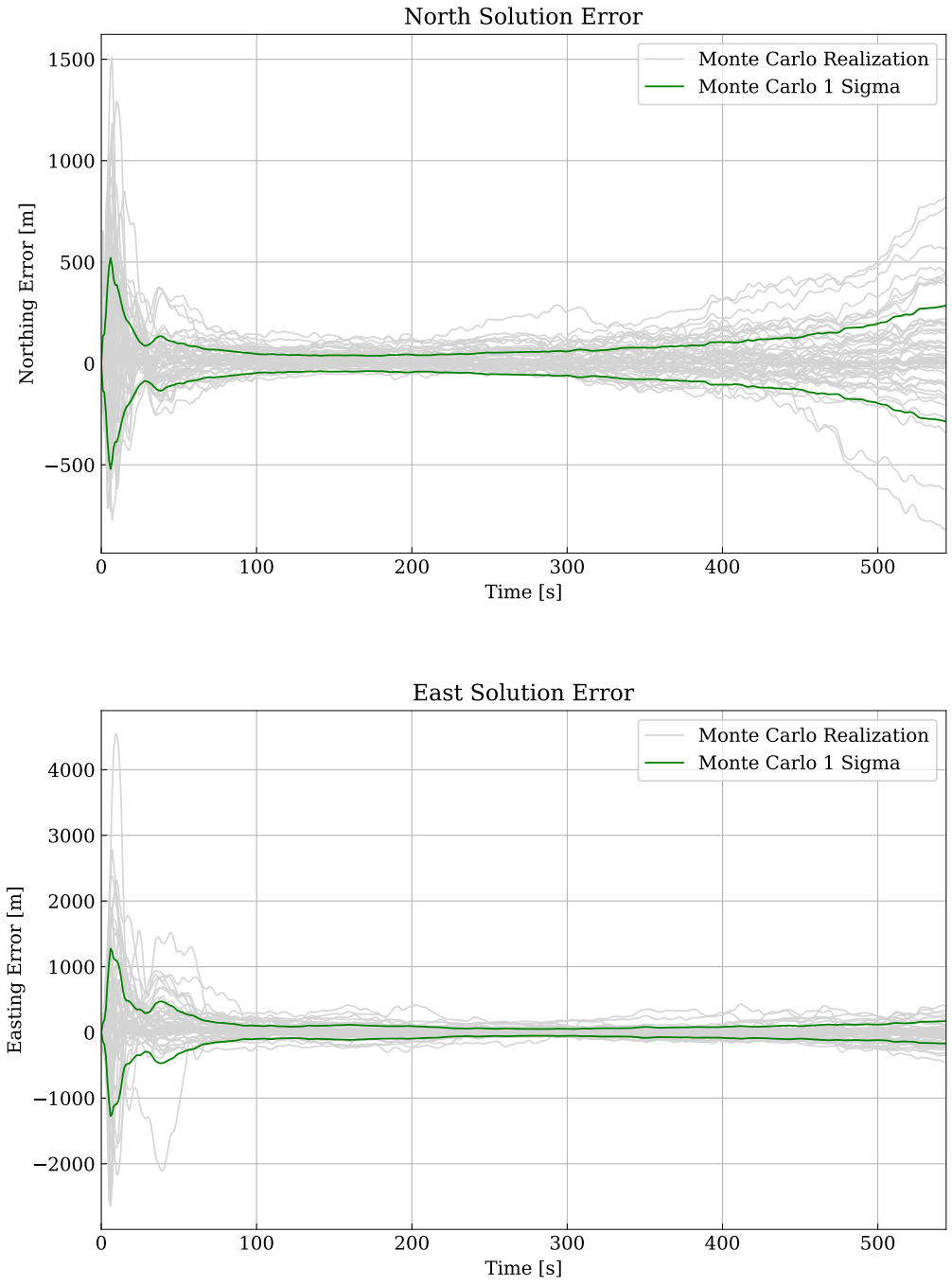

Figure 59: Vector MagNav Monte Carlo Simulation northing and easting results. These simulations were conducted with random locations over Australia.

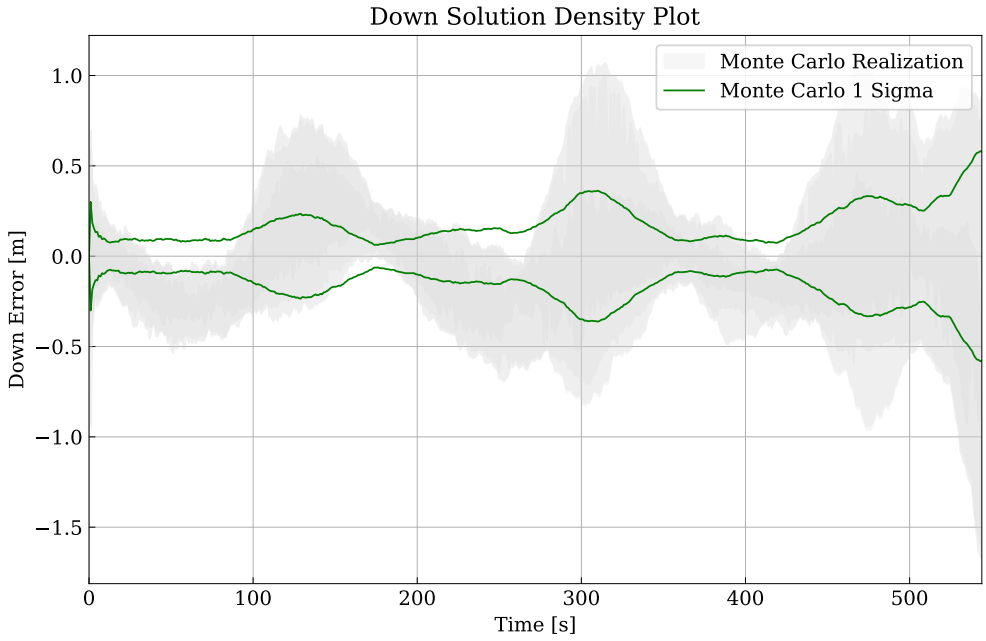

Figure 60: Random location vector MagNav Monte Carlo simulation down results.

While the results of this Monte Carlo simulation appear encouraging, the average performance statistics for all five trajectories tell a different story. These performance statistics are shown below in Table 6.

Table 6: Average navigation grade IMU MagNav Monte Carlo Simulation results.

Measurement	**Vector MagNav**	**Scalar MagNav**	**IMU Only**
MAE North Error (m)	212.6	231.93	490.3
STD North Error (m)	282.0	322.0	613.3
MAE East Error (m)	243.6	206.31	443.1
STD East Error (m)	409.2	288.3	544.0
MAE Down Error (m)	0.38	0.30	0.32
STD Down Error (m)	0.41	0.23	0.26
DRMS Error (m)	514.3	437.3	827.2

These results do not show significant performance improvements and in fact do not out-perform the scalar results for the same IMU grade shown in Section 4.3. As a result of the implementation of vector MagNav, it does not perform as expected.

Canciani [12] outlines the filter design and required derivatives for vector MagNav. However, due to time constraints, finite differencing was used to calculate the derivatives in the vector MagNav system. This process had shown to be sufficient for scalar MagNav, however given the filter performance shown in figures 57-58, we see that the filter is not well-behaved with respect to its covariance bounds, and this was after filter tuning had been performed. From these results it is clear that the finite differencing implementation of vector MagNav is inherently unstable. This instability becomes clear as the filter is able to constrain error initially, however over time the error starts to spike which points to filter instability. It is important to note that even though the filter uses the EMM as a map, it will not be distorted by a potential sensor mismatch like the results seen in Section 4.4. Since the EMM was used as both a measurement source, and magnetic anomaly map, the results of this section and those in section 4.4 should not be compared. These results do not invalidate vector MagNav for a hypersonic aircraft, however they invalidate the viability of finite differencing for vector MagNav. These results do show that even with filter stability issues, vector MagNav performs close to scalar MagNav for HGVs.

4.6 Result Trends

This section covered the results from the simulations conducted for this research. The key enabling work for these simulations was understanding the correct map upwards continuation distance. After this was completed, simulations using the Australian Magnetic Anomaly Map and HGV trajectories were conducted. Then, to simulate world-wide navigation capabilities, these same trajectories were simulating using the EMM as the map. Lastly a trial of vector MagNav was conducted on these trajectories. Of these, the most realistic results were achieved using the Australia Magnetic Anomaly Map.

All results show a consistent trend, all under-perform the results for MagNav on a non-hypersonic aircraft. There are two reasons why this might be: IMU mechanization issues and low magnetic information as a result of high altitude.

First, mechanization issues plagued the simulation of hypersonic MagNav. Since mechanization and reverse mechanization were simulated with two different systems, they had slightly different underlying assumptions. When normal solutions are processed in this method the error is negligible, however that was not the case with hypersonic solutions. To trouble shoot this issue, the filter was run with a noiseless IMU on a hypersonic trajectory. From this filter it was directly observed that more mechanization errors were present when the IMU was run at a lower rate. As a result, the IMU rate was increased to 1000 Hz from 100 Hz. This update rate removed the majority of the error, however there was still some error in the range of 10 m present in the noiseless mechanization, however noisy IMU solutions presented expected results.

The second and most probable reason for the filter under performing on hypersonic trajectories is the magnetic information decay at higher altitudes. As noted in Section 2.2.1, the performance of MagNav decays at higher altitudes due to less information being available. Since this degradation in performance was expected to be offset by the higher speeds, it was expected that the flights would show better performance regardless of the altitude. However, this seems to not be the case, and this degradation from altitude did not exceed the benefits of the high speed, resulting in worse overall performance compared to a normal aircraft.

4.7 Summary

In summary, these simulations show the potential for MagNav on a HGV. Additionally, they show that to utilize MagNav on these hypersonic vehicles world-wide, additional mapping effort will be required. While this particular MagNav system has

seemingly under-whelming performance, the system performance can be increased by better error models. For the sake of convenience, all results are summarized in Table 7 below.

Table 7: All Monte Carlo Simulation results. Note all EMM based simulations will have a map-sensor mismatch, which significantly reduces overall performance.

Measurement	**MagNav**	**IMU Only**
Scalar navigation grade MAE north error (m)	231.93	490.3
Scalar navigation grade MAE east error (m)	206.31	443.1
Scalar navigation grade DRMS error (m)	437.3	827.2
Vector navigation grade MAE north error (m)	212.6	490.3
Vector navigation grade MAE east error (m)	243.6	443.1
Vector navigation grade DRMS error (m)	514.3	827.2
Scalar tactical grade MAE north error (m)	1 628.8	2 704.8
Scalar tactical grade MAE east error (m)	1 223.5	1 872.7
Scalar tactical grade DRMS error (m)	3 455.5	4 427.5
EMM navigation grade MAE north error (m)	1 623.47	664.30
EMM navigation grade MAE east error (m)	1 147.2	463.5
EMM navigation grade DRMS error (m)	2 717.8	1 062.4

V. Conclusions

This thesis successfully implemented the Magnetic Navigation (MagNav) system designed by Canciani [2] on hypersonic trajectories provided by Lysak [8]. Implementation was done within the NavToolKit framework as a Monte Carlo Simulation. This was done in order to have a complete analysis of the capabilities of the navigation filter.

In order to achieve this goal, a detailed analysis of available literature regarding potential plasma magnetic noise was conducted. This research concluded that for magnetic fields, plasma is magnetically permeable, but may create high frequency noise. The noise was assumed to be able to be removed by separation and a low pass filter. Separation is achievable by placing the magnetometer inside the aircraft away from the outer areas where the plasma could form. For cases when separation is not able to remove all plasma induced noise, low pass filtering should be able to remove all remaining noise. With this information from the literature, it is assumed that plasma will not create significant issues for a MagNav system.

Map availability and processing systems proved to be a significant challenge for hypersonic MagNav. The primary issue regarding map availability is that there is only one map with sufficient quality that is large enough to satisfy the needs for MagNav on a hypersonic vehicle. This map was the Australia Magnetic Anomaly Map. When trying to use the Australia Magnetic Anomaly Map, it became apparent that the current magnetic anomaly map handling systems for MagNav in NavToolKit were insufficient due to the challenges that arise with maps of this scale. After upgrades to these systems were completed, use of the Australia map started challenging prior assumptions for MagNav. These prior assumptions with respect to map altitudes had to be re-approached, and ended up forming one of the core contributions of this thesis, non-linear map spacing. This concept states that maps only need to be

upwards continued at intervals, which can be approximated with a polynomial. Non-linear map spacing is a concept that greatly reduces the computational burden of running MagNav for both hypersonic and traditional aircraft flight paths.

After map handling systems were upgraded, simulation could proceed. The basic form of simulation consisted of using the high quality Australia Magnetic Anomaly Map to provide both sensor measurements and the map source. This simulation demonstrated the viability of MagNav on a hypersonic aircraft using a high quality map.

In order to test world-wide availability of MagNav, simulations were conducted using the Enhanced Magnetic Model (EMM). The EMM is a worldwide magnetic anomaly map. This map has satellite based magnetic measurements for both the scalar and vector magnetic fields. In order to more accurately demonstrate how this map might perform when used as the navigation map, sensor measurements were collected from the Australia map, and the filter used the EMM as the map source. This filtering method showed a considerable decrease in navigation accuracy, and showed that the EMM is not viable for use as the sole magnetic anomaly map for MagNav due to its inaccuracies.

The final set of simulations that were conducted used the vector components of the EMM, without additional noise. This was done to complete the fifth research objective and showcase the abilities of vector MagNav. These tests showed that implementing vector MagNav using finite differencing is not viable as the filter became unstable. However, these results were nearly on-par with the scalar MagNav, showing that a filter not implemented with finite differencing will outperform scalar MagNav on hypersonic aircraft.

All the simulations presented showed a consistent theme of under performance in comparison to MagNav on a non-hypersonic aircraft. Under performance can be at-

tributed to two factors, breakdown of inertial measurement unit (IMU) assumptions at hypersonic speeds, and lack of map data at high altitudes. Errors originating from map data are the only potential issues that are unique to hypersonic MagNav. Maps loosing data at high altitudes was both expected and unavoidable. It was initially expected that the speed of hypersonic aircraft would automatically compensate for this, however this appears to not be the case. Finally, the breakdown of IMU assumptions is a difficult issue to pinpoint and should be the focus of future research.

The results presented in this thesis satisfy all the research objectives outlined in Section 1.2. This thesis was able to successfully implement MagNav on hypersonic trajectories and improve MagNav implementation and assumptions. This paper successfully demonstrates MagNav for hypersonic aircraft, however there is still significant room to improve these results.

5.1 Future Work

There are two categories of research that need to be examined, plasma modeling and IMU mechanization error examination; as this is the only error source with the potential to be corrected. In order to have a robust MagNav system on a hypersonic aircraft, the effects of the plasma sheath on a magnetic measurement need to be examined. This could take the form of a wind tunnel test and/or a Computational Fluid Dynamics (CFD) analysis. These tests will provide an improved understanding of the noise generated by the plasma, and in turn can be used to improve simulation realism. The second source of future work and improvement is to fully understand the IMU errors that started to arise. The source of these errors should be traced to either: reverse mechanization, mechanization, error approximation, or within the filtering system itself. This will improve results and provide insight to potentially invalid assumptions with how IMU data is processed for hypersonic aircraft.

Appendix A. Additional Navigation Grade IMU Australia Map Simulations

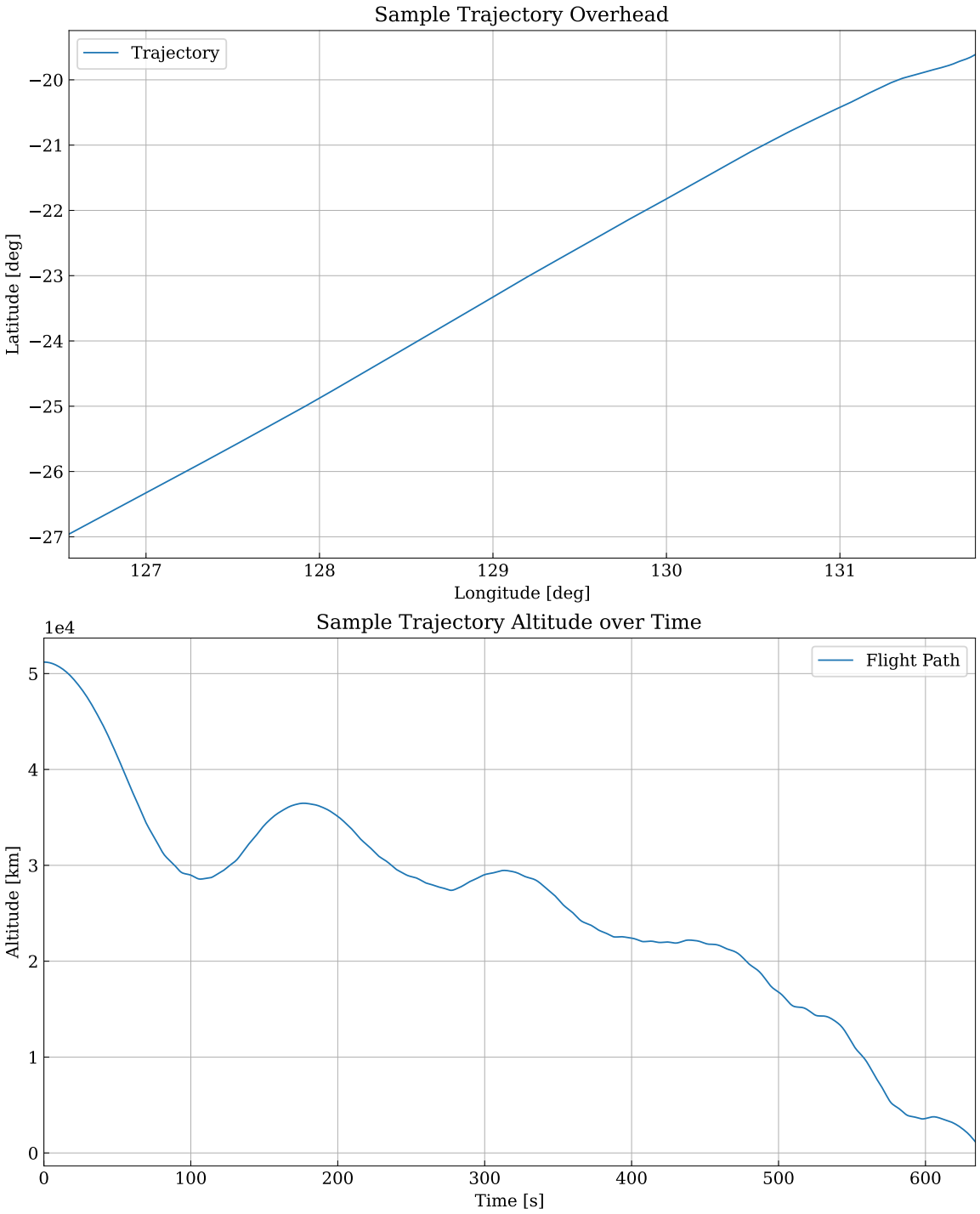

Figure 61: Second hypersonic trajectory flight path.

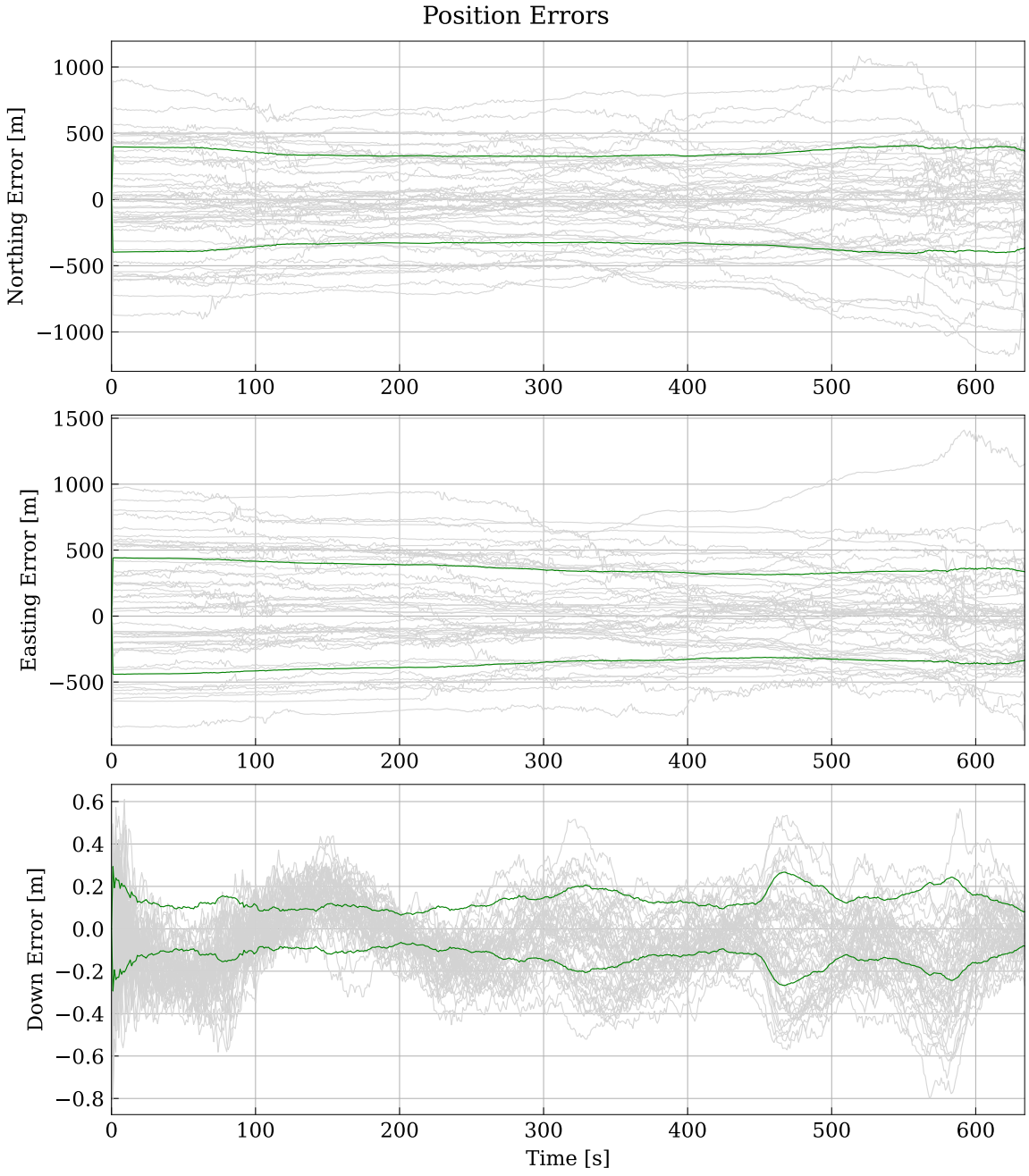

Figure 62: Second hypersonic trajectory navigation grade IMU MagNav filter performance.

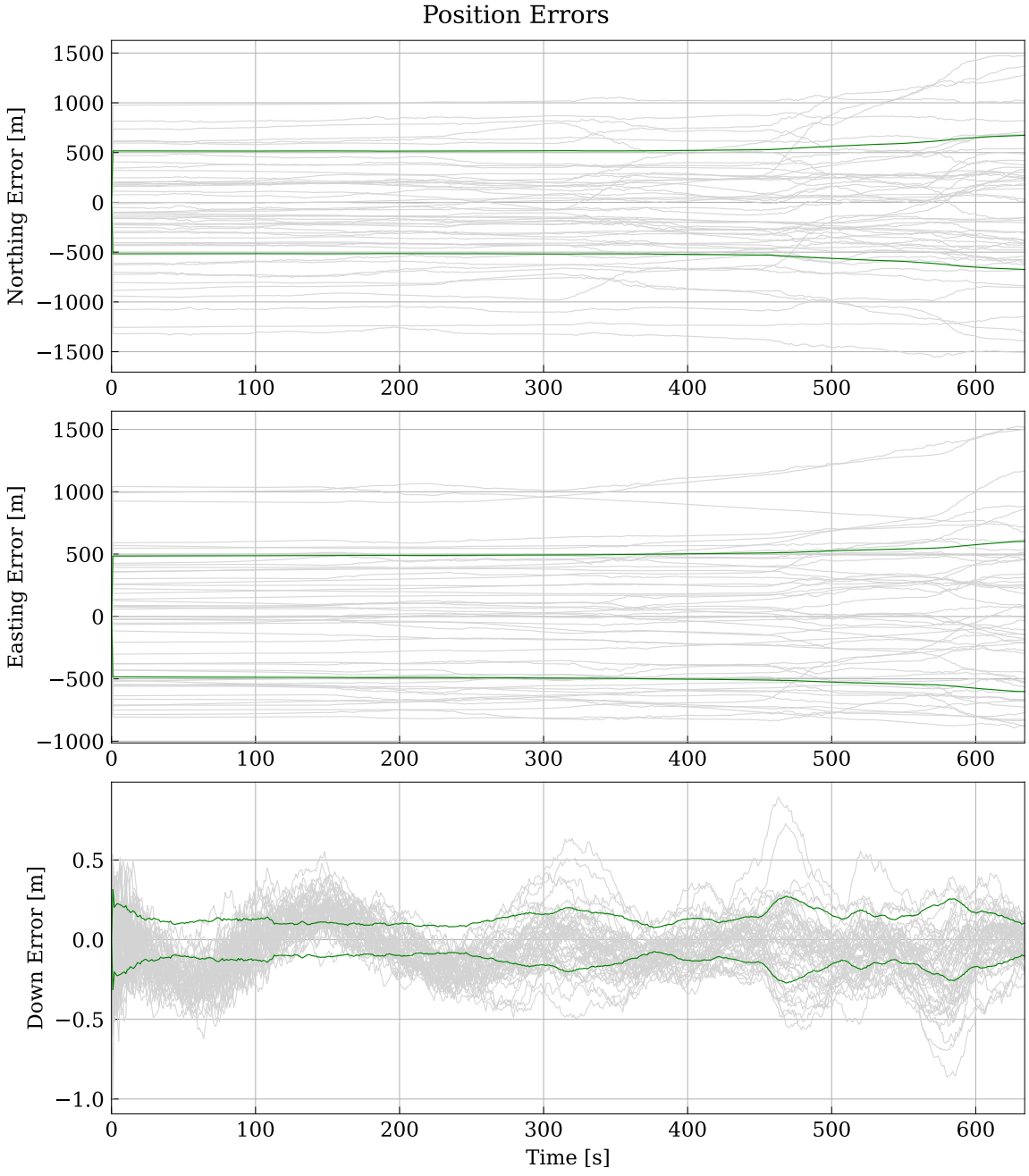

Figure 63: Second hypersonic trajectory unaided navigation grade IMU performance.

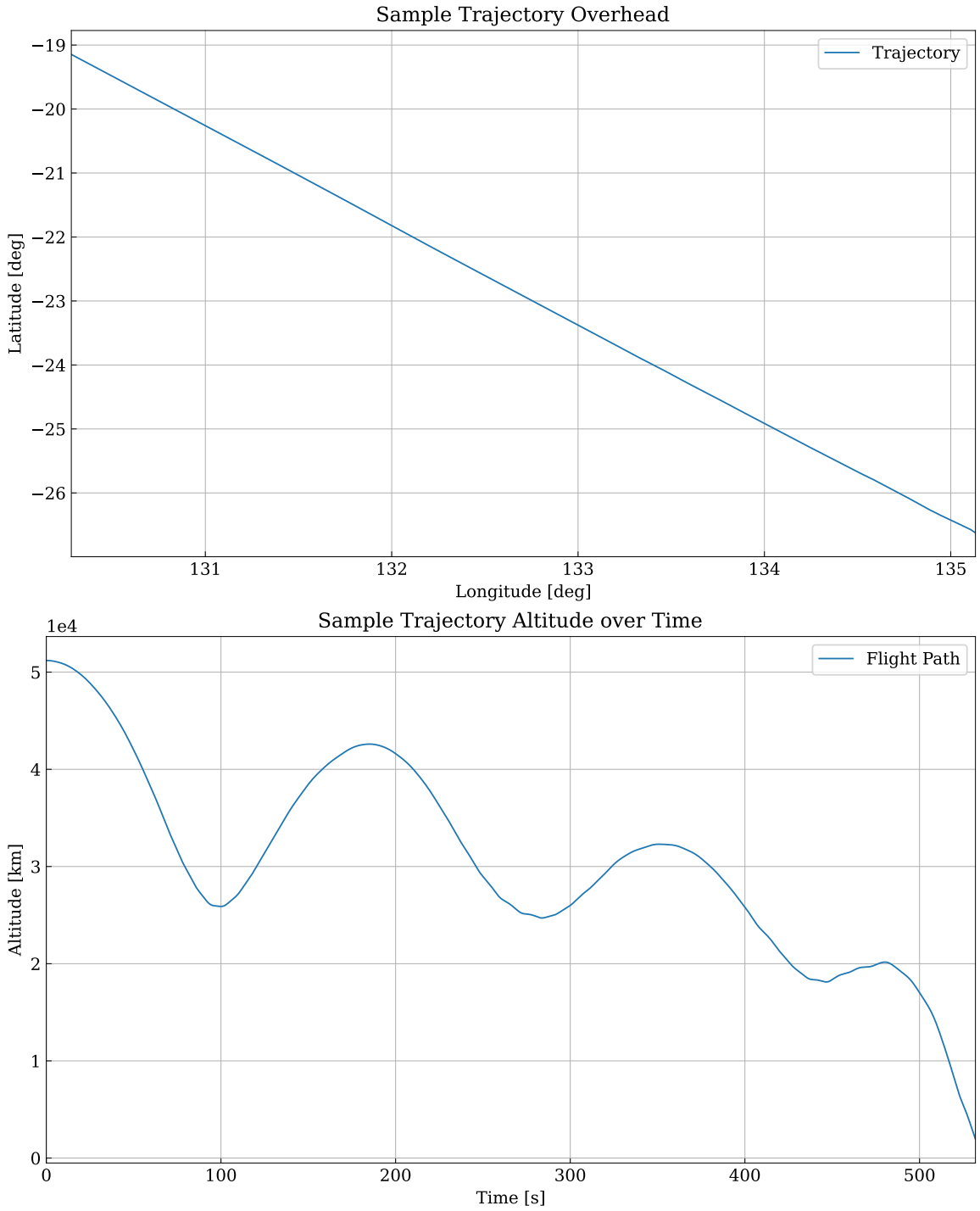

Figure 64: Third hypersonic trajectory flight path.

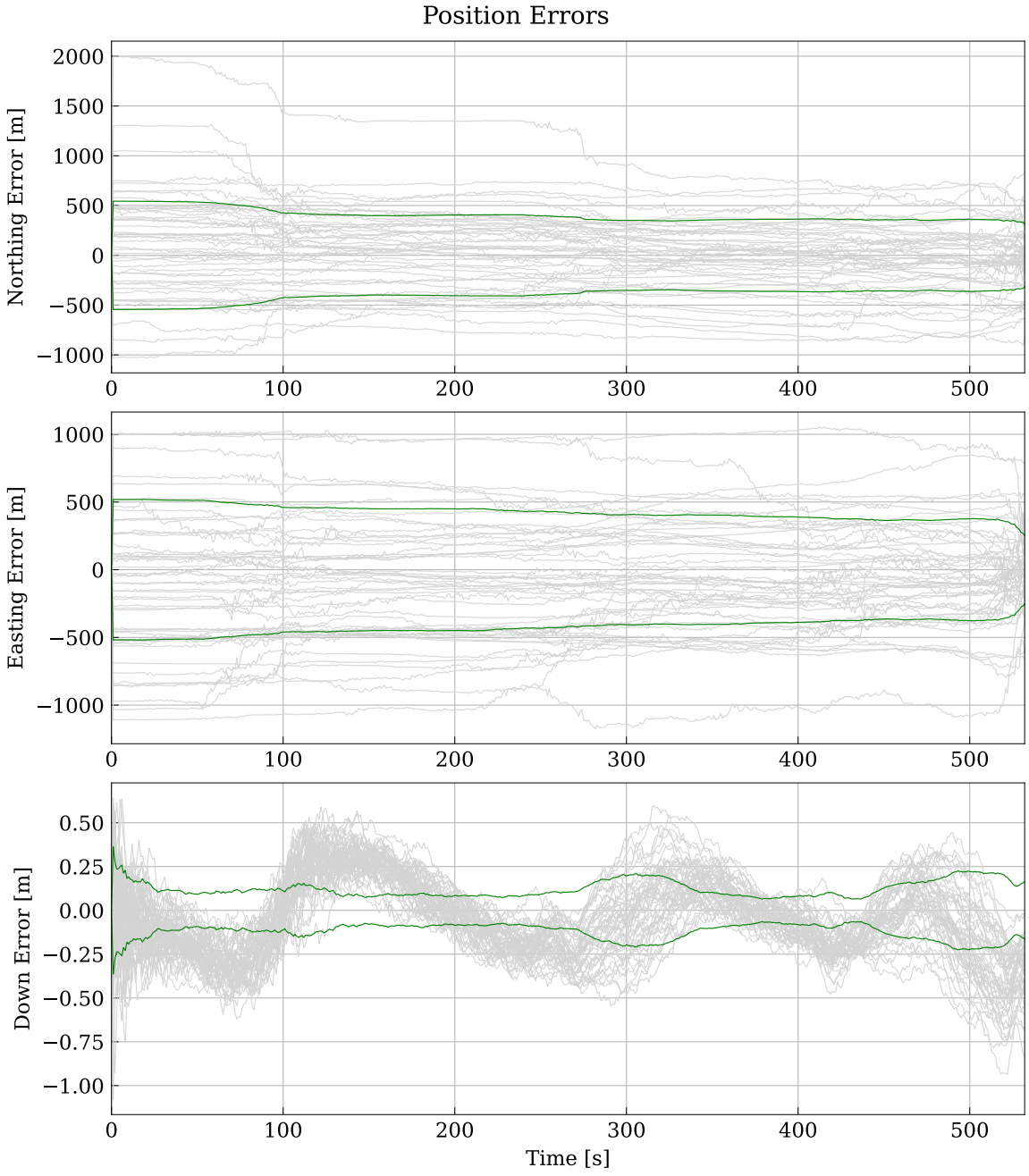

Figure 65: Third hypersonic trajectory navigation grade IMU MagNav filter performance.

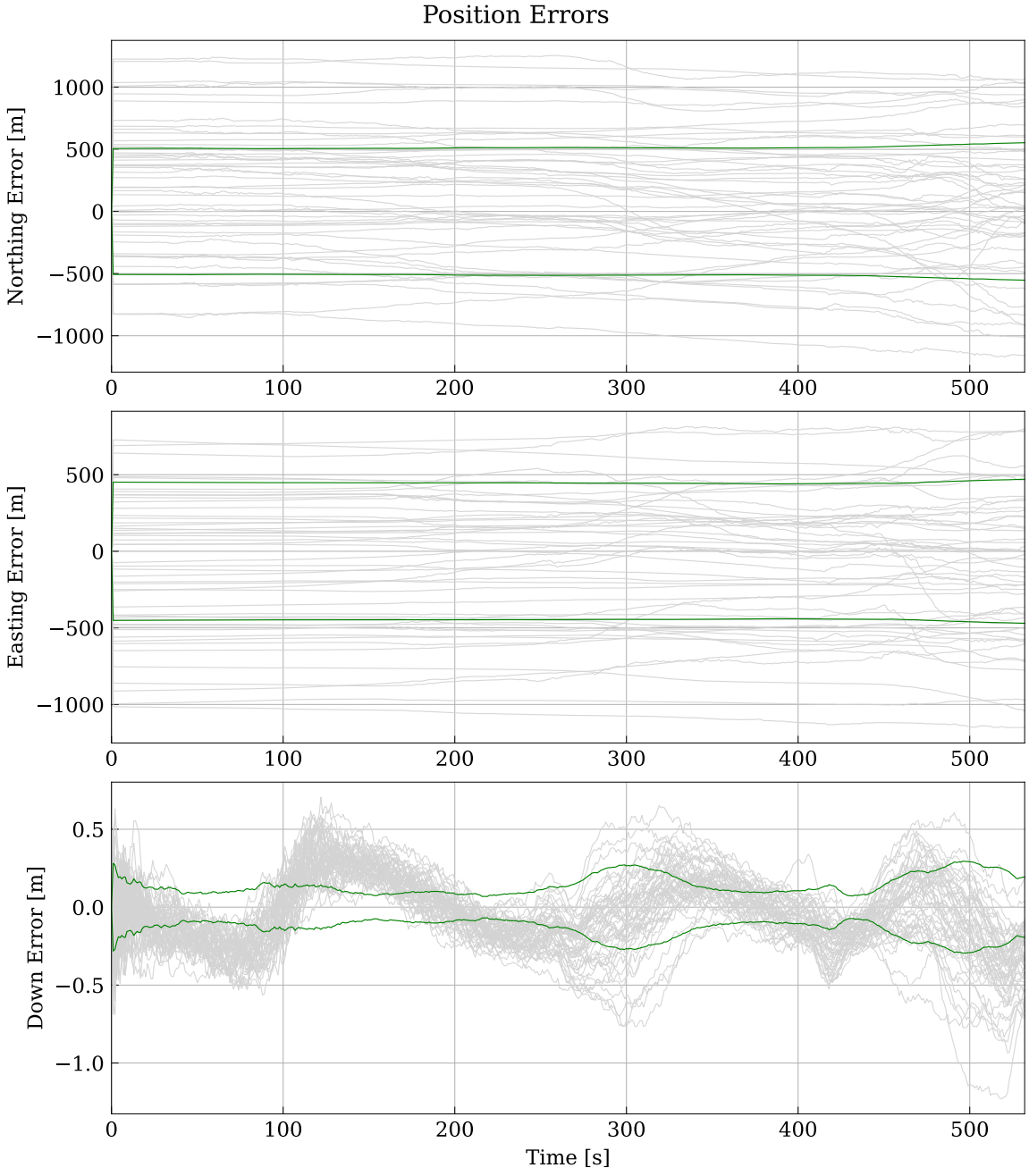

Figure 66: Third hypersonic trajectory unaided navigation grade IMU performance.

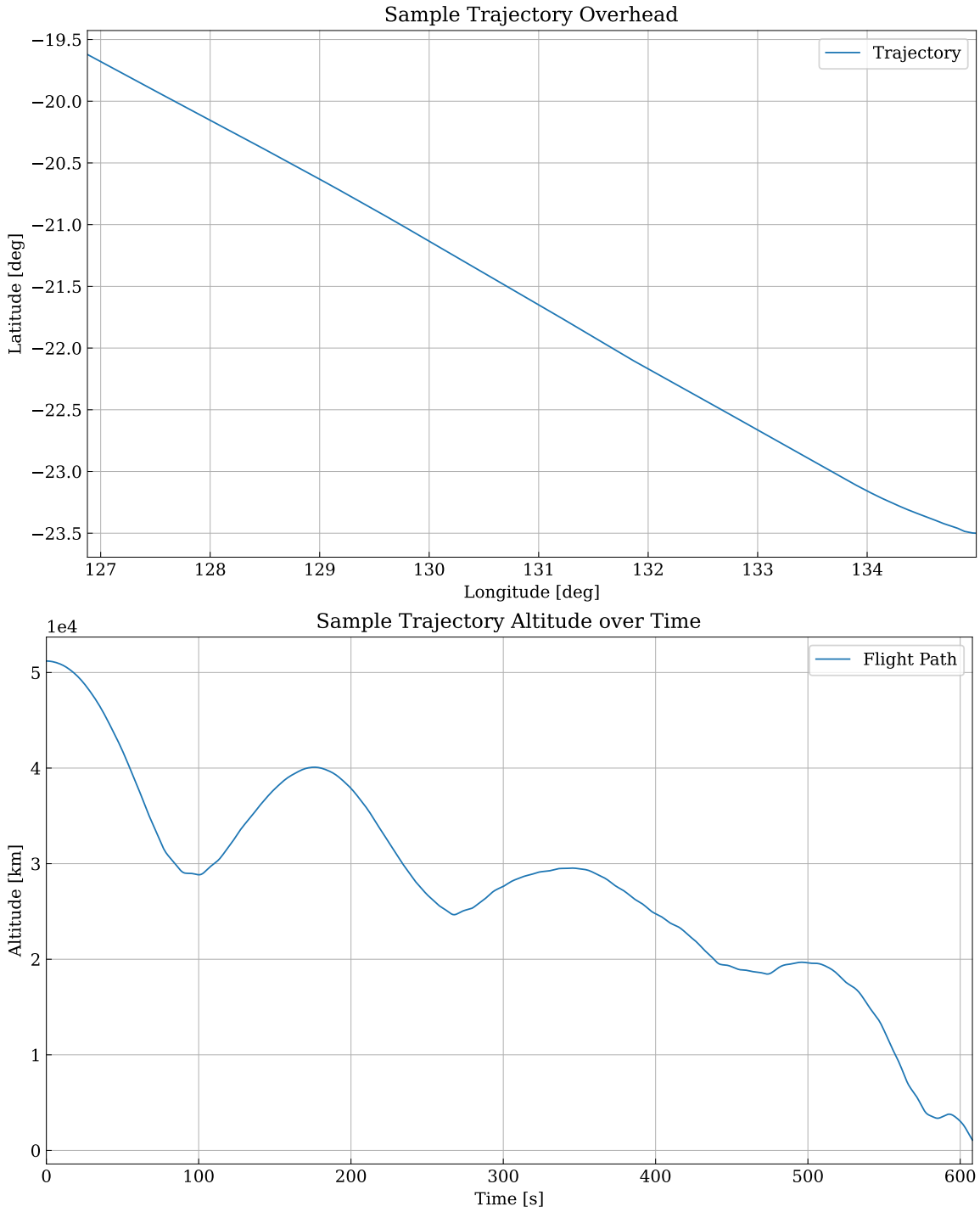

Figure 67: Fourth hypersonic trajectory flight path.

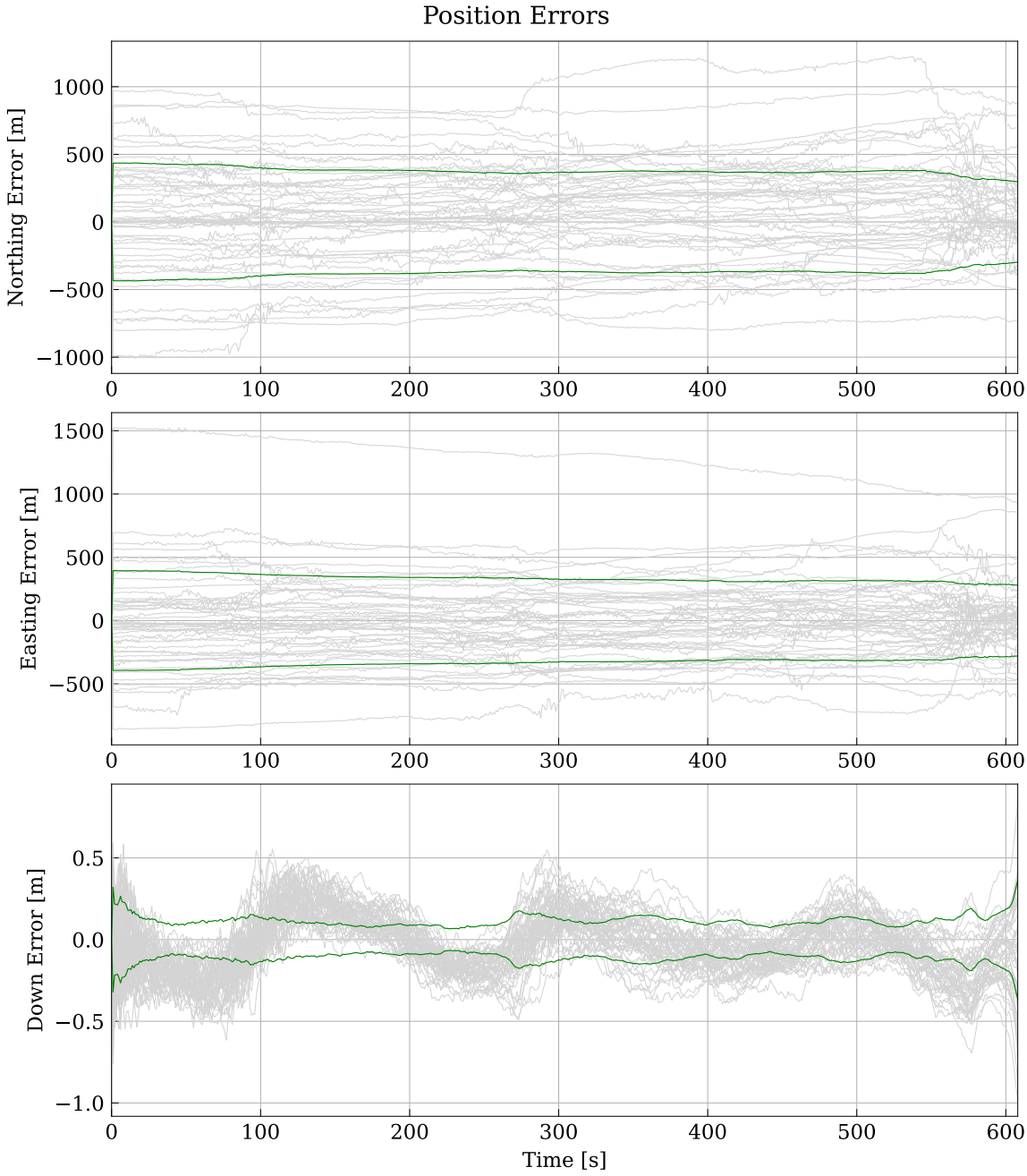

Figure 68: Fourth hypersonic trajectory navigation grade IMU MagNav filter performance.

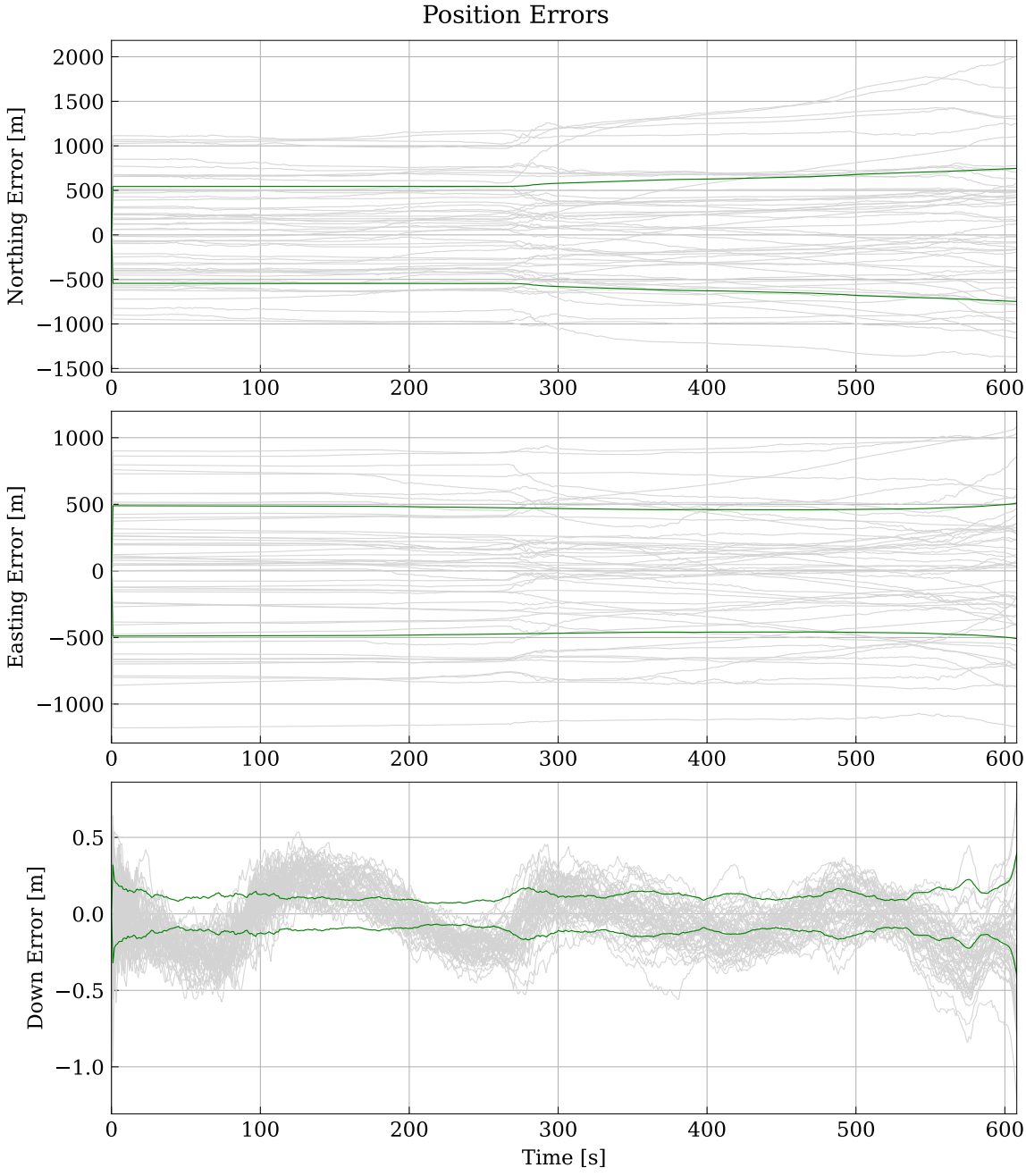

Figure 69: Fourth hypersonic trajectory unaided navigation grade IMU performance.

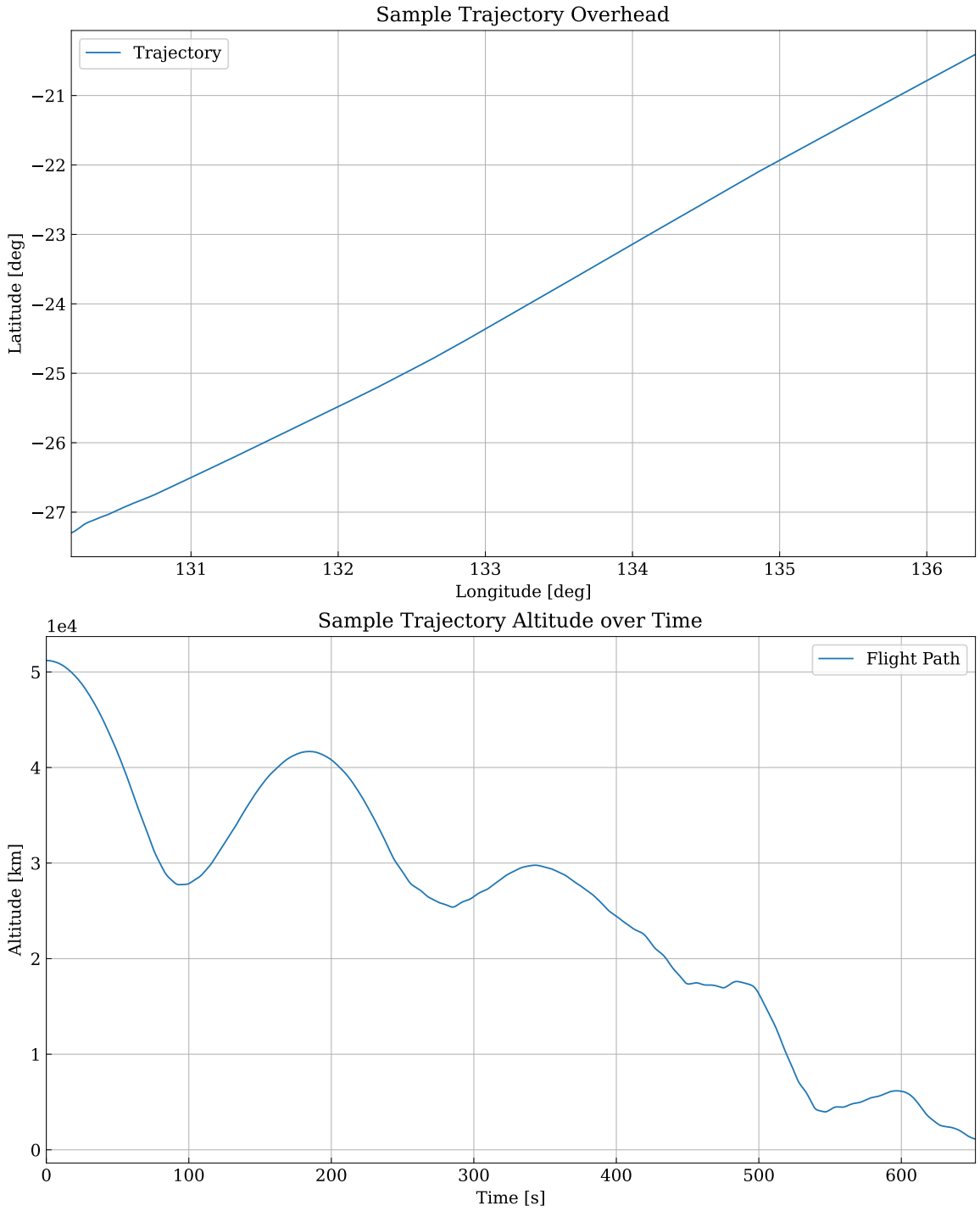

Figure 70: Fifth hypersonic trajectory flight path.

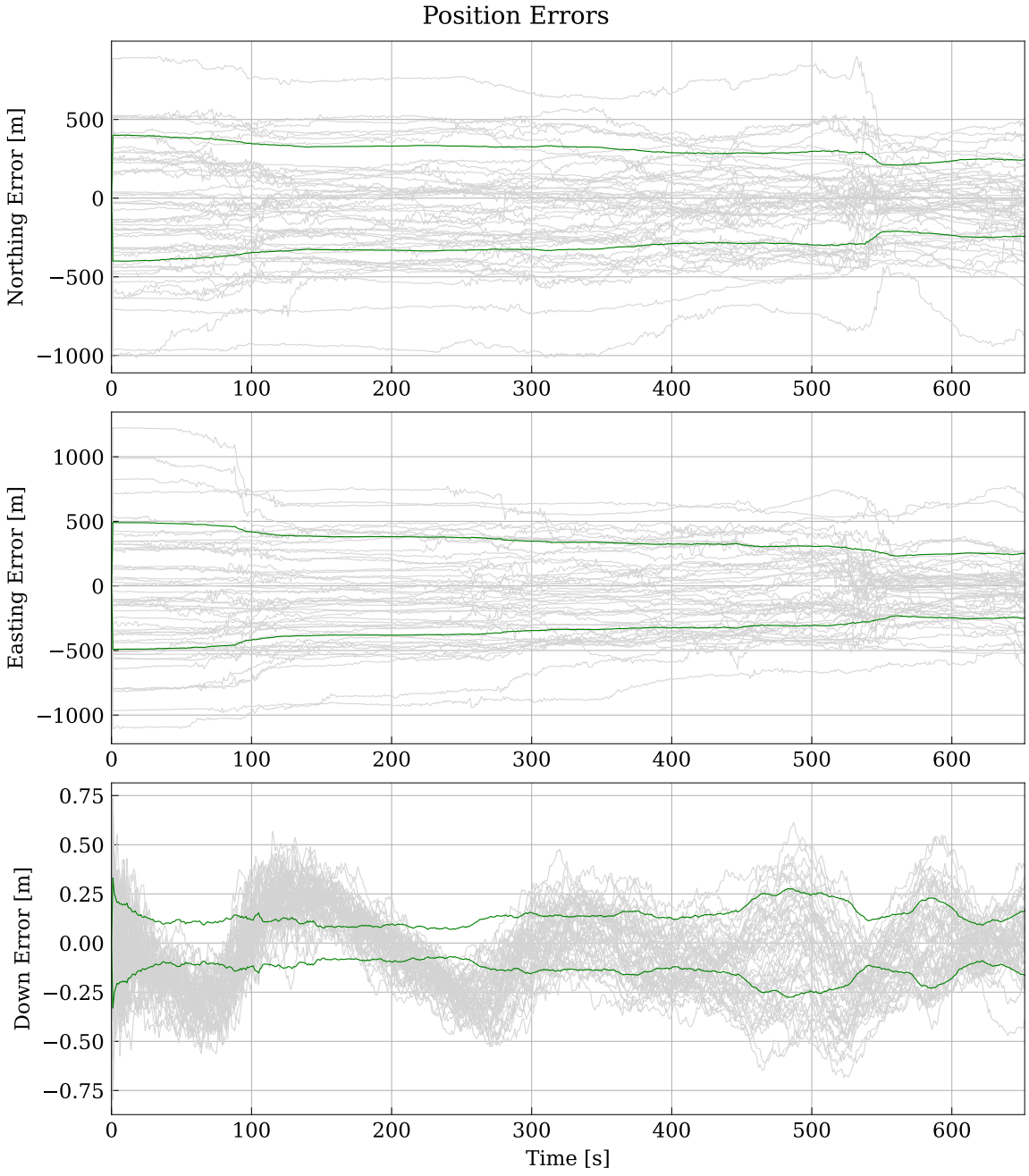

Figure 71: Fifth hypersonic trajectory navigation grade IMU MagNav filter performance.

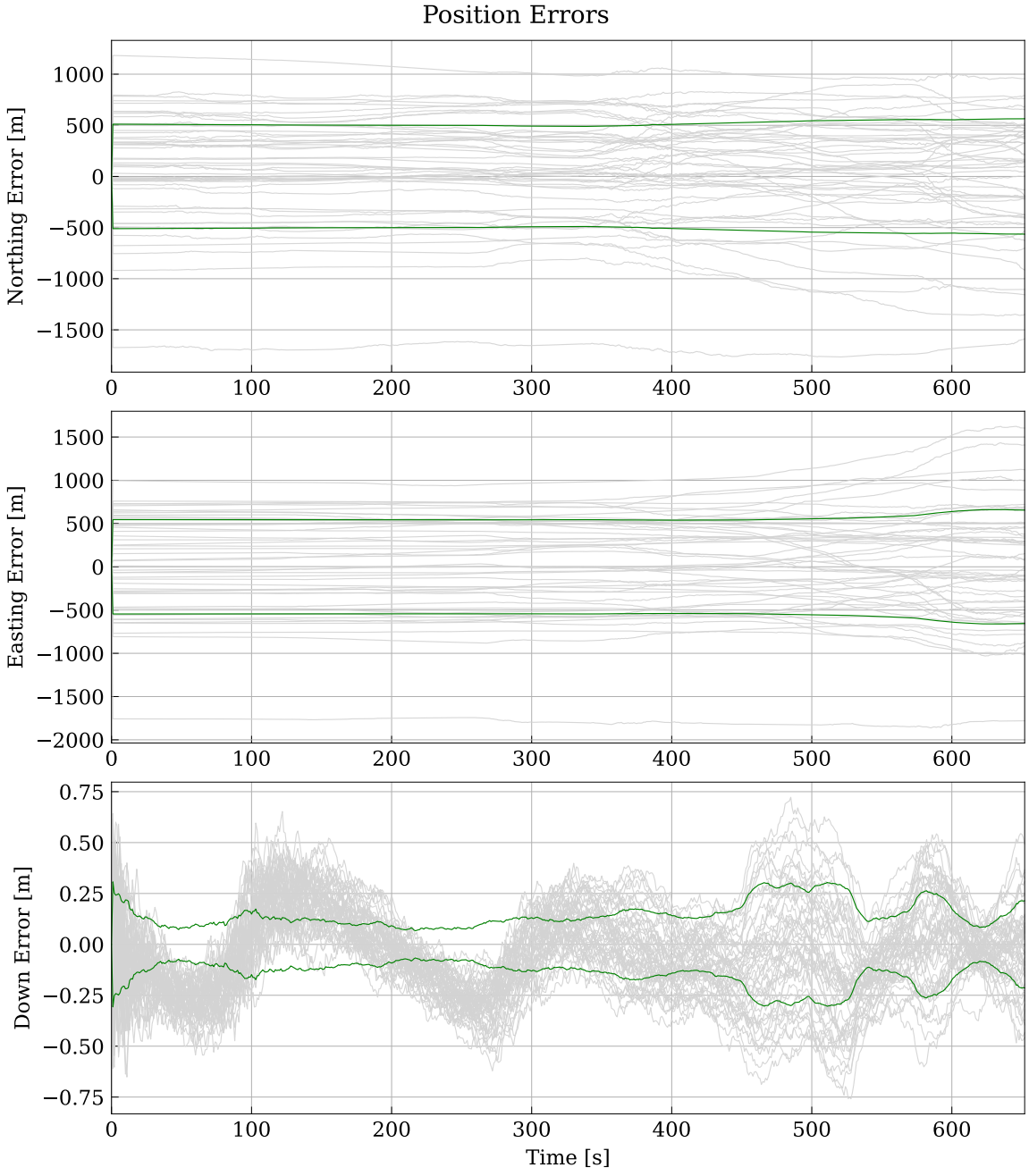

Figure 72: Fifth hypersonic trajectory unaided navigation grade IMU performance.

Appendix B. Additional Tactical Grade IMU Australia Map Simulations

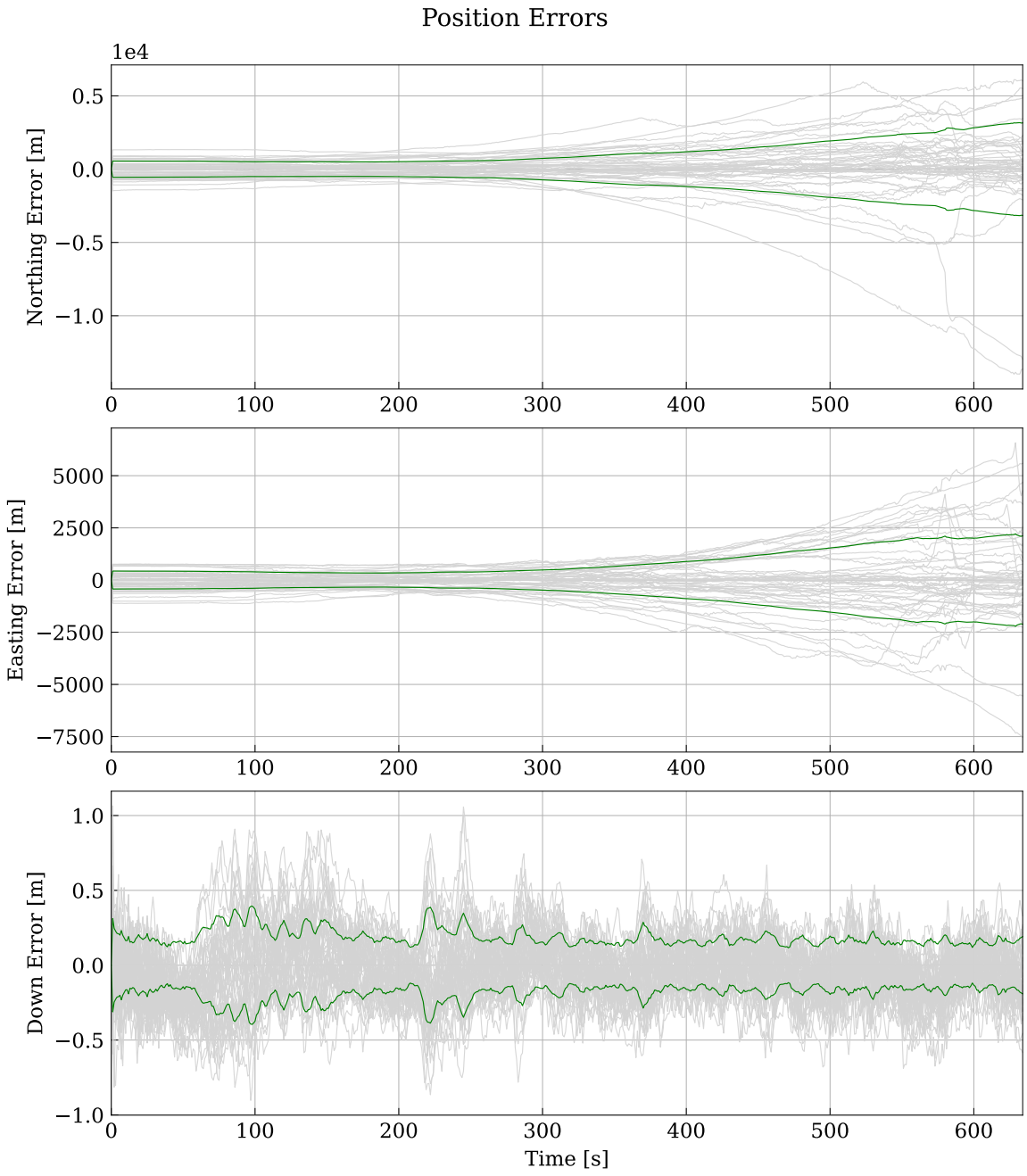

Figure 73: Second hypersonic trajectory tactical grade MagNav filter performance.

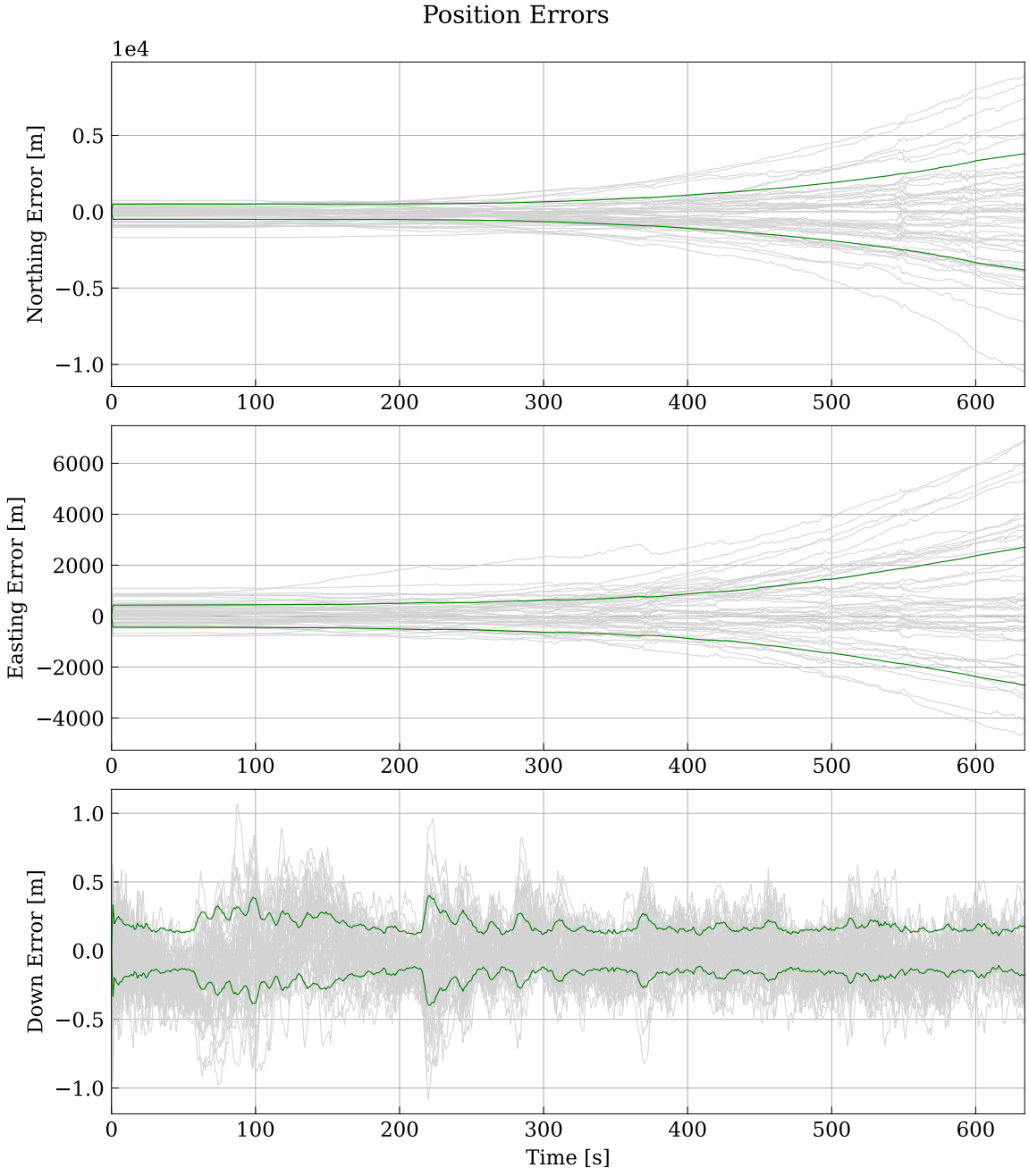

Figure 74: Second hypersonic trajectory unaided tactical grade IMU performance.

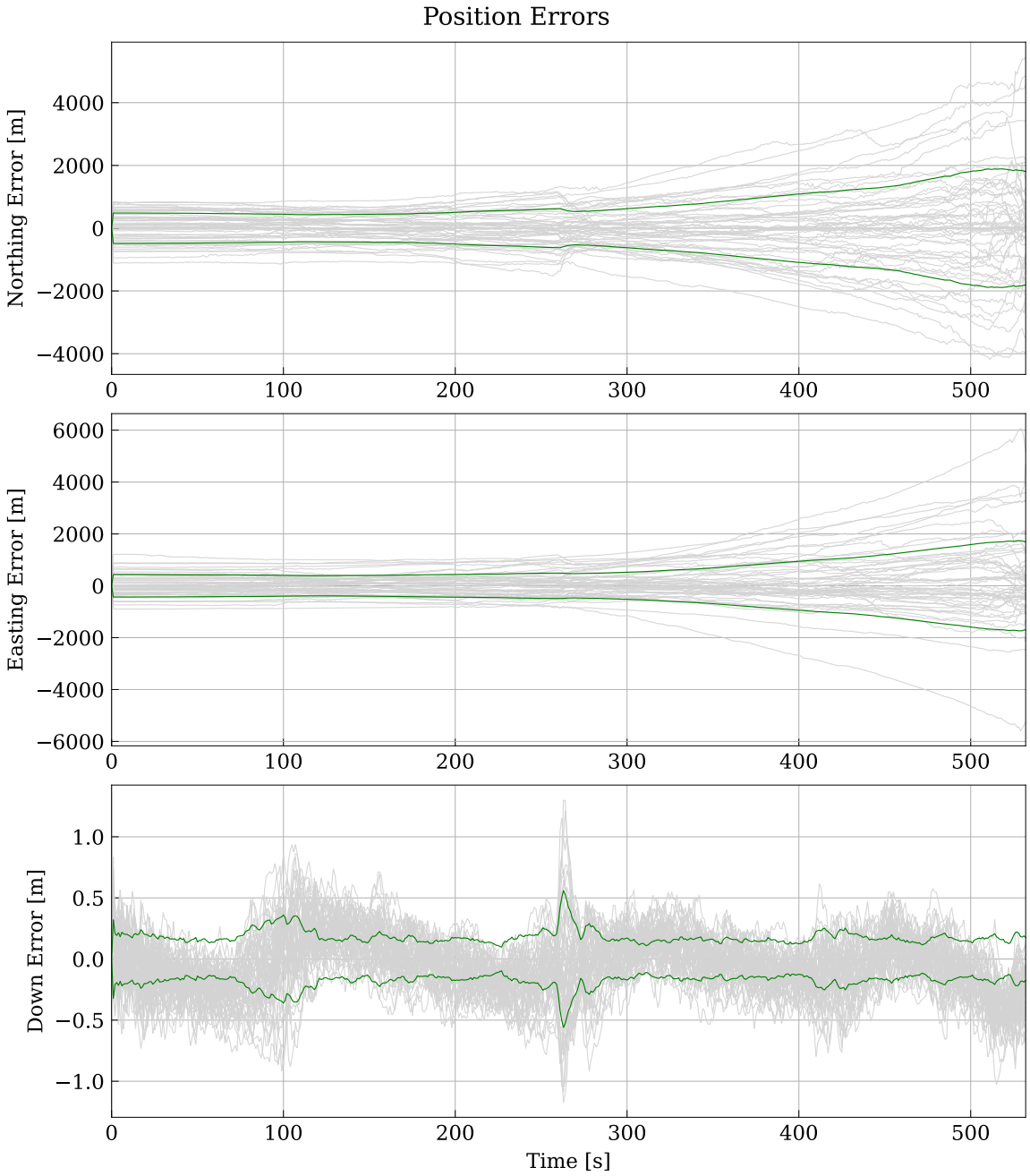

Figure 75: Third hypersonic trajectory tactical grade MagNav filter performance.

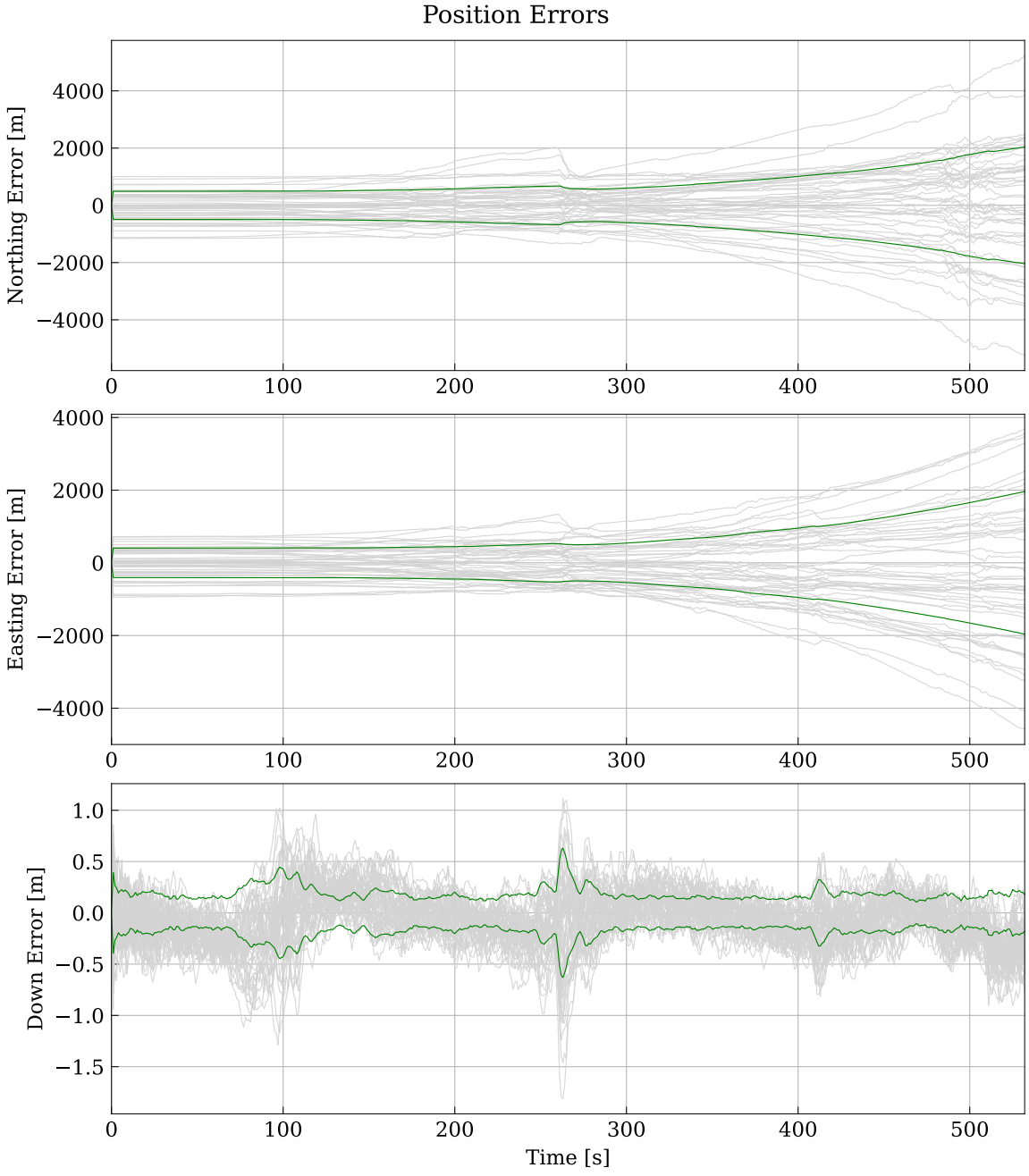

Figure 76: Third hypersonic trajectory unaided tactical grade IMU performance.

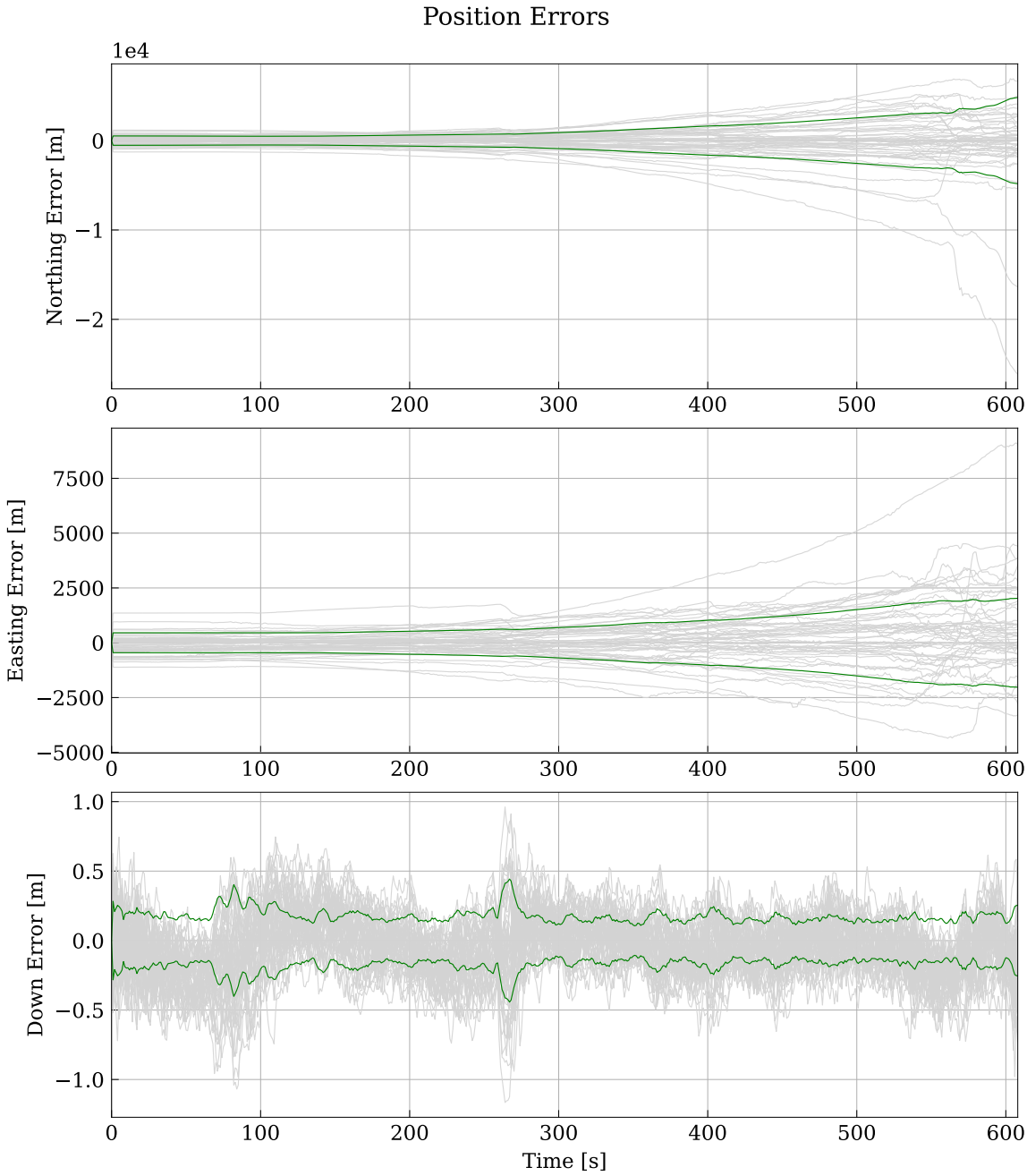

Figure 77: Fourth hypersonic trajectory tactical grade MagNav filter performance.

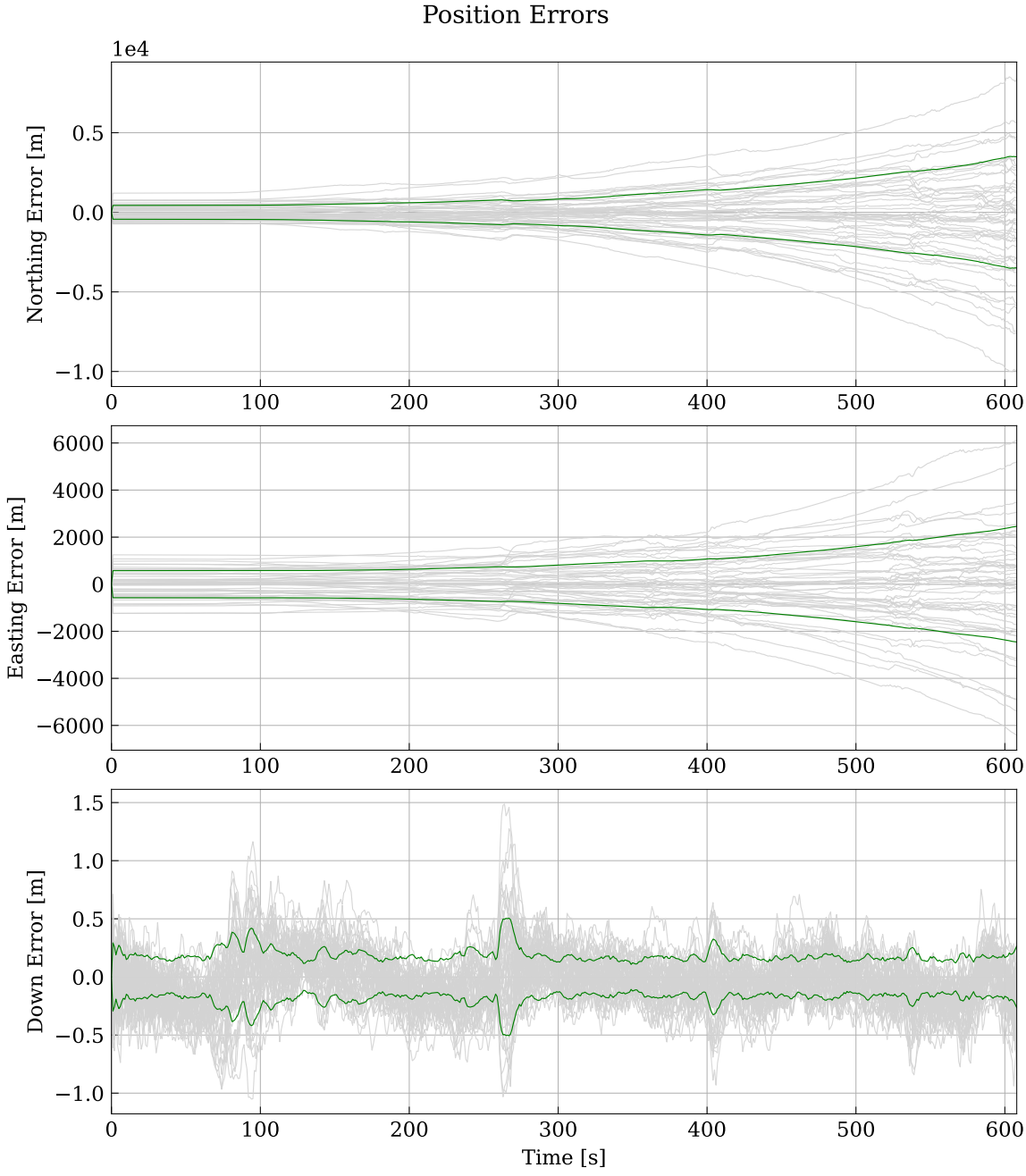

Figure 78: Fourth hypersonic trajectory unaided tactical grade IMU performance.

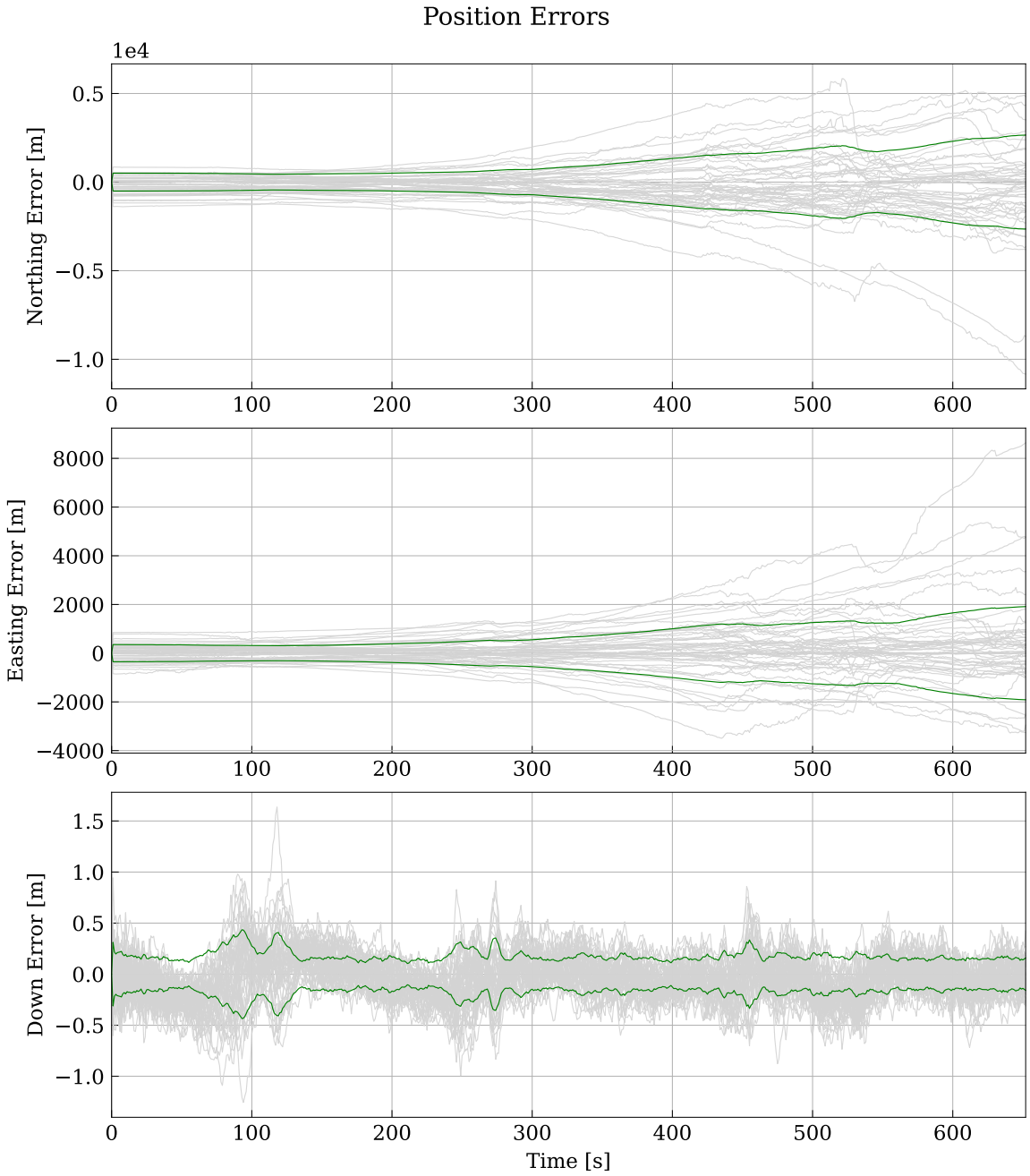

Figure 79: Fifth hypersonic trajectory tactical grade MagNav filter performance.

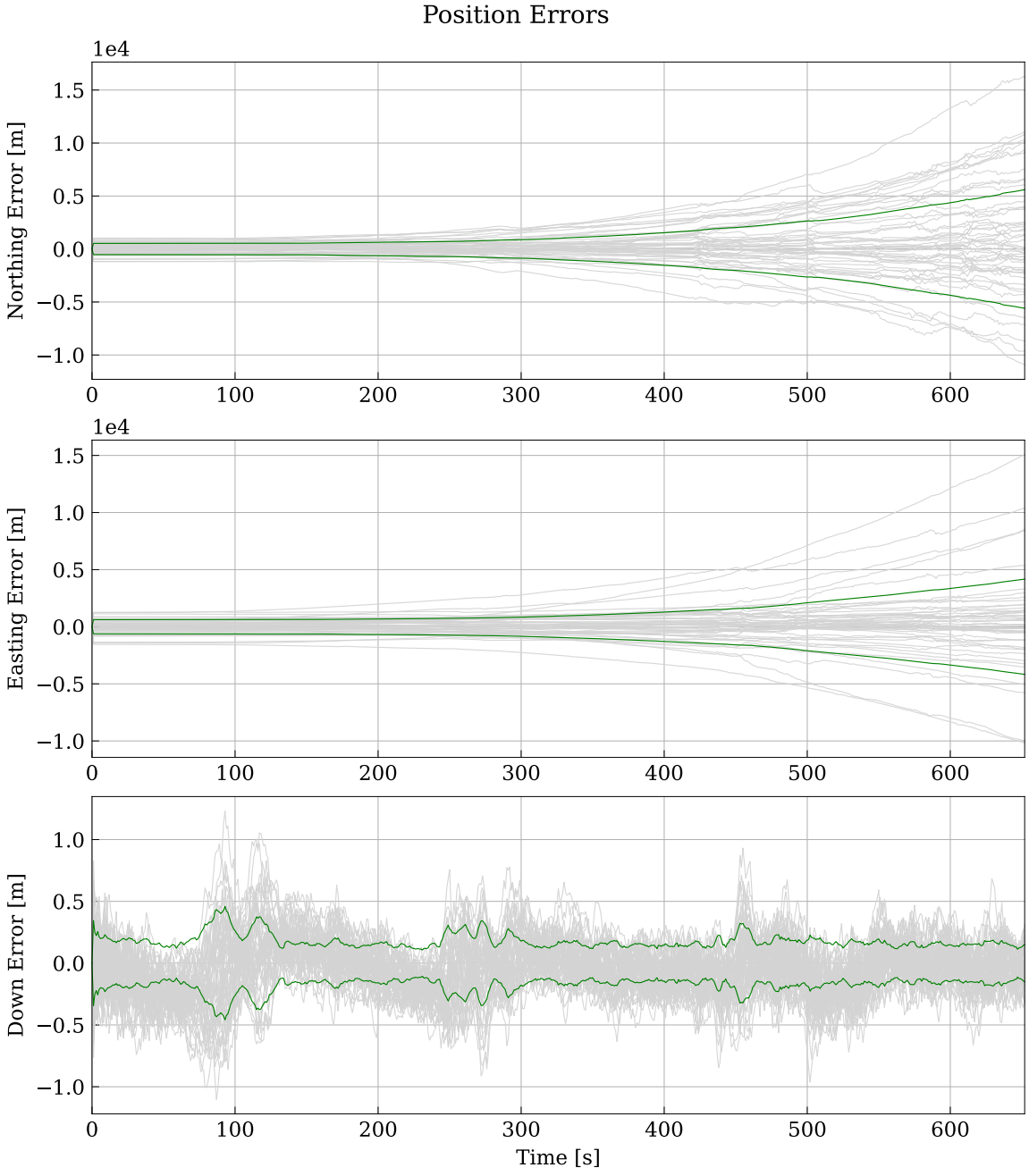

Figure 80: Fifth hypersonic trajectory unaided tactical grade IMU performance.

Appendix C. Additional Navigation Grade IMU EMM Simulations

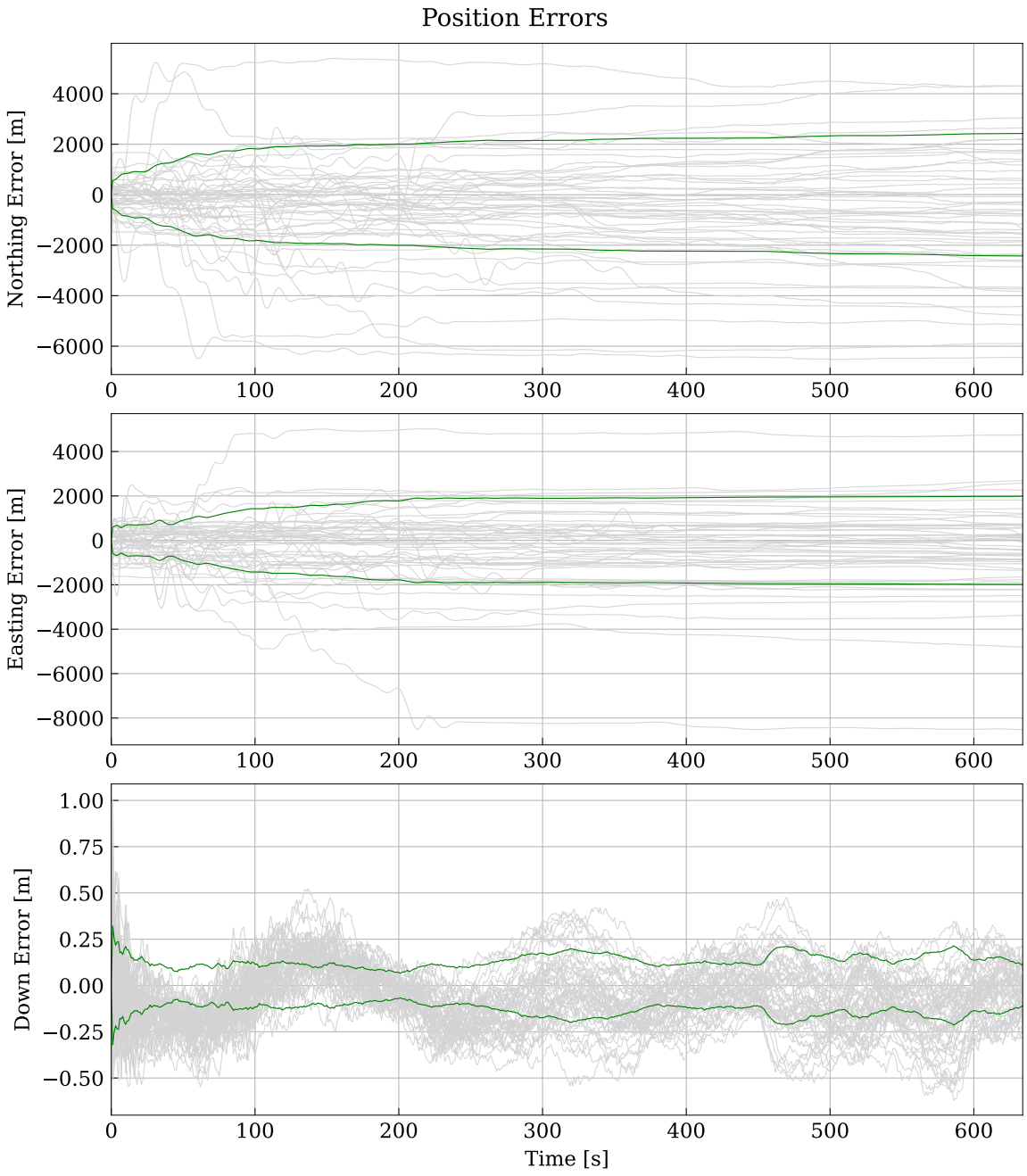

Figure 81: Second hypersonic trajectory navigation grade IMU MagNav filter performance using EMM as navigation map.

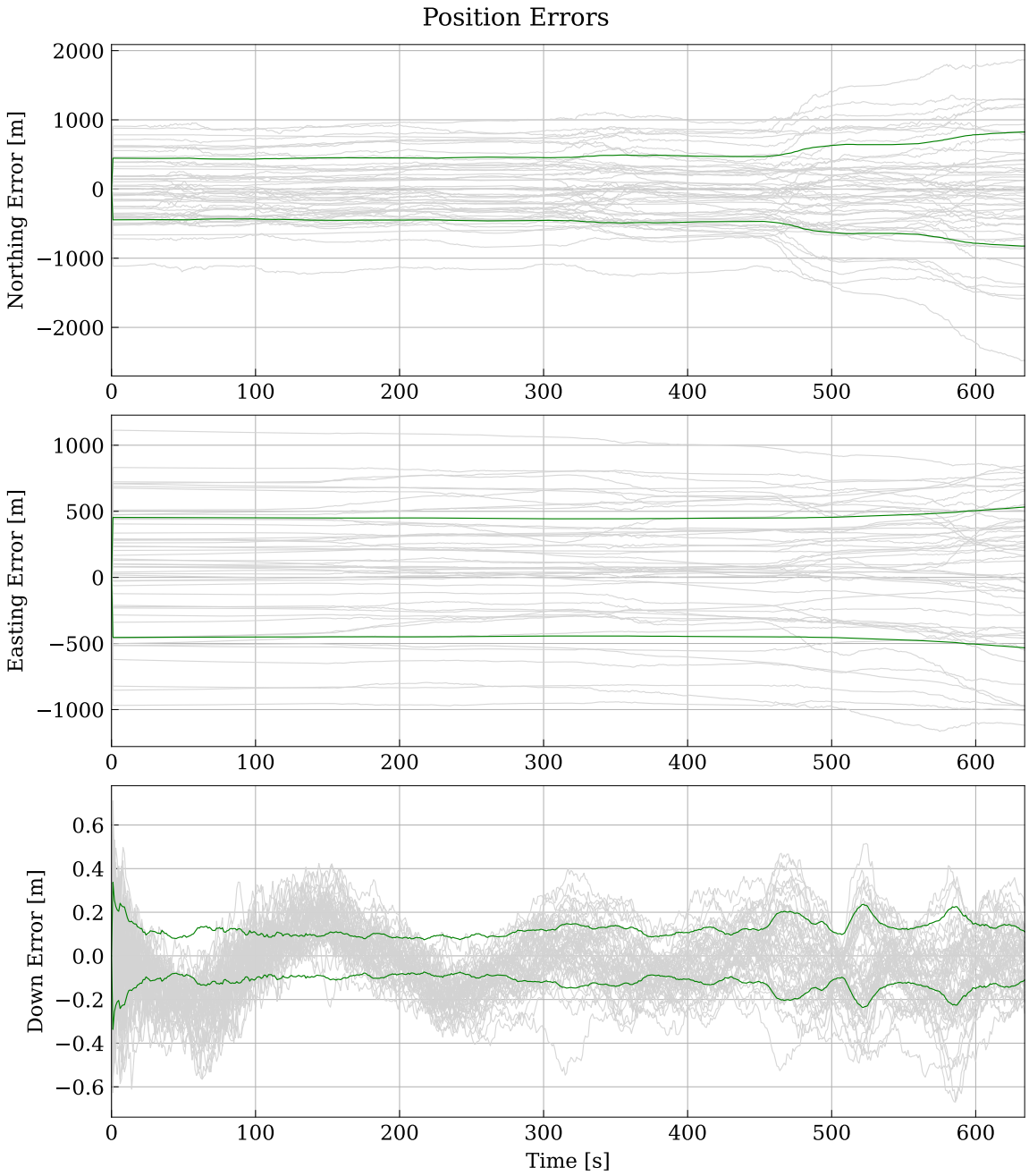

Figure 82: Second hypersonic trajectory unaided navigation grade IMU performance using initial conditions for the EMM navigation simulations.

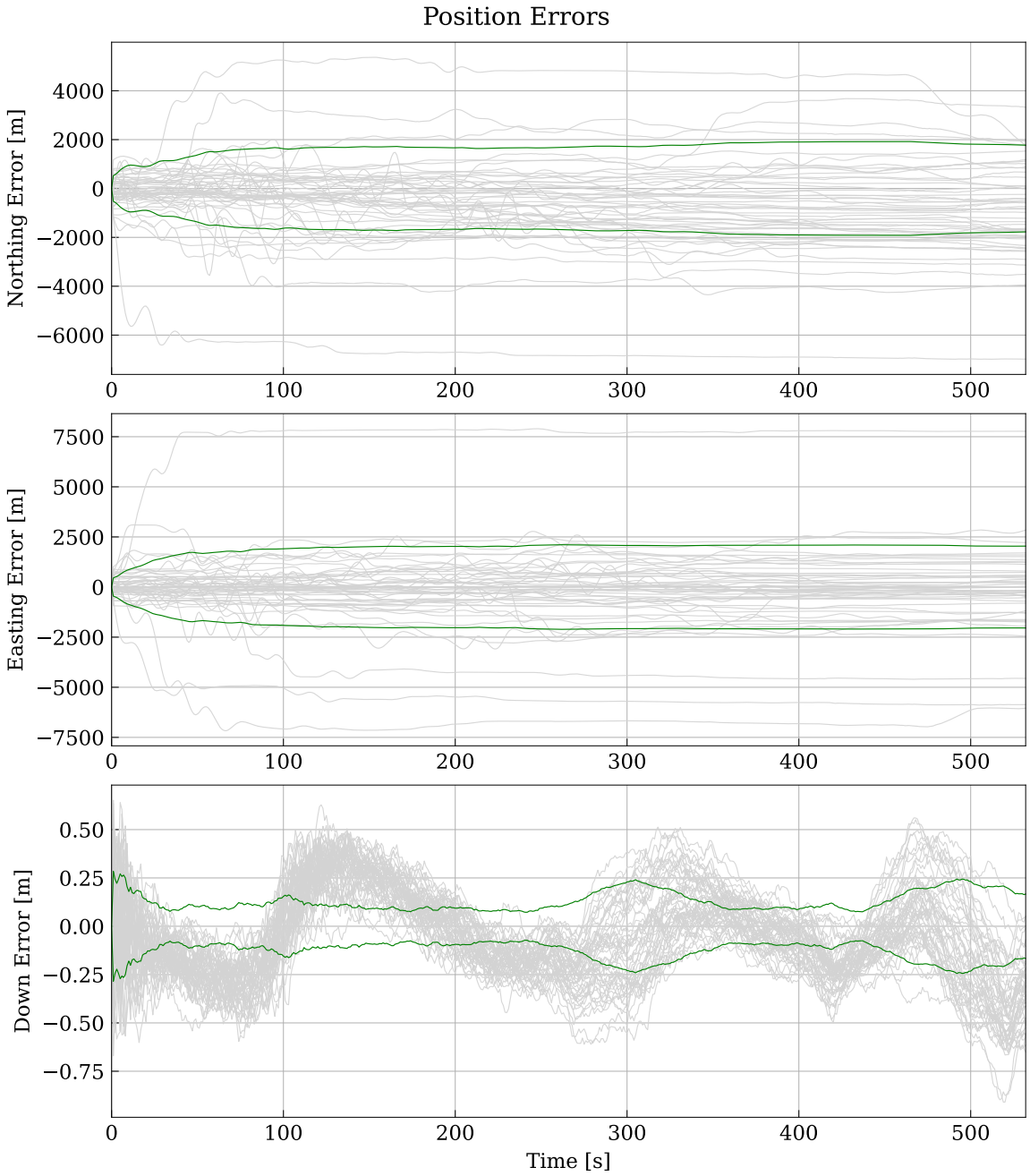

Figure 83: Third hypersonic trajectory navigation grade IMU MagNav filter performance using EMM as navigation map.

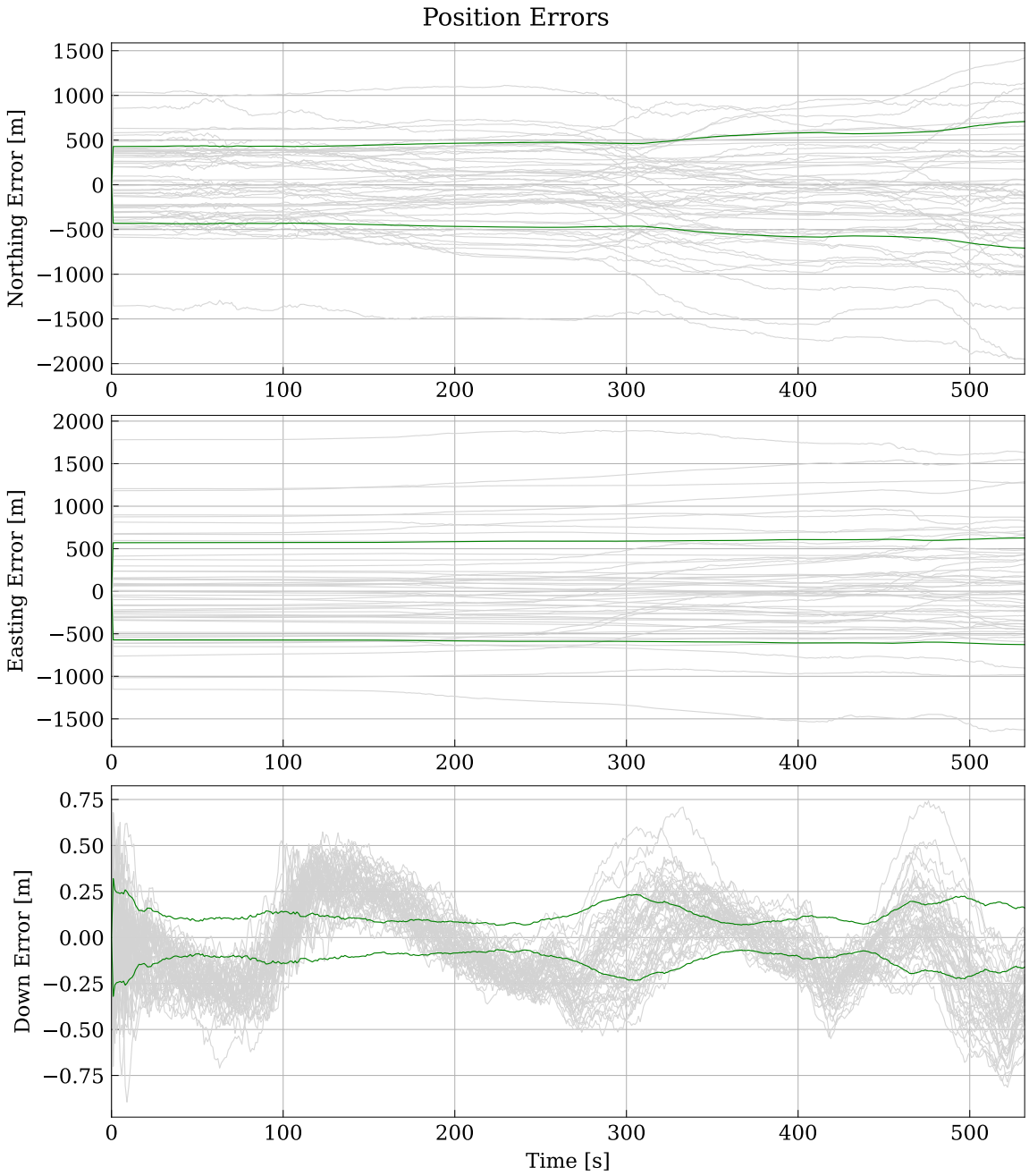

Figure 84: Third hypersonic trajectory unaided navigation grade IMU performance using initial conditions for the EMM navigation simulations.

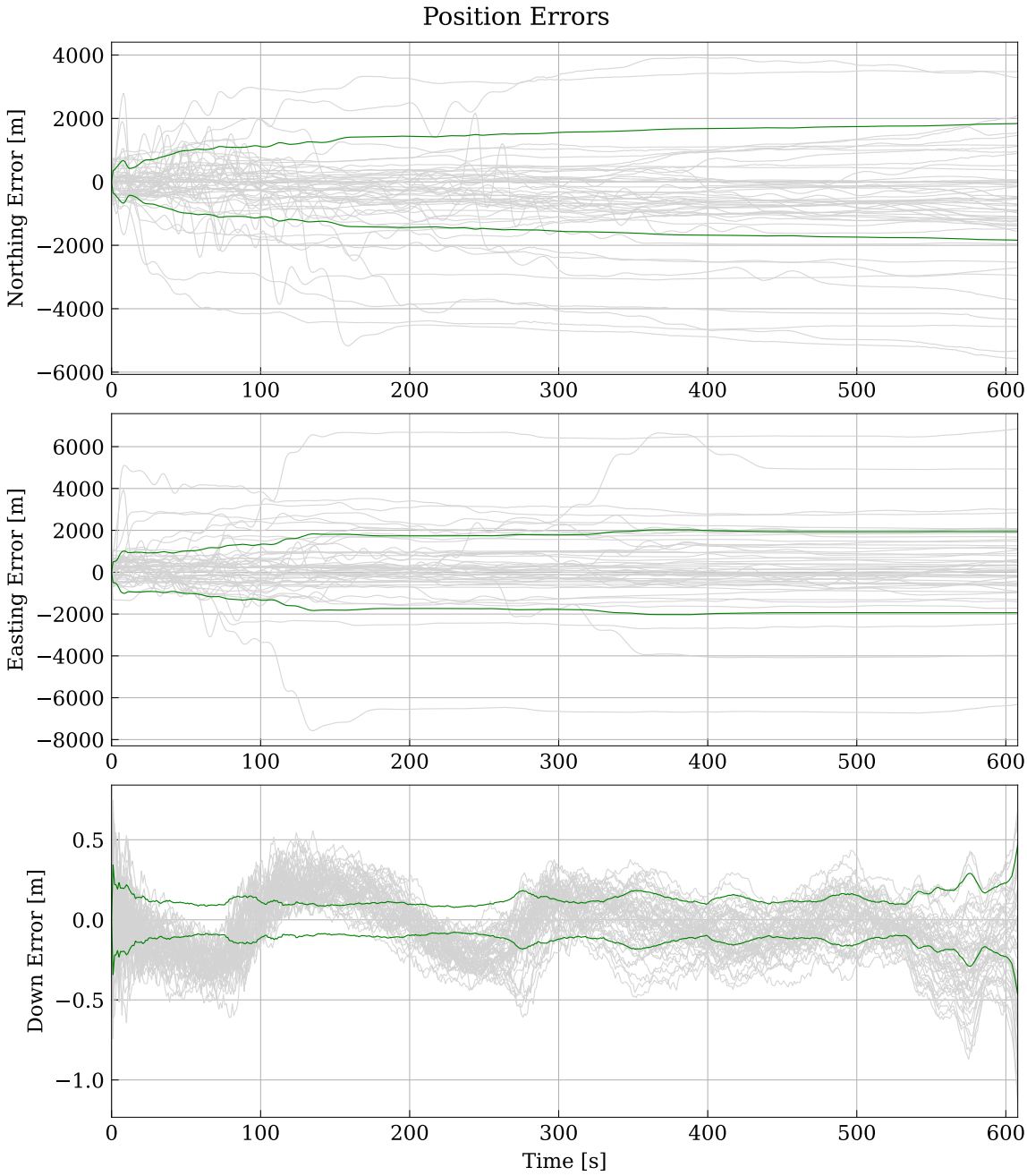

Figure 85: Fourth hypersonic trajectory navigation grade IMU MagNav filter performance using EMM as navigation map.

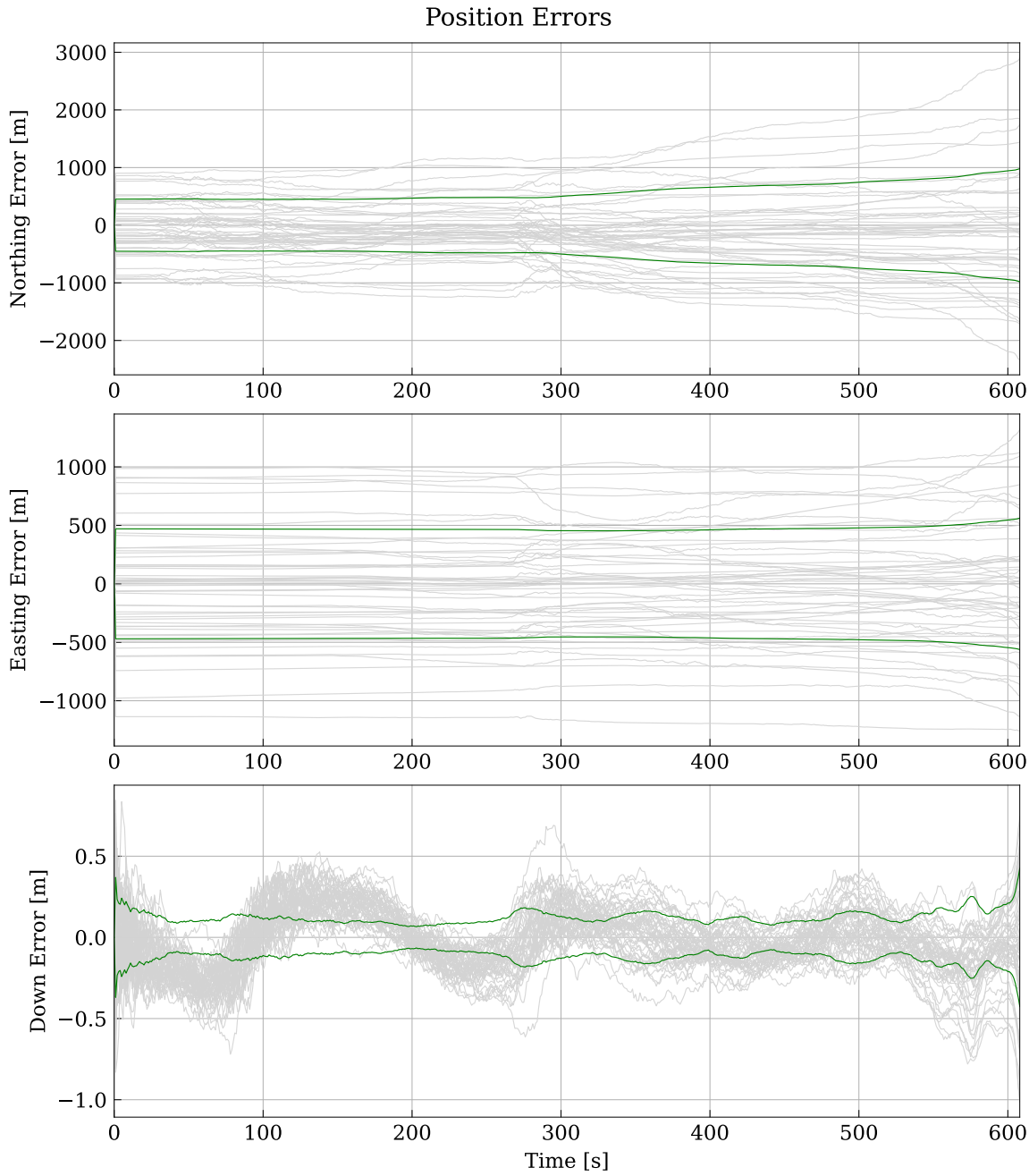

Figure 86: Fourth hypersonic trajectory unaided navigation grade IMU performance using initial conditions for the EMM navigation simulations.

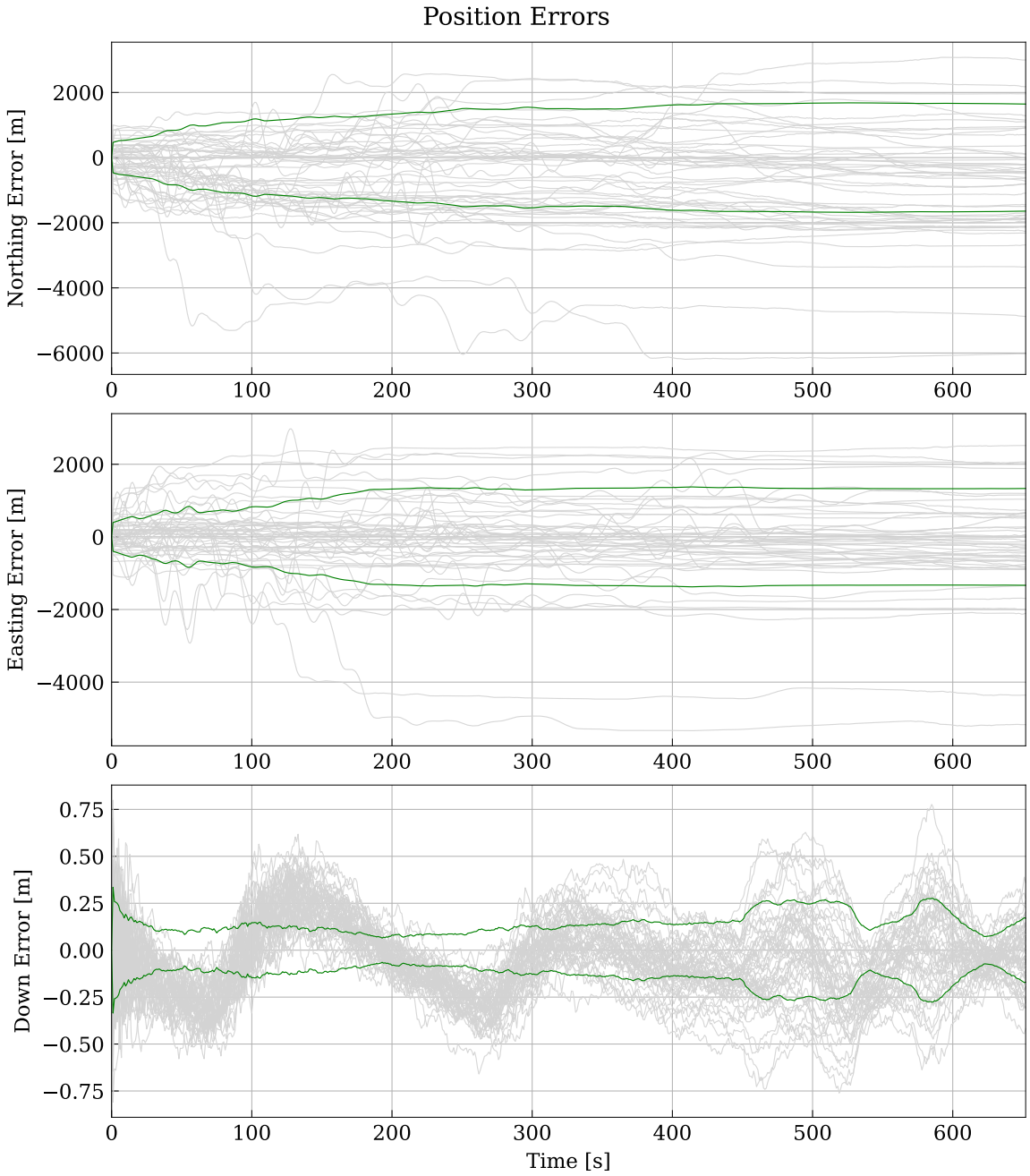

Figure 87: Fifth hypersonic trajectory navigation grade IMU MagNav filter performance using EMM as navigation map.

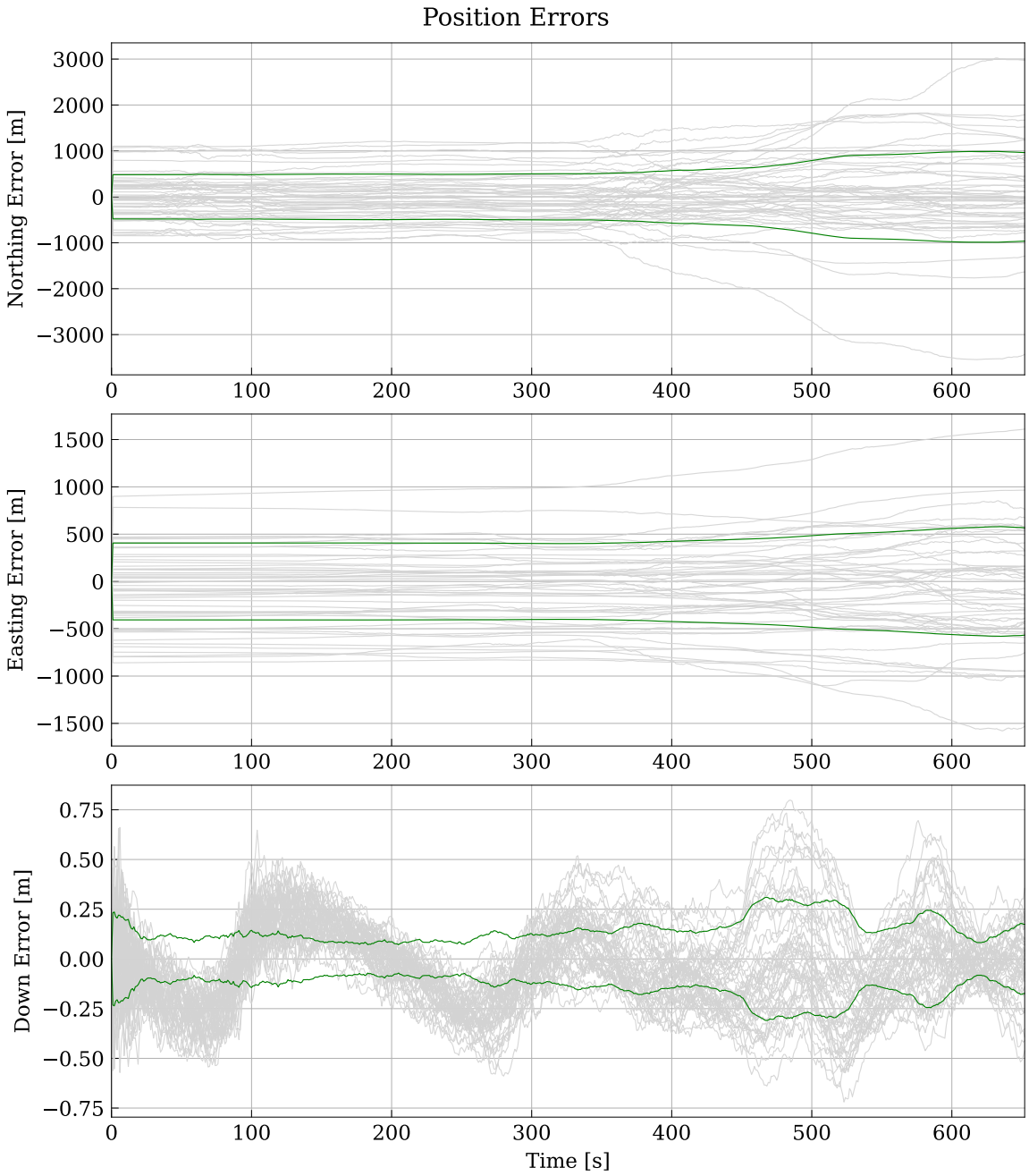

Figure 88: Fifth hypersonic trajectory unaided navigation grade IMU performance using initial conditions for the EMM navigation simulations.

Appendix D. Additional Vector MagNav Simulations

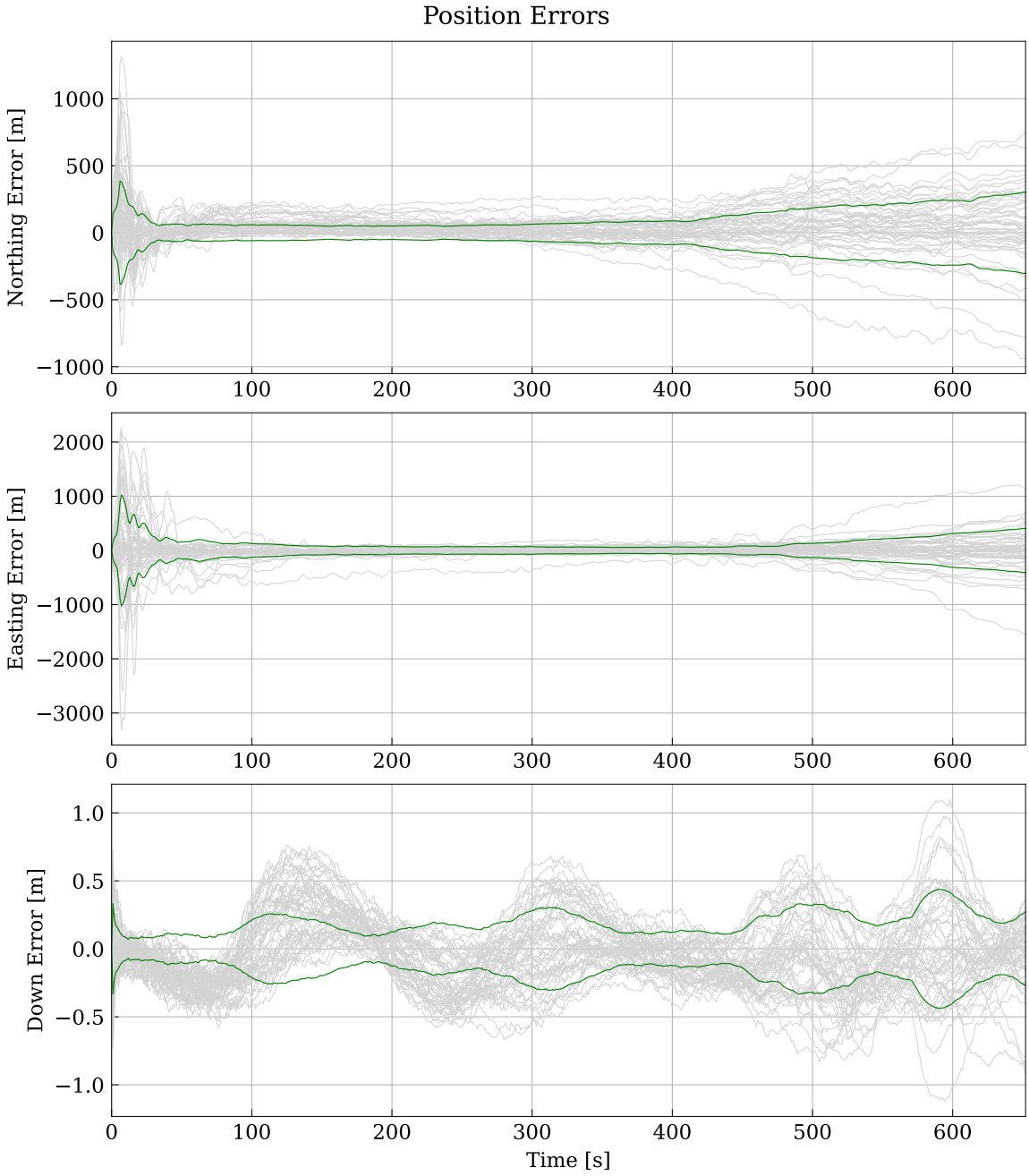

Figure 89: Second hypersonic trajectory navigation grade IMU MagNav filter performance using vector MagNav.

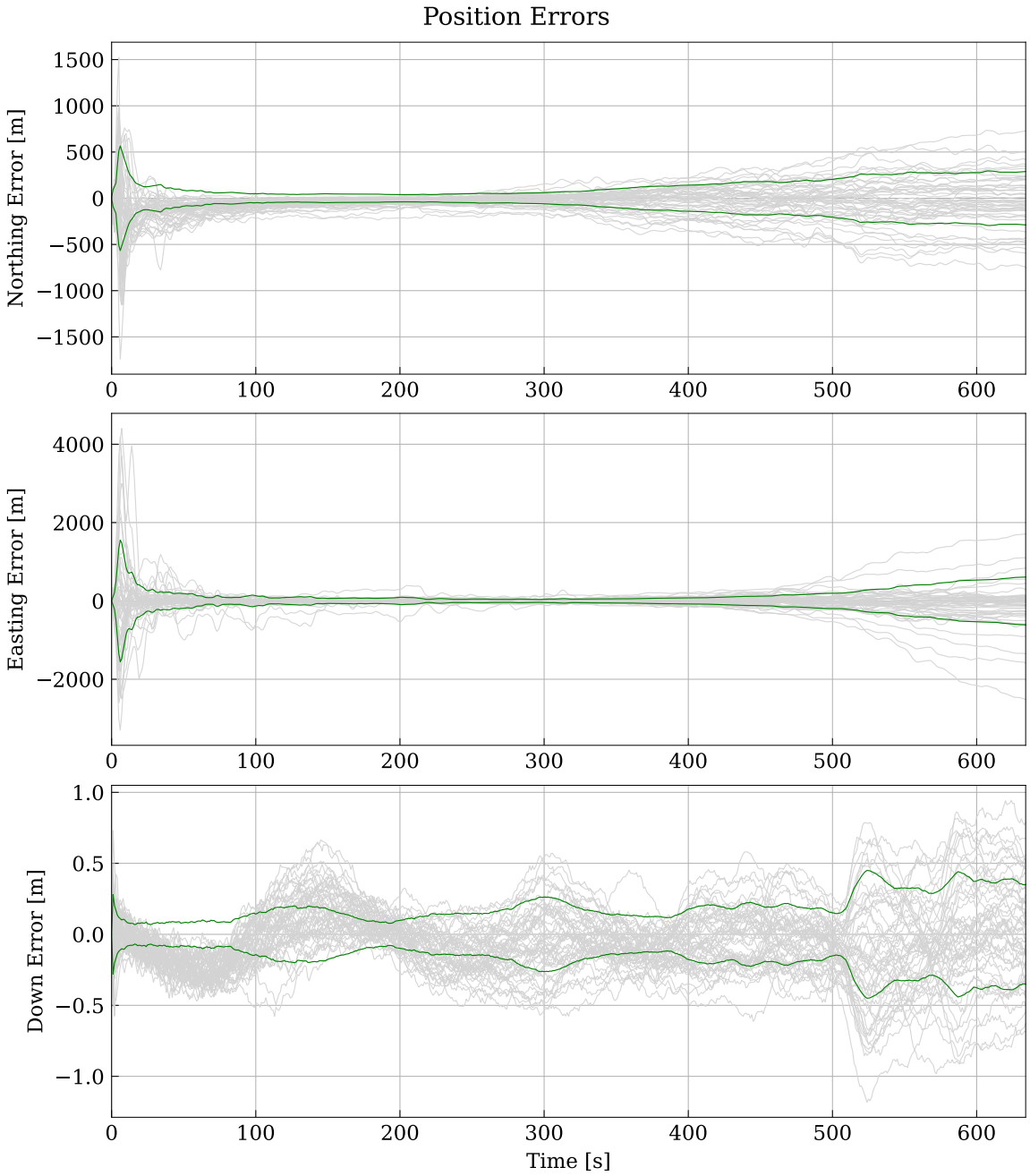

Figure 90: Third hypersonic trajectory navigation grade IMU MagNav filter performance using vector MagNav.

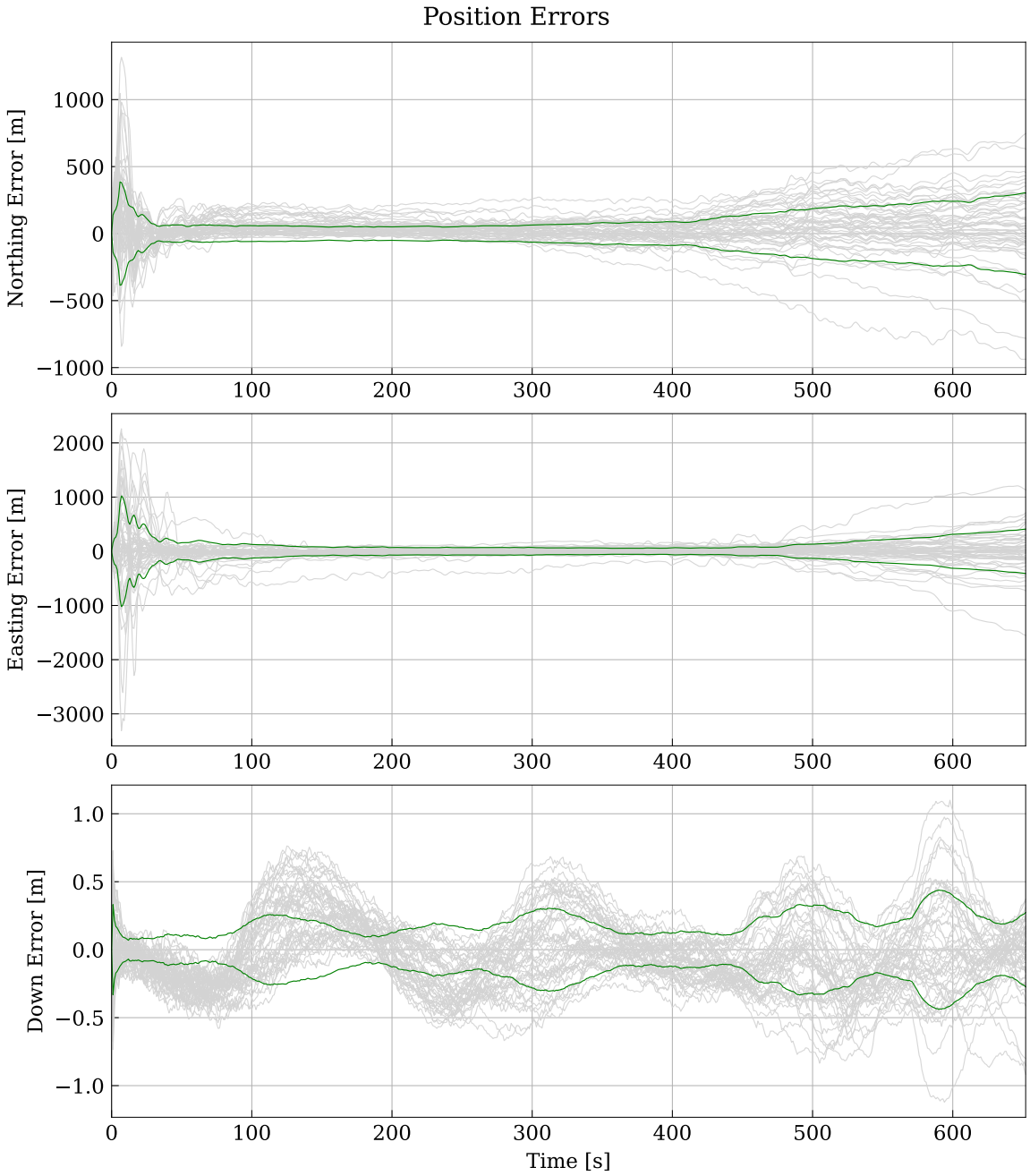

Figure 91: Fourth hypersonic trajectory navigation grade IMU MagNav filter performance using vector MagNav.

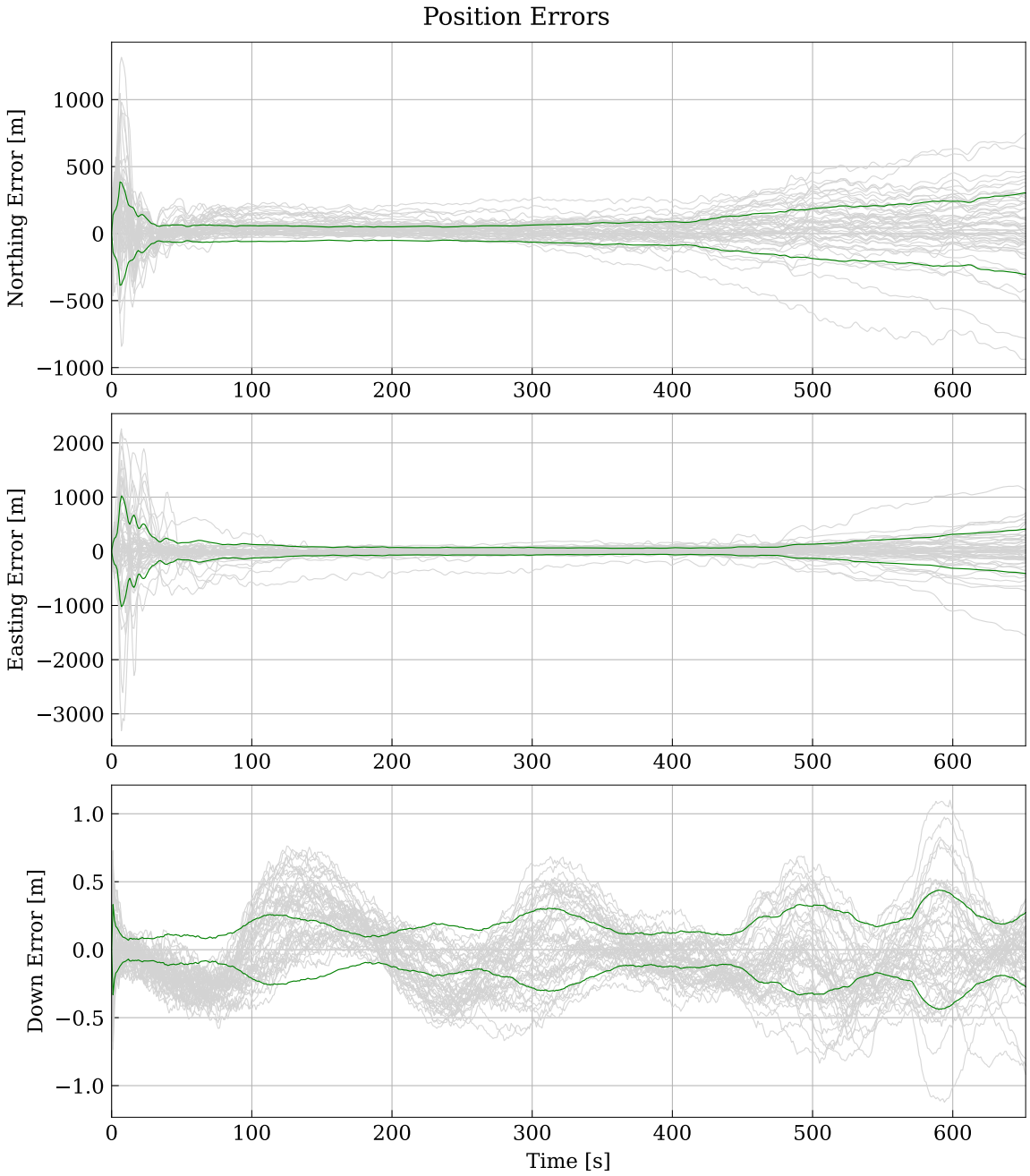

Figure 92: Fifth hypersonic trajectory navigation grade IMU MagNav filter performance using vector MagNav.

Bibliography

1. William H. Hayt and John A. Buck. *Engineering Electromagnetics*. McGraw-Hill, New York, 8 edition, 2012.

2. Aaron J. Canciani. *Absolute Positioning Using the Earth's Magnetic Anomaly Field*. PhD thesis, Air Force Institute of Technology, 2016.

3. Aaron J Canciani. Magnetic Navigation on an F-16 Aircraft using Online Calibration. pages 1–15, 2021.

4. Arnaud Chulliat Patrick Alken Manoj Nair Adam Woods Brian Meyer Michael Paniccia, William Brown Ciarán Beggan Grace Cox Susan Macmillan, W Brown, P Alken, C Beggan, M Nair, G Cox, A Woods, and S Macmillan. The US/UK World Magnetic Model for. pages 2020–2025, 2020.

5. Viki Bankey, Alejandro Cuevas, David Daniels, Carol A. Finn, Israel Hernandez, Patricia Hill, Robert Kucks, Warner Miles, Mark Pilkington, Carter Roberts, Walter Roest, Victoria Rystrom, Sarah Shearer, Stephen Snyder, Ronald Sweeney, Julio Velez, J.D. Phillips, and D. Ravat. Digital Data Grids for the Magnetic Anomaly Map of North America. Technical report, U.S. Geological Survey, Denver, Colorado, USA, 2002.

6. Laurie A. Marshall, Catherine Bahm, Griffin P. Corpening, and Robert Sherrill. Overview with results and lessons learned of the X-43 A Mach 10 flight. *A Collection of Technical Papers - 13th AIAA/CIRA International Space Planes and Hypersonic Systems and Technologies Conference*, 2:1237–1259, 2005.

7. Colin Reeves. Aeromagnetic Surveys, 2005.

8. Andrej J. Lysak. Using Deep Reinforcement Learning to Train an Artificial Neural Network to Fly Hypersonic Glide Vehicles. *AFIT Scholar*, 2021.

9. Yu Li and Nai Gang Cui. Optimal attack trajectory for hypersonic boost-glide missile in maximum reachable domain. *2009 IEEE International Conference on Mechatronics and Automation, ICMA 2009*, pages 4012–4017, 2009.

10. Yvonne Gibbs. CFD Image of X-43A at Mach 7 Test Condition, 2009.

11. Aaron Canciani. Navigation Capabilities Enabled by a Super-Low Altitude Satellite (SLAT) Crustal Magnetism Constellation Principle Investigator Australian Data-Set.

12. Aaron Joseph Canciani and Christopher J. Brennan. An Analysis of the Benefits and Difficulties of Aerial Magnetic Vector Navigation. *IEEE Transactions on Aerospace and Electronic Systems*, 56(6):4161–4176, 2020.

13. Erwan Thébault, Michael Purucker, Kathryn A. Whaler, Benoit Langlais, and Terence J. Sabaka. The magnetic field of the earth's lithosphere. *Space Science Reviews*, 155(1-4):95–127, 2010.

14. Peter S. Maybeck. *Stochastic Models, Estimation, and Control Volume 1.* Academic Press Inc., WPAFB, OH, 1 edition, 1979.

15. Thomas Schön, Fredrik Gustafsson, and Per Johan Nordlund. Marginalized particle filters for mixed linear/nonlinear state-space models. *IEEE Transactions on Signal Processing*, 53(7):2279–2289, 2005.

16. David H. Titterton and John L. Weston. *Strapdown intertail Navigation Technology.* The American Institude of Aeronautics and Astronautics, Reston VA, 2 edition, 2002.

17. David Woodburn and Robert C. Leishman. *Inertial navigation*, volume 1. 2021.

18. Nils Olsen, Eigil Friis-Christensen, Rune Floberghagen, Patrick Alken, Ciaran D. Beggan, Arnaud Chulliat, Eelco Doornbos, João Teixeira Da Encarnação, Brian Hamilton, Gauthier Hulot, Jose Van Den Ijssel, Alexey Kuvshinov, Vincent Lesur, Hermann Lühr, Susan Macmillan, Stefan Maus, Max Noja, Poul Erik H. Olsen, Jaeheung Park, Gernot Plank, Christoph Püthe, Jan Rauberg, Patricia Ritter, Martin Rother, Terence J. Sabaka, Reyko Schachtschneider, Olivier Sirol, Claudia Stolle, Erwan Thébault, Alan W.P. Thomson, Lars Tøffner-Clausen, Jakub Velímský, Pierre Vigneron, and Pieter N. Visser. The Swarm satellite constellation application and research facility (SCARF) and Swarm data products. *Earth, Planets and Space*, 65(11):1189–1200, 2013.

19. Richard J. Blakely. *Potential Theory in Gravity and Magnetic Applications*. Cambridge University Press, jan 1995.

20. Yaoguo Li and Sarah Devriese. Enhancement of magnetic data by stable downward continuation for UXO applications. *79th Society of Exploration Geophysicists International Exposition and Annual Meeting 2009, SEG 2009*, 51(6):1464–1468, 2009.

21. M. Fedi and G. Florio. A stable downward continuation by using the ISVD method. *Geophysical Journal International*, 151(1):146–156, 2002.

22. E. Friis-Christensen, H. Lühr, and G. Hulot. Swarm: A constellation to study the Earth's magnetic field. *Earth, Planets and Space*, 58(4):351–358, 2006.

23. Irma Shamatava, Gregory Schultz, and Fridon Shubitidze. Predicting Earth magnetic anomalies from measured EMAG2 data. *Proceedings of International Sem-*

inar/Workshop on Direct and Inverse Problems of Electromagnetic and Acoustic Wave Theory, DIPED, 2016-Decem:127–130, 2016.

24. NASA. Magnetic Fields - Earth and Extraterrestrial. (March), 1969.

25. Terence J. Sabaka, Nils Olsen, and Robert A. Langel. A comprehensive model of the quiet-time, near-Earth magnetic field: Phase 3. *Geophysical Journal International*, 151(1):32–68, 2002.

26. Tai Chow. *Introduction to Electromagnetic Theory: A Modern Perspective*. Jones and Barlett Publishers, Boston, MA, 2006.

27. W.E. Tolles and J.D. Lawson. Magnetic compensation of mad equipped aircraft. Technical report, Airborn Instruments Lab, INC., 1950.

28. Sander Geophysics Ltd. High Resolution Magnetic Gradiometer Surveys: Fixed-Wing or Helicopter.

29. Guanyi Zhao, Qi Han, Xiang Peng, Pengyi Zou, Haidong Wang, Changping Du, He Wang, Xiaojun Tong, Qiong Li, and Hong Guo. An aeromagnetic compensation method based on a multimodel for mitigating multicollinearity. *Sensors (Switzerland)*, 19(13):1–13, 2019.

30. John D. Anderson. *Hypersonic and High Temperature Gas Dynamics*. American INstitute of Aeronautics and Astronautics Inc, 2nd edition, 2006.

31. John D. Jackson. *Classical Electrodynamics*. John Wiley and Sons, New York, first edition, 1962.

32. H. J. van Leeuwen. Vraagstukken uit de Electronentheorie van het Magnetisme. 1919.

33. Paul Gibbon. Introduction to plasma physics. *arXiv*, 001(November 2014):23–29, 2020.

34. Tom Neiser. Calculating The Magnetic Permeability of a Known Plasma, 2017.

35. Bruce A. Webb and Richard W. Ziolkowski. Enabling Transmission Through Reentry Plasmas: Simulation of Plasma-SRR Layered Materials. *2018 6th IEEE International Conference on Wireless for Space and Extreme Environments, WiSEE 2018*, pages 101–103, 2019.

36. Kyle Kauffman, Daniel Marietta, John Raquet, Daniel Carson, Robert C. Leishman, Aaron Canciani, Adam Schofield, and Michael Caporellie. Scorpion: A Modular Sensor Fusion Approach for Complementary Navigation Sensors. *2020 IEEE/ION Position, Location and Navigation Symposium, PLANS 2020*, pages 156–167, 2020.

Acronyms

CFD Computational Fluid Dynamics. 100

DRMS Distance Root Mean Squared. 6, 65, 72, 79

EEJ Equatorial Electro Jet. 23, 24

EKF Extended Kalman Filter. 7, 8, 9, 30, 38

EMM Enhanced Magnetic Model. vi, ix, xiii, 3, 16, 17, 41, 52, 57, 58, 60, 62, 80, 81, 82, 83, 84, 85, 86, 87, 88, 90, 91, 95, 97, 99

FOGM First Order Gauss-Markov. 54, 56

FOM Figure of Mirit. 30

GPS Global Positioning System. iv, vii, 1, 19

HGV Hypersonic Glide Vehicle. vii, 31, 32, 33, 40, 41, 42, 58, 59, 69, 72, 95, 96

IMU inertial measurement unit. viii, ix, xiii, 1, 8, 10, 11, 31, 32, 39, 40, 41, 53, 55, 56, 59, 60, 61, 65, 66, 67, 68, 71, 72, 73, 74, 75, 76, 77, 78, 79, 80, 81, 82, 83, 84, 85, 86, 87, 88, 94, 96, 100, 103, 106, 109, 112, 114, 116, 118, 120, 122, 124, 126, 128

MagNav Magnetic Navigation. iv, vii, viii, ix, x, xiii, 1, 2, 3, 4, 5, 6, 7, 8, 9, 10, 11, 12, 13, 14, 15, 16, 17, 22, 24, 25, 27, 30, 31, 32, 33, 34, 37, 38, 39, 40, 43, 52, 53, 54, 55, 57, 58, 59, 60, 61, 62, 64, 65, 69, 72, 73, 75, 76, 78, 79, 80, 81, 82, 83, 84, 85, 86, 88, 89, 90, 91, 92, 93, 94, 95, 96, 98, 99, 100, 102, 105, 108, 111, 113, 115, 117, 119, 121, 123, 125, 127, 129, 130, 131, 132

NAMAD North American Magnetic Anomaly Database. vii, 18, 19

PSD Power Spectral Density. vii, 44, 46, 47, 48

WMM World Magnetic Model. 6, 9, 16, 22

REPORT DOCUMENTATION PAGE

Form Approved
OMB No. 0704–0188

1. REPORT DATE *(DD–MM–YYYY)*	2. REPORT TYPE	3. DATES COVERED *(From — To)*
06–03–2022	Master's Thesis	Sept 2020 — Mar 2022

4. TITLE AND SUBTITLE

Magnetic Anomaly Absolute Positioning for Hypersonic Aircraft

5a. CONTRACT NUMBER

5b. GRANT NUMBER

5c. PROGRAM ELEMENT NUMBER

6. AUTHOR(S)

Alexander J. McNeil

5d. PROJECT NUMBER

5e. TASK NUMBER

5f. WORK UNIT NUMBER

7. PERFORMING ORGANIZATION NAME(S) AND ADDRESS(ES)

Air Force Institute of Technology
Graduate School of Engineering and Management (AFIT/EN)
2950 Hobson Way
WPAFB OH 45433-7765

8. PERFORMING ORGANIZATION REPORT NUMBER

AFIT-ENG-MS-22-M-046

9. SPONSORING / MONITORING AGENCY NAME(S) AND ADDRESS(ES)

AFRL/RWWN
101 West Eglin Blvd
Building 421
Eglin AFB, FL 32542
COMM 937-XXX-XXXX
Email: kevin.brink@us.af.mil

10. SPONSOR/MONITOR'S ACRONYM(S)

AFRL/RWWN

11. SPONSOR/MONITOR'S REPORT NUMBER(S)

12. DISTRIBUTION / AVAILABILITY STATEMENT

DISTRIBUTION STATEMENT A:
APPROVED FOR PUBLIC RELEASE; DISTRIBUTION UNLIMITED.

13. SUPPLEMENTARY NOTES

14. ABSTRACT

GPS has proven to be an extremely valuable asset for navigation, and timing. GPS has become the standard navigation system for all applications, but GPS has limitations. GPS is susceptible to jamming, spoofing, and in the case of hypersonic aircraft, is likely unavailable. When an aircraft is traveling at hypersonic speeds, there is a plasma sheath that surrounds the aircraft. This plasma sheath blocks electromagnetic waves, and is therefore responsible for a GPS blackout. GPS unavailability for hypersonic aircraft has prompted the research into the viability of alternate navigation systems for these aircraft. This paper seeks to explore the viability of MagNav for hypersonic aircraft. Hypersonic aircraft present new challenges for MagNav including: high altitudes, high speeds, large scale map availability, and new noise sources. This paper explores these challenges to determine if any poses an insurmountable problem. Simulations are conducted to explore the potential performance of MagNav on a hypersonic vehicle. These simulations conclude that MagNav is viable on a hypersonic aircraft.

15. SUBJECT TERMS

magnetic navigation, MagNav, hypersonic glide vehicles, alternate navigation

16. SECURITY CLASSIFICATION OF:			17. LIMITATION OF ABSTRACT	18. NUMBER OF PAGES	19a. NAME OF RESPONSIBLE PERSON
a. REPORT	b. ABSTRACT	c. THIS PAGE			Alexander McNeil, AFIT/ENG
U	U	U	UU	154	19b. TELEPHONE NUMBER *(include area code)* (209) 288-9257; alexander.mcneil.ctr@afit.edu